DISSERTATION

LINKS BETWEEN CLIMATE FEEDBACKS AND THE LARGE-SCALE CIRCULATION ACROSS IDEALIZED AND COMPLEX CLIMATE MODELS

Submitted by

Luke L. B. Davis

Department of Atmospheric Science

In partial fulfillment of the requirements

For the Degree of Doctor of Philosophy

Colorado State University

Fort Collins, Colorado

Summer 2023

Doctoral Committee:

Advisor: David W. J. Thompson

Eric Maloney
David Randall
Olivier Pinaud
Edwin Gerber

ABSTRACT

LINKS BETWEEN CLIMATE FEEDBACKS AND THE LARGE-SCALE CIRCULATION ACROSS IDEALIZED AND COMPLEX CLIMATE MODELS

The circulation response to anthropogenic forcing is typically considered in one of two distinct frameworks: One that uses radiative forcings and feedbacks to investigate the thermodynamics of the response, and another that uses circulation feedbacks and thermodynamic constraints to investigate the dynamics of the response. In this thesis, I aim to help bridge the gap between these two frameworks by exploring direct links between climate feedbacks and the atmospheric circulation across ensembles of experiments from idealized and complex general circulation models (GCMs).

I first demonstrate that an existing, widely-used type of idealized GCM — the dynamical core model — has climate feedbacks that are explicitly prescribed and determined by a single parameter: The thermal relaxation timescale. The dynamical core model may thus help to fill gaps in the model hierarchies commonly used to study climate forcings and climate feedbacks. I then perform two experiments: One that explores the influence of prescribed feedbacks on the unperturbed, climatological circulation; and a second that explores their influence on the circulation response to a horizontally uniform, global warming-like forcing perturbation. The results indicate that more stabilizing climate feedbacks are associated with 1) a more vigorous climatological circulation with increased thermal diffusivity, and 2) a weaker poleward displacement of the circulation in response to the global warming-like forcing. Importantly, since the most commonly-used relaxation timescale field resembles the real-world clear-sky feedback field, the uniform forcing perturbations produce realistic warming patterns, with amplified warming in the tropical upper troposphere and polar lower troposphere. The warming pattern and circulation response disappear when the relaxation timescale field is instead spatially uniform, demonstrating the critical role of spatially-varying feedback processes on shaping the response to anthropogenic forcing.

I next explore circulation-feedback relationships in more complex GCMs using results from the most recent Coupled Model Intercomparison Projects (CMIP5 and CMIP6). Here, I estimate climate feedbacks by regressing top-of-atmosphere radiation against surface temperature for both 1) an unperturbed pre-industrial control experiment and 2) a perturbed global warming experiment forced by an abrupt quadrupling of CO_2 concentrations. I find that across both ensembles, the cloud component of the perturbed climate feedback is closely related to the cloud component of the unperturbed climate feedback. Critically, the relationship is much stronger in CMIP6 than CMIP5, contrasting with many previously proposed constraints on the perturbation response. The relationship also explains the slow part of the CO_2 response better than the fast, transient response. In general, the strength of the relationship depends on the degree to which the spatial pattern of the response resembles ENSO-dominated internal variability, with "El Niño-like" East Pacific warming and related tropical cloud changes. This is consistent with fluctuation-dissipation theory: Regions with stronger deep ocean heat exchange and weaker net feedbacks must always dominate both 1) internal fluctuations in the global energy budget, and 2) the slow part of the response to forcing perturbations. The stronger CMIP6 inter-model relationships are due to both an ampification of this mechanism and higher inter-model correlations between tropical cloud changes and extratropical cloud changes. Finally, I present emergent constraints on the slow response using a recent observational estimate of the unperturbed cloud feedback.

I conclude by discussing some implications of these results. I consider how the relaxation feedback framework might be further developed and reconciled with traditional climate feedbacks to provide future research opportunities with climate model hierarchies.

ACKNOWLEDGEMENTS

This thesis was supported by the U.S. National Science Foundation Climate Dynamics Program. I would like to thank my advisors David W. J. Thompson and Thomas Birner for teaching me so much, and for their kindness, encouragement, and patience over these past years. I would also like to thank Maria A. A. Rugenstein for her guidance and insight over our many engaging meetings, my Ph.D. committee for their help and for giving me time to complete this degree, and my research group colleagues (past and present) for all of their support. I would like to thank my grandparents, Vivianne T. Nachmias and Jacob Nachmias, former Professors at the University of Pennsylvania, for inspiring me to pursue a career in science from a young age. I would like to thank my mother, Lisa N. Davis, for her love and her many sacrifices, without which this thesis would not be possible and for which I will always be in debt. I'd like to thank other friends and family for their love and support in times good and bad.

TABLE OF CONTENTS

LIST OF TABLES

LIST OF FIGURES

Chapter 1

Introduction

1.1 Motivation and outline

The physical processes that determine the temperature of Earth's surface have been of scientific interest for centuries (*Anderson et al.* 2016, *Lacis et al.* 2010, *Mudge* 1997). An insulating *greenhouse effect*, caused by atmospheric absorption of infrared radiation, was first proposed in the early 19th century (*Fourier* 1827, *Pouillet* 1838). In the late 19th century, this effect was attributed to the *greenhouse gases* carbon dioxide (CO_2) and water vapor (H_2O) – first qualitatively by John Tyndall (*Tyndall* 1861), then quantitatively by Svante Arrhenius (*Arrhenius* 1896). Following this foundational work, throughout the early and middle 20th century, a growing body of research noticed the possible influence of human activities on greenhouse gases and their attendant greenhouse effects (*Bolin and Eriksson* 1959, *Callendar* 1938, *Keeling* 1970, *Revelle and Suess* 1957, *Sawyer* 1972). This culminated in the development of early computer models that provided rudimentary predictions of these effects (*Manabe and Wetherald* 1967, 1975, *Schneider and Dickinson* 1974, *Sellers* 1969), followed by an immensely impactful synthesis of these efforts commonly called "The Charney Report" (*Charney et al.* 1979). This report identified fossil fuel burning as responsible for past increases in CO_2, predicted continued and substantial future increases, and estimated the surface warming associated with an eventual doubling of CO_2 at approximately $3 \pm 1.5\,\mathrm{K}$, marshaling an explosion of growth in the field of climate science.

Today, climate science encompasses a huge variety of phenomena beyond the essential warming effect of greenhouse gases. However, the average surface warming originally predicted by the Charney report has remained persistently uncertain (*Charney et al.* 1979, *Knutti et al.* 2017, *Roe and Baker* 2007, *Sherwood et al.* 2020). Much of this uncertainty propagates to the circulation response to increasing CO_2: The warming itself is connected to various hydrologic and energetic aspects of the circulation response (e.g., *Bony et al.* 2013, *Chadwick et al.* 2019, *He and Soden*

2015, *Held and Soden* 2006, *Pendergrass and Hartmann* 2014, *Vecchi and Soden* 2007), while patterns and gradients in the warming are connected to dynamical aspects of the circulation response (e.g., *Brayshaw et al.* 2008, *Davis and Birner* 2022, *Grise and Polvani* 2014, 2016, *Held* 1993, *Williamson et al.* 2013, *Zhang et al.* 2019). Some parts of the circulation response are also dependent on opposing or time-varying thermodynamic changes, such that individual model simulations may exhibit significant changes while the average across several model simulations exhibits a very weak change (e.g., *Ceppi and Shepherd* 2017, *Feldl et al.* 2017, *Heede et al.* 2020, *Shaw and Voigt* 2015, *Shaw et al.* 2016). Overall, the close relationship between temperature and circulation responses to increasing greenhouse gas concentrations underscores the critical need to understand and constrain their coupled interactions.

The warming response to greenhouse gas emissions is commonly assessed using the forcing-feedback framework (*Hansen et al.* 1985). Under this framework, the warming induced by increasing CO_2 is broken down into the ratio between 1) *radiative forcing perturbations*, which instigate energetic imbalances at the surface and throughout the atmospheric column, and 2) *radiative climate feedbacks*, which comprise the pathways used by the climate system to restore energetic balance and adjust to the new equilibrium state (e.g., *Hansen et al.* 1985, *Roe* 2009, *Rugenstein and Armour* 2021). The global average temperature change resulting from the radiative forcing and feedback processes is typically called the *climate sensitivity*. While the forcing-feedback framework is widely used to explore the energetics of the response, it is much less commonly used to explore the circulation response. Instead, circulation changes are typically investigated by relating the circulation to the background thermodynamic state through the lens of circulation feedbacks and steady-state thermodynamic constraints (e.g., *Armour et al.* 2019, *Butler et al.* 2011, *Chen et al.* 2020, *Davis and Birner* 2019, *Held* 1999, *Schneider and Walker* 2006, *Zhang et al.* 2021). This is important, since there is also clearly a robust two-way coupling between the circulation and the climate feedbacks themselves (e.g., *Ceppi and Shepherd* 2017, *Lu et al.* 2021, *Sun et al.* 2013).

The aim of this thesis is to explore direct relationships between climate feedbacks, climate sensitivity, and the large-scale circulation. The rest of Chapter 1 surveys some of the existing lit-

erature on the two frameworks identified above: Forcing-feedback effects on the thermodynamic response, and thermodynamic effects on the circulation response. Chapter 2 demonstrates that the thermal relaxation coefficients used with *dynamical core* configurations of general circulation models (GCMs) determine the response of the model to forcing perturbations. In other words, the climate feedbacks of dynamical core models are exactly linear and can be explicitly prescribed, allowing us to study their direct influence on the large-scale circulation. Chapter 3 uses the theory from Chapter 2 to explore the influence of climate feedbacks on both 1) the unperturbed large-scale circulation and 2) the circulation response to forcing perturbations. Chapter 4 provides more traditional estimates of the climate feedback (based on surface temperature rather than prescribed thermal relaxation timescales) using experiments from the most recent two Coupled Model Intercomparison Projects (CMIP5 and CMIP6; *Eyring et al.* 2016, *Taylor et al.* 2012), identifying a strong inter-model relationship between cloud feedbacks estimated from internal variability and cloud feedbacks estimated from increased CO_2 concentrations. Chapter 5 investigates this inter-model relationship and identifies the roles of circulation-moderated pattern effects and cloud shifts on the strength of the relationship. Chapter 6 offers concluding remarks on the idealized and coupled model results, then discusses possible extensions of the relaxation feedback framework that could be used to build novel model hierarchies for studying effects of cloud feedbacks on the circulation response to global warming.

1.2 Circulation responses

As with the thermodynamic response, understanding the circulation response to global warming requires simplified frameworks that describe the coupling between atmospheric dynamics and atmospheric thermodynamics. The future circulation can then be predicted from the impingement of greenhouse effects onto the thermodynamics of the framework. Figure 1.1 (bottom) depicts these frameworks and their connections to different components of the climate system (thermodynamic forcing-feedback frameworks are further depicted on the top of the figure; see Section 1.3). These frameworks describe either the effects of thermodynamics on the circulation (i.e., dynam-

ical closures and energetic constraints) or the effects of the circulation on thermodynamics (i.e., circulation feedbacks). Circulation feedback frameworks seek to capture the direct effects of large-scale circulation features – namely, overturning cells and baroclinic eddies – on the background states from which they emerge (e.g., *Hoskins and Valdes* 1989, *Hoskins et al.* 1983, *Xie* 1996, *Xie and Philander* 1994). These include rigorous, analytic treatments for the effects of baroclinic eddies on thermal stratification and troposphere depth (*Held* 1999, *Schneider* 2004, *Schneider and Walker* 2006) or the maintenance of baroclinicity maxima from which the eddies are generated (*Lorenz and Hartmann* 2001, 2003, *Robinson* 2000, *Thompson and Barnes* 2014). More recently, some authors have developed forcing-feedback frameworks suitable for the atmospheric circulation, in which changes to eddy-mean flow coupling are linearized against the mean flow response (analogous to a linearization of radiation against the mean temperature response; *Chen et al.* 2020, *Zhang et al.* 2021). Others have isolated eddy feedbacks on the tropical Hadley circulation using mechanism-denial experiments with axisymmetric and eddy-resolving GCM simulations (*Davis and Birner* 2019, 2022).

This thesis focuses on simpler thermodynamic constraints – namely, dynamical closures (Figure 1.1, bottom left), under which energy transport diffusively adjusts to changes in the background thermodynamics; and energetic constraints (Figure 1.1, bottom right), under which energy transport is constrained to balance energetic exchange at the boundaries of the atmosphere (*Armour et al.* 2019). Using the diffusive perspective, enhanced tropical-subtropical upper tropospheric warming has been shown to shift the storm track and eddy-driven jet poleward through increased baroclinicity (*Butler et al.* 2010, 2011) and static stability (*Lu et al.* 2010, *Mbengue and Schneider* 2013), with subtropical heating playing an outsize role in determining this poleward shift (*Baker et al.* 2017, *Shaw and Tan* 2018). By contrast, enhanced polar heating is associated with equatorward shifts through reduced baroclinicity (*Baker et al.* 2017, *Butler et al.* 2010). More recently, cloud feedbacks have been argued to drive the large part of the poleward circulation shift predicted by coupled climate models (*Ceppi and Hartmann* 2016, *Ceppi and Shepherd* 2017, *Li et al.* 2019). Cloud radiative feedbacks lead to warming patterns with strong meridional gradients, while

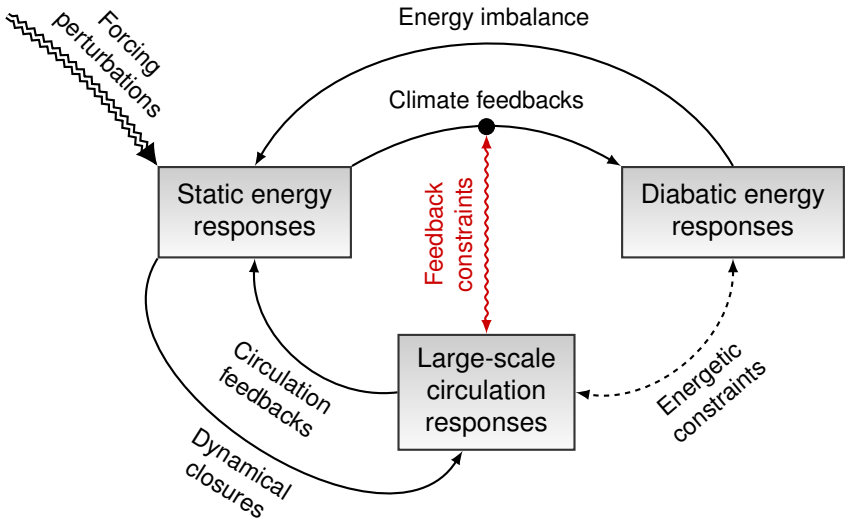

Figure 1.1: Summary of frameworks for assessing the climate system response to forcing perturbations. The three boxes represent distinct components of the climate system: static energy reservoirs (i.e., temperature and humidity; upper left), diabatic energy exchange (i.e., radiative and turbulent fluxes; upper right), and large-scale circulation features (i.e., eddies and overturning cells; bottom). The arrows represent physical mechanisms associated with changes to each climate system component. The thick, zigzag arrow represents external forcing perturbations (e.g., via greenhouse gases, sulfate aerosols, or insolation). Solid arrows indicate causal links internal to the climate system, where changes to one component lead to changes in another. Dashed arrows indicate associative links, where a robust diagnostic relationship exists but the causality of the relationship is unclear. Squiggle arrows indicate links between climate system components and the coupling mechanisms themselves.

clear-sky radiative feedbacks lead to warming patterns with opposing meridional gradients (i.e., enhanced tropical upper tropospheric warming and polar lower tropospheric warming; *Shaw et al.* 2016). Diffusive adjustments can also explain increased moist static energy transport under global warming, due to the strong meridional gradient in the specific humidity adjustments associated with warming (*Armour et al.* 2019, *Held and Soden* 2006). This increase is partly compensated by reductions in sensible heat transport, due to polar amplification reducing the near-surface temperature gradients (*Armour et al.* 2019, *Held and Soden* 2006, *Hwang et al.* 2011).

Energetic constraints provide an even simpler perspective on the circulation response to forcing – although this framework is mainly diagnostic rather than prognostic (Figure 1.1, bottom right; *Armour et al.* 2019, *Shaw et al.* 2018). First, the radiative forcing from rising greenhouse gas concentrations implies greater poleward energy transport in and of itself, due to the temperature dependence and resulting meridional structure of the greenhouse effect change (*Huang and Zhang* 2014, *Huang et al.* 2016). Radiative feedbacks also imply strong transport changes, with temperature feedbacks associated with reduced transport and water vapor and cloud feedbacks associated with increased transport (*Huang et al.* 2017, *Hwang and Frierson* 2010, *Zelinka and Hartmann* 2012). These perspectives are closely related to the diffusive perspective: In response to a forcing, the poles warm more than the tropics through some combination of increased latent heat transport (*Armour et al.* 2019) and locally weaker climate feedbacks (*Henry and Merlis* 2019, *Pithan and Mauritsen* 2014, *Stuecker et al.* 2018). Energetic balance is then restored by some combination of diffusive reductions in sensible heat transport and increased radiative cooling associated with local climate feedbacks. Radiative constraints on meridional transport thus reflect a three-way balance between non-uniform warming, diffusive adjustments, and climate feedbacks (*Hwang et al.* 2011). Finally, radiative constraints can also be used to decompose shifts in the meridional transport maxima associated with global warming (*Barpanda and Shaw* 2017, *Shaw and Voigt* 2016).

Outside of the extratropics, thermodynamic constraints are also used to interpret tropical and hydrologic responses to global warming. Many of these are built upon the canonical $\sim 7\,\%\,/\,\mathrm{K}$ specific humidity response to surface warming, derived from the Clausius-Clapeyron scaling between

temperature and saturation vapor pressure (e.g., *Allen and Ingram* 2002, *Held and Soden* 2006). A $\sim 7\,\% \,/\, \mathrm{K}$ increase reflects the relative humidity-preserving specific humidity adjustment required to satisfy surface energetics without dramatic changes to the circulation (*Allen and Ingram* 2002, *Held and Soden* 2000, *Schneider et al.* 2010). The Clausius-Clapeyron specific humidity response is connected to broad reductions in convective mass flux anomalies (*Held and Soden* 2006), along with the "wet get wetter, dry get drier" paradigm of amplified latent heat flux divergence in dry regions and latent heat flux convergence in wet regions (mainly established over broad ocean regions rather than land; *Byrne and O'Gorman* 2015, *Held and Soden* 2006). The Clausius-Clapeyron response can also be used to explain a part of the Hadley cell expansion associated with global warming (*Shaw and Voigt* 2016). As with atmospheric humidity, global-average changes to evaporation and precipitation can also be understood through energetic constraints. A similarly robust $\sim 2\,\% \,/\, \mathrm{K}$ precipitation response to global warming (often called hydrologic sensitivity, by analogy with climate sensitivity) arises from moderate changes to surface radiation and turbulent sensible heat flux that constrain precipitation changes to far below the Clausius-Clapeyron scaling (*Held and Soden* 2006). The exact value of this hydrologic sensitivity arises from competing effects of a variety of time-varying radiative forcings and feedbacks associated with anthropogenic climate change (*Pendergrass* 2020, *Pendergrass and Hartmann* 2014).

All of these thermodynamic constraint frameworks are highly idealized. For example: Baroclinic eddies modify the background state against which diffusive frameworks claim they propagate (e.g., *Schneider and Walker* 2006), and radiative fluxes are modified by the circulation adjustments that radiative constraints claim to govern (e.g., *Armour et al.* 2019). Likewise, the global average Clausius-Clapeyron response actually reflects competing, regionally compensating changes in specific humidity (*Rose and Rencurrel* 2016), and is countered by modest relative humidity reductions (*Byrne and O'Gorman* 2016, *Sherwood et al.* 2010). Nevertheless, thermodynamic constraints have proved successful for understanding future circulation changes from simple thermodynamic starting points, despite the seemingly intractable complexities of coupled dynamic-thermodynamic processes (*Shaw* 2019). So far, most GCM experiments that leverage thermodynamic constraints

rely upon passive cooling or heating terms that are independent from the warming response (*Butler et al.* 2010, 2011, *Li et al.* 2019, 2020). Other experiments that permit interactivity via climate feedbacks rely upon one-dimensional energy balance models rather than GCMs (*Armour et al.* 2019, *Huang and Zhang* 2014, *Hwang and Frierson* 2010, *Zelinka and Hartmann* 2012). Chapter 2 presents an idealized modeling framework that lets us directly assess the role of climate feedbacks on the large-scale circulation and its response to global warming – without relying upon idealized, fixed-diffusivity energy balance models or non-interactive, patterned forcing terms (*Shaw* 2019, *Shaw and Tan* 2018). Chapter 3 then discusses a set of experiment results based on this framework and interprets the results using the diffusive and energetic constraints discussed above.

1.3 Climate feedbacks

The temperature and radiative responses to forcing perturbations are most often assessed using forcing-feedback frameworks (Section 1.1; Figure 1.1, top). There are many variants of this framework – however in general, each version expresses the energetic response to notionally constant forcing perturbations (Figure 1.1, top right) using linearizations about the temperature response (Figure 1.1, top left). This can be written as:

$$\Delta N - \Delta F - H = \Delta R = \lambda \Delta T + \mathcal{O}(\Delta T^2) \tag{1.1}$$

where H is the forcing perturbation, ΔF is the heating by anomalous atmospheric motions, ΔN is the anomalous energy imbalance, ΔR is the energetic response, ΔT is the temperature response (e.g., the *climate sensitivity*), and λ is a linear scaling factor (e.g., the *radiative climate feedback*). The $\mathcal{O}(\Delta T^2)$ term represents the non-linear terms neglected by the linearization (e.g., *Bloch-Johnson et al.* 2021, *Knutti and Rugenstein* 2015). The forcing perturbation, energy imbalance, and energetic response are typically evaluated with radiative flux across an upper boundary (e.g., the tropopause or top-of-atmosphere), and the temperature response is typically evaluated at the surface. Most simply, Equation 1.1 is a scalar function of the global average radiative re-

sponse and global average temperature response (e.g., *Hansen et al.* 1985, *Roe* 2009, *Rugenstein and Armour* 2021). However it can also be defined regionally using either 1) local radiative responses to local surface temperature (*Armour et al.* 2012, *Boer and Yu* 2003a,b, *Feldl and Roe* 2013a, *Hedemann et al.* 2022), 2) local radiative responses to zonal or global average surface temperature (*Andrews et al.* 2015, *Feldl and Roe* 2013a, *Hedemann et al.* 2022, *Senior and Mitchell* 2000, *Uribe et al.* 2022), 3) using tropical tropospheric temperature instead of surface temperature (*Ceppi and Gregory* 2017, 2019, *Fueglistaler* 2019, *Fueglistaler and Silvers* 2021), or 4) using explicit estimates of the circulation-adjusted radiative response to regional surface temperature change (*Bloch-Johnson et al.* 2020, *Dong et al.* 2019, 2020, *Zhou et al.* 2017).

While we have developed a much deeper understanding of the processes that guide radiative forcing perturbations and radiative climate feedbacks, the uncertainty in our estimates of these processes and their consequent effects on climate sensitivity have narrowed only slightly (*Charney et al.* 1979, *Masson-Delmotte et al.* 2021, *Roe and Baker* 2007, *Sherwood et al.* 2020, *Stocker et al.* 2013). Further complicating this picture, climate sensitivity estimates from the most recent Coupled Climate Model Intercomparison Project (CMIP6; *Eyring et al.* 2016, *Masson-Delmotte et al.* 2021) are substantially higher and have more inter-model spread than those derived from the previous model inter-comparison project (CMIP5; *Taylor et al.* 2012, *Zelinka et al.* 2020). The increased sensitivity of CMIP6 models has been attributed to more positive extratropical and subtropical shortwave cloud feedbacks in the absence of compensating radiative forcing changes (*Lutsko et al.* 2022, *Zelinka et al.* 2020). The marked differences in climate sensitivity estimates between CMIP5 and CMIP6 underscore the critical need to better understand and constrain climate feedback processes. In particular, this will require a greatly improved understanding of the circulation-mediated surface warming patterns that guide the evolution of the global-average radiative response, commonly called *pattern effects* (*Stevens et al.* 2016).

A rapidly growing body of work has shown that pattern effects exert a strong influence on the global climate feedback parameter (*Andrews et al.* 2015, *Armour et al.* 2012, *Dong et al.* 2020, *Lee et al.* 2022, *Senior and Mitchell* 2000). The circulation helps guide these patterns through changes

to the tropical Walker circulation (*Heede et al.* 2020, *Lu et al.* 2021, *Merlis and Schneider* 2011, *Seager et al.* 2019), atmospheric teleconnections between the tropics and extratropics (*Alexander et al.* 2002, *Dong et al.* 2022, *Kay et al.* 2012, *Kim et al.* 2022, *Luongo et al.* 2023), and ocean heat update and transport adjustments (*Armour et al.* 2016, *Clement et al.* 1996, *Hwang et al.* 2017, *Winton et al.* 2010, *Zhang and Li* 2014, *Zhang et al.* 2019). Many studies on warming pattern effects are motivated by the discrepancy between 1) observed historical warming patterns, which exhibit strong West Pacific warming and moderate East Pacific cooling (*Chung et al.* 2019, *Coats and Karnauskas* 2017, *Heede and Fedorov* 2023), and 2) model-simulated warming patterns, which generally exhibit increasingly amplified East Pacific warming as the climate equilibrates (*Chung et al.* 2019, *Dong et al.* 2020, *Heede and Fedorov* 2021, *Lee et al.* 2022). Since West and East Pacific amplification are associated with vastly different global climate feedbacks (*Andrews and Webb* 2018, *Andrews et al.* 2015, 2022, *Dong et al.* 2019), this discrepancy affects inferences of future warming from the historical record (*Armour* 2017, *Dessler* 2020, *Dong et al.* 2021, *Marvel et al.* 2018). The future of the Pacific warming pattern (and, thus, the magnitude of expected global warming) depends on whether the current West Pacific amplification represents a forced response associated with increasing CO_2 (*Cane et al.* 1997, *Seager et al.* 2019) or a temporary, transient response. A transient historical West Pacific amplification might be intrinsic to the climate system (*Heede et al.* 2020, 2021), or might be due to either unusual internal decadal variability (*Heede and Fedorov* 2023, *Olonscheck et al.* 2020, *Watanabe et al.* 2021, *Xie et al.* 2016), volcanic or anthropogenic sulfate aerosol cooling (*Gregory et al.* 2019, *Heede and Fedorov* 2021, *Smith et al.* 2021, *Takahashi and Watanabe* 2016), or locally-forced Southern Ocean cooling (*Gjermundsen et al.* 2021, *Hartmann* 2022, *Zhang et al.* 2019).

To provide some intuition for the fundamental role of pattern effects on the global climate feedback, Figure 1.2 shows results from a simple box model. The model simulates canonical Pacific surface-warming pattern effects on the global climate feedback using three regions with distinct climate feedbacks and distinct ocean heat uptake intensities (*Rohrschneider et al.* 2019). The regions are independent, with regional feedbacks representing (for example) the local feedback

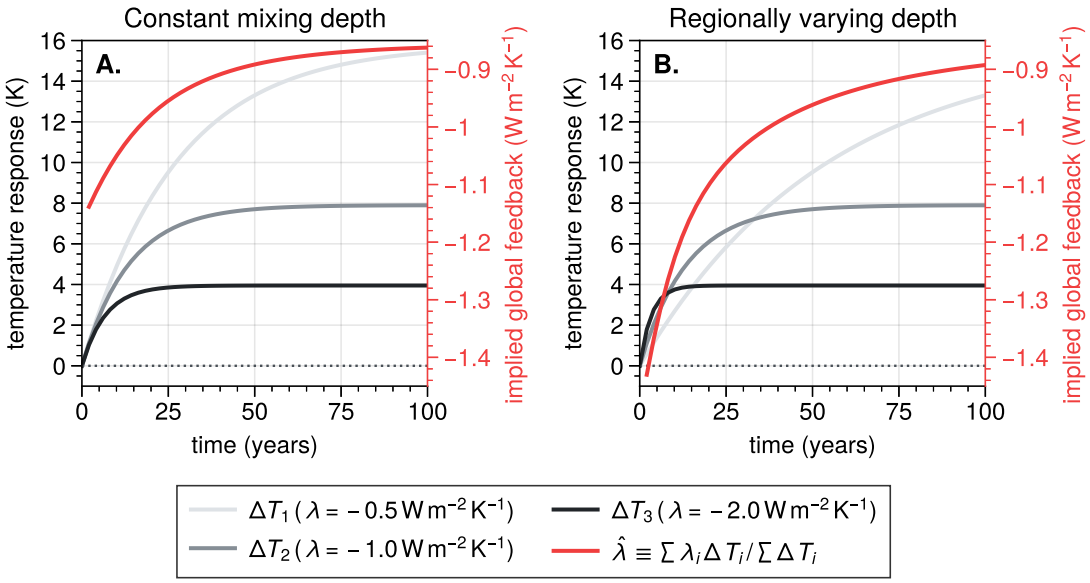

Figure 1.2: Idealized box model for pattern effects on the global climate feedback. The gray lines indicate the first 100 years of the temperature response for each separate region (left y-axis), calculated from analytic solutions to the ordinary differential equation from the main text – i.e., $\Delta T(t) \equiv -(H/\lambda)(1 - \exp((\lambda/C)t)$. The light gray, medium gray, and dark gray lines correspond to regions with feedbacks of $\lambda_1 = -0.5\,\mathrm{W\,m^{-2}\,K^{-1}}$, $\lambda_2 = -1\,\mathrm{W\,m^{-2}\,K^{-1}}$, and $\lambda_3 = -2\,\mathrm{W\,m^{-2}\,K^{-1}}$, respectively (see legend). The red line indicates the effective global climate feedback parameter $\hat{\lambda}$ at each timestep (right y-axis), defined as the average radiative response divided by the average temperature response across the three regions – i.e., $\hat{\lambda}(t) \equiv (\lambda_1 \Delta T_1 + \lambda_2 \Delta T_2 + \lambda_3 \Delta T_3)/(\Delta T_1 + \Delta T_2 + \Delta T_3)$. Panel A shows a simulation with constant ocean mixing depths of $100\,\mathrm{m}$. Panel B shows a simulation where the mixing depths are correlated with the feedbacks; the light gray, medium gray, and dark gray lines correspond to mixing depths of $200\,\mathrm{m}$, $100\,\mathrm{m}$, and $50\,\mathrm{m}$, respectively. Note that as far as the surface energy budget is concerned, net ocean heat uptake is interchangeable with increased ocean heat transport divergence (e.g., *Held and Soden* 2006). Thus, the increased mixing depth in the region with weak feedbacks (light gray line) may also be analogous to an enhanced cooling effect of deep water upwelling due to advection across the steeper thermocline associated with transient upper-ocean warming (e.g., *Yang and Wang* 2009).

parameters of *Armour et al.* (2012) or the circulation-adjusted Green's functions of *Zhou et al.* (2017) and *Dong et al.* (2019). They evolve according to the simple forcing-feedback expression $C\,\mathrm{d}T/\mathrm{d}t = \lambda\Delta T + H$ where t is time, T is local temperature, C is the local heat capacity, λ is the local climate feedback, and $H = 7.9\,\mathrm{W\,m^{-2}}$ is a forcing perturbation matching a recent estimate from CO_2-quadrupling experiments (*Smith et al.* 2020). The regions are also coupled to a hypothetical ocean that instantaneously mixes heat to a fixed "depth," such that C is evaluated from the combined heat capacities of the upper ocean and the atmospheric column (i.e., $C = c_\mathrm{w}\rho_\mathrm{w}d + c_p p_\mathrm{s}/g$, where $c_\mathrm{w} = 4182\,\mathrm{J\,kg^{-1}\,K^{-1}}$ is the specific heat capacity of water, $\rho_\mathrm{w} = 997\,\mathrm{kg\,m^{-3}}$ is the density of water, $d = 100\,\mathrm{m}$ is the upper ocean depth, $c_p = 1004\,\mathrm{J\,kg^{-1}\,K^{-1}}$ is the atmospheric heat capacity at constant pressure, $p_\mathrm{s} = 101325\,\mathrm{kg\,m^{-1}\,s^{-2}}$ is the atmospheric surface pressure, and $g = 9.81\,\mathrm{m\,s^{-2}}$ is the standard gravitational acceleration). The use of a hypothetical ocean extends the timescale of the response to something resembling a typical $4\times CO_2$ response (see x-axis). Under constant mixing depth (Figure 1.2, A), the model produces initially uniform warming followed by slow amplification in the region with weak feedbacks (A, gray lines), resulting in a moderate pattern effect on $\hat{\lambda}$ (A, red line, right y axis). This is analogous to homogeneous tropical Pacific warming followed by East Pacific amplification. Under feedbacks with correlated mixing depths (Figure 1.2, B), the model produces fast amplified warming in the region with strong feedbacks (B, dark gray line) followed by slow amplified warming in the region with weak feedbacks (B, light gray line), resulting in a large pattern effect on $\hat{\lambda}$ (B, red line, right y axis). This is analogous to West Pacific amplification followed by East Pacific amplification.

The rapidly growing literature on pattern effects and the above conceptual model results point to the critical role of surface warming patterns on the global climate response – whether as an intrinsic response to increasing CO_2, or through transient, external influences on warming patterns. It also reaffirms the need to understand links between climate feedbacks and the atmospheric circulation in order to constrain not just the circulation response to global warming, but also the magnitude of global warming itself: The circulation influences "intrinsic" pattern effects (Figure 1.2) by determining the magnitudes of regional climate feedbacks (e.g., by guiding circulation-adjusted

global radiative responses to regional temperature changes; *Dong et al.* 2019, *Zhou et al.* 2017), while the circulation influences "external" pattern effects by setting large-scale modes of decadal variability and guiding teleconnection responses to regional, transient climate forcings (e.g., *Dong et al.* 2022, *Hartmann* 2022, *Kim et al.* 2022). Chapters 4 and 5 explore these circulation effects by comparing results across ensembles of coupled climate models. This allows us to develop constraints on model estimates of global climate feedbacks and test hypotheses for the role of the global circulation on shaping global climate feedbacks.

Chapter 2

Dynamical core: Theory

2.1 Thermal relaxation timescales

The *dynamical core* represents the component of any general circulation model (GCM) that evaluates the primitive equations on a rotating sphere. *Held and Suarez* (1994) first proposed comparing dynamical cores of GCMs by replacing all entropy-increasing physics with linear relaxation terms; the resulting simplified models are called *dynamical core models*. Since their pioneering paper, dynamical core models have been used to explore a wide range of problems in extratropical variability (e.g., *Boljka et al.* 2018, *Chen et al.* 2020), as well as the extratropical circulation responses to stratospheric cooling (*Kushner and Polvani* 2004, 2006), tropical heating (*Butler et al.* 2010, *Lu et al.* 2014, *Mbengue and Schneider* 2013, *Sun et al.* 2013), and variations in boundary layer friction (*Chen et al.* 2007). In these two chapters, I use a dynamical core model to probe the relationships between climate feedbacks, climate sensitivity, and the global circulation – both its unperturbed climatology, and its response to external forcing perturbations. I accomplish this by exploiting the close analogy between the relaxation term used in the thermodynamic equation of a dynamical core model and the canonical definition of the climate feedback parameter.

To clarify the analogy, consider the thermodynamic equation of state for a dynamical core atmosphere where all diabatic processes are parameterized as a linear relaxation of the temperature field (*Held and Suarez* 1994):

$$N = F + Q = F - C\left(\frac{T - T^{\mathrm{e}}}{\tau}\right). \tag{2.1}$$

Above, T is the air temperature; F is the heat transport convergence; $N \equiv C(\partial T/\partial t)$ is the transient energy imbalance; $Q \equiv -C\left(T - T^{\mathrm{e}}\right)/\tau$ is the thermal relaxation rate (i.e., the diabatic heating rate), which I call the *thermal forcing*; T^{e} is the *equilibrium temperature*; τ is the *thermal relaxation timescale*; and $C = c_p/g$ is the heat capacity density (where c_p is the specific heat

capacity at constant pressure and g is the acceleration due to gravity). The units of of N, F, and Q are $\mathrm{W\,m^{-2}\,Pa^{-1}}$, and the units of C are $\mathrm{J\,m^{-2}\,Pa^{-1}\,K^{-1}}$. The equilibrium temperature and thermal relaxation timescale are both defined as a function of latitude and height (i.e., they are zonally symmetric).

Now consider Equation 2.1 for two climate states with identical equilibrium temperature profiles: 1) a control climate in which the only forcing terms are the heat transport convergence F and the thermal relaxation rate Q; and 2) a perturbed climate additionally forced by the forcing perturbation H on the RHS of Equation 2.1. Taking the difference between these equations and rearranging terms yields

$$\Delta N - \Delta F - H = \Delta Q = -\frac{C}{\tau}\Delta T \tag{2.2}$$

where ΔN, ΔF, ΔQ, and ΔT are the differences in energy imbalance, heat transport convergence, thermal forcing, and air temperature between the two states. Comparing Equation 2.2 to Equation 1.1, it is clear that the ratio of the heat capacity to the thermal relaxation timescale is analogous to the local climate feedback parameter λ in dynamical core models. I call this term the *relaxation feedback parameter* λ_τ, defined

$$\lambda_\tau = -\frac{C}{\tau}. \tag{2.3}$$

Even though λ_τ uniquely determines the climate feedbacks in dynamical core models, I use the prefix "relaxation" to avoid confusion with climate feedbacks in more complex models. Importantly, since λ_τ is proportional to τ^{-1}, the climate sensitivity implied by λ_τ is proportional to τ (see Figure 3.4, B and Appendix A). An intuition for this proportionality can be gained as follows: If we group the forcing perturbation H into the numerator of the thermal relaxation term $-C(T - T^{\mathrm{e}})/\tau$ (Equation 2.1), it is clear that H can be equivalently expressed as the thermal relaxation timescale-scaled equilibrium temperature perturbation $\Delta T^{\mathrm{e}} \equiv H\tau/C$. Since this equilibrium temperature perturbation is scaled by τ, and since climatological temperature is generally

proportional to equilibrium temperature, it follows that τ must be generally proportional to climate sensitivity.

The central difference between the feedback parameter in complex climate models (λ in Equation 1.1) and the feedback parameter in dynamical core models (λ_τ in Equation 2.2) is that the former is defined with surface temperature and the radiative flux across an upper boundary, whereas the latter is defined with air temperature and the local diabatic heating. Nevertheless, the analogy between λ and λ_τ is important, since it means that we can explicitly prescribe climate feedback parameters in dynamical core models to assess the role of climate feedbacks on the atmospheric circulation. The approach stands in contrast to analyses of fully coupled GCM simulations, in which the feedback parameter cannot be prescribed *a priori* and must instead by diagnosed *a posteriori*.

2.2 Coupled model comparisons

For the dynamical core model experiments, I use three globally-averaged quantities to quantify the sensitivity of each configuration to forcing perturbations (see Appendix A for details):

1. The *reference thermal relaxation timescale* $\tau_0 = 1/\ \overline{\langle 1/\tau \rangle}$ (Equation A.6), defined as the inverse average of the inverse thermal relaxation timescale over the entire atmosphere (where the single overbar denotes a horizontal average and the single angle brackets denote a vertical average).

2. The *relaxation sensitivity parameter* $s_\tau = -1/\overline{\langle\!\langle \lambda_\tau \rangle\!\rangle} = \tau_0 / C_0$ (Equation A.6), equivalent to the negative inverse of the horizontally averaged, vertically integrated relaxation feedback parameter (where the double angle brackets denote a vertical integral and C_0 is the heat capacity of the full atmospheric column). This represents the climate sensitivity per unit forcing under the assumption of spatially uniform warming.

3. The *relaxation climate sensitivity* $\Delta T_\tau = -\overline{\langle\!\langle H \rangle\!\rangle} / \overline{\langle\!\langle \lambda_\tau \rangle\!\rangle} = \overline{\langle\!\langle H \rangle\!\rangle}\, \tau_0 / C_0$ (Equation A.7), equivalent to the product of the relaxation sensitivity parameter and the horizontally averaged, vertically integrated forcing perturbation. This represents the climate sensitivity under

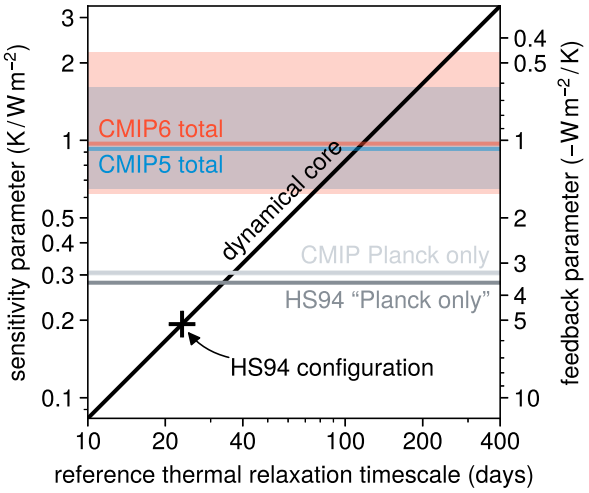

Figure 2.1: Climate sensitivity and the thermal relaxation timescale. (black, solid) The relaxation sensitivity parameter s_τ as a function of the reference thermal relaxation timescale τ_0 in a dynamical core model, with the *Held and Suarez* (1994; hereafter HS94) configuration indicated by the plus marker. (dark gray) The Planck climate sensitivity parameter from the HS94 configuration, using the atmosphere-average temperature as the "emission" temperature (see Appendix A and Equation A.8). (light gray) The Planck climate sensitivity parameter diagnosed from the consensus of CMIP abrupt $4\times CO_2$ experiments ($s_0 \approx 0.3\,\mathrm{K}\,/\,\mathrm{W\,m^{-2}}$, $\Delta T_0 \approx 1.2$K; *Zelinka et al.* 2020). (blue and red) The mean (solid lines) and 5-95 percentile range (shading) net climate sensitivity parameter diagnosed from the CMIP5 (blue) and CMIP6 (red) abrupt $4\times CO_2$ experiments (*Zelinka et al.* 2020). The right y-axis shows the feedback parameter λ associated with each sensitivity parameter s (i.e., the negative inverse sensitivity parameter).

the assumption of spatially uniform warming. Empirical measures of the climate sensitivity generally scale with ΔT_τ under the same forcing and feedback patterns (see Section 3.2 and Figure 3.4, B).

I also use the relaxation feedback parameter λ_τ (Equation 1.1) to quantify the strength of the local climate feedbacks. Specifically, I argue that λ_τ can be viewed as the dynamical core-equivalent of the net radiative feedback kernel K (see Appendix A and Equation A.4). Before proceeding with the experiment results, I consider how s_τ and λ_τ calculated from typical configurations of dynamical core models (see Appendix A.4) compare with more conventional derivations of the climate sensitivity parameter and radiative feedback kernels.

Figure 2.1 shows the relationship between the relaxation sensitivity parameter s_τ and the reference thermal relaxation timescale τ_0 (solid black line). Under the common *Held and Suarez* (1994; hereafter HS94) configuration used with dynamical core models (Appendix A.4), the relaxation

sensitivity parameter s_τ is approximately $0.2\,\mathrm{K}\,/\,\mathrm{W\,m^{-2}}$ (Figure 2.1, dashed black line). This is lower than consensus estimates from versions 5 and 6 of the Coupled Model Intercomparison Project (CMIP), as the HS94 configuration was not designed with the goal of producing a realistic climate sensitivity. To match the CMIP estimates, the reference relaxation timescale would need to be on the order of 100 days rather than 20 days (Figure 2.1, blue and red lines and shading; *Zelinka et al.* 2020). Notably, the HS94 relaxation sensitivity parameter is also lower than two separate estimates of the Planck sensitivity parameter: The first obtained from CMIP simulations of global warming (*Zelinka et al.* 2020), the second from applying the Stefan-Boltzmann Law to climatological temperatures under the HS94 configuration (see Equation A.8). Both Planck estimates imply a reference thermal relaxation timescale on the order of 40 days rather than 20 days (Figure 2.1, gray lines). Figure 2.1 motivates us to study the effects of longer relaxation timescales on the large-scale circulation (Section 3.1).

Figure 2.2 compares the latitude-height profile of the HS94 relaxation feedback parameter λ_τ (Figure 2.2, D) against clear-sky temperature, specific humidity, and combined temperature-specific humidity radiative feedback kernels (Figure 2.2, A–C; see Equation A.5) estimated by *Huang et al.* (2017) from the ERA-Interim reanalysis data set (*Dee et al.* 2011). Figure 2.3 also shows vertical integrals of the feedback kernels from Figure 2.2. The specific humidity radiative kernel is scaled by the specific humidity change associated with a 1 K temperature perturbation under constant relative humidity, consistent with the Clausius-Clapeyron relation (e.g., *Held and Soden* 2006). The average magnitude of the relaxation feedback parameter given by the HS94 configuration is about 25% that of the combined temperature-specific humidity ERA-Interim radiative kernel (Figure 2.2, C–D; note the separate color scales), or about 50% when the surface temperature radiative kernel is included (compare black and solid red, Figure 2.3; note the HS94 values are scaled by 0.5). These results are more-or-less consistent with Figure 2.1 (compare black cross with blue and red lines, right y-axis). But notably, the spatial pattern of the HS94 relaxation feedback parameter compares favorably with that of the temperature-specific humidity radiative kernel in the lower and middle troposphere (Figure 2.2, C–D). Both are characterized by a weakly

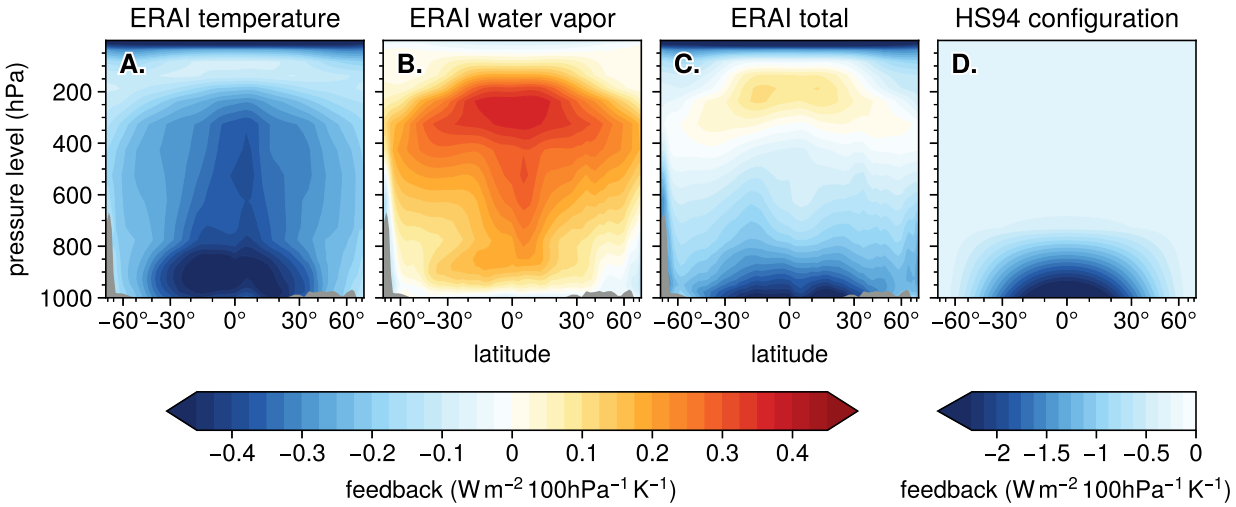

Figure 2.2: Radiative feedback kernels and the thermal relaxation timescale. (A) The annual-mean zonal-mean air temperature radiative feedback kernel K_T from the ERA-Interim reanalysis data set (ERAI; *Dee et al.* 2011), estimated as the top-of-atmosphere radiative response to a 1 K temperature perturbation as a function of the latitude and height of the applied perturbation (*Huang et al.* 2017). The radiative response is normalized by the average pressure thickness of the perturbed model level, and only the clear-sky component of the response is shown (i.e., cloud radiative effects were excluded from the radiative transfer calculations; *Huang et al.* 2017). Pressures above the 0.33 quantile surface pressure are masked out with gray, and the *x*-axis is scaled by a sine function so that equal distances along the axis correspond to equal spherical surface areas. (B) As in A, but for the radiative response to the specific humidity perturbations required for a constant-relative humidity response to a 1 K temperature perturbation. This represents the specific humidity radiative feedback kernel K_q multiplied by the Clausius-Clapeyron scaling $\partial q / \partial T$ (Equation A.5); thus, the units also have Kelvin in the denominator. (C) As in A, but for the combined temperature-specific humidity radiative feedback kernel $K_{T,q}$ (equivalent to the sum of panels A and B; Equation A.5). (D) The relaxation feedback parameter $\lambda_\tau = -c_p / g\tau$ from the *Held and Suarez* (1994) configuration (please note the distinct color scale).

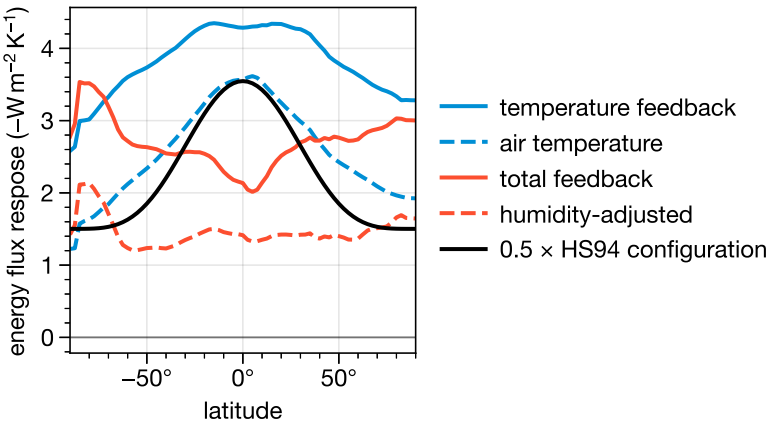

Figure 2.3: As in Figure 2.2 but showing vertically-integrated values. The blue lines indicate pure temperature feedback kernels (Figure 2.2, A). The red lines indicate combined temperature and relative humidity-preserving water vapor feedback kernels (Figure 2.2, C). The solid lines (dashed lines) include (exclude) the surface temperature radiative kernel from *Huang et al.* (2017). The black line indicates the vertically integrated relaxation feedback parameter $\lambda_\tau = -c_p/g\tau$ from the *Held and Suarez* (1994) configuration (scaled by 0.5).

negative feedback throughout the middle troposphere and much stronger negative feedbacks in the lower troposphere at low latitudes.

The ERA-Interim radiative feedback kernel is locally amplified due to the combined effects of a strong vertical gradient in the scaled specific humidity radiative kernel and a strong meridional gradient in the temperature radiative kernel (Figure 2.2, A–B). By contrast, the HS94 relaxation feedback parameter was locally amplified by *Held and Suarez* (1994) in order to match real-world circulation statistics and thermal stratification. It is not entirely clear whether the goal of producing a realistic steady-state climate necessarily guarantees a realistic pattern of relaxation feedback parameters, or whether the resemblance of the HS94 relaxation feedback parameters to the clear-sky radiative feedback kernel is a coincidence. Regardless, as shown later, the non-uniformity of the relaxation feedback parameter turns out to play a critical role in governing the circulation response to horizontally uniform forcing perturbations (Section 3.2).

2.3 Experimental design

To study the effects of relaxation climate sensitivity on the large-scale circulation, I designed two experiments. The first experiment tests the influence of relaxation climate sensitivity on the unperturbed steady-state circulation (hereafter, the *unperturbed* experiment), while the second experiment tests the influence of relaxation climate sensitivity on the response of the circulation to a horizontally uniform forcing perturbation (hereafter, the *perturbed* experiment).

The unperturbed experiment consists of control-like simulations with relaxation climate sensitivity (i.e., thermal relaxation timescales) varying across three orders of magnitude. I first ran the model with the latitude-height fields of the equilibrium temperature and thermal relaxation timescale configured according to HS94 (Figure 2.4, A–B; see Appendix A.4). In the HS94 configuration, the equilibrium temperature T^{e} is characterized by large meridional temperature gradients, a statically neutral lapse rate at the poles, and a statically stable lapse rate at the equator (Figure 2.4, A; Equation A.9); the thermal relaxation timescale τ is characterized by a minimum of $\tau_{\mathrm{min}} = 4$ days at the surface on the equator and a maximum of $\tau_{\mathrm{max}} = 40$ days above $\sim$700 hPa and at the poles (Figure 2.4, B; Equation A.10). I then perturbed the relaxation climate sensitivity by uniformly scaling the thermal relaxation timescale τ; the maximum relaxation timescale τ_{max} used with each simulation was 0.4, 1, 2, 4, 10, 20, 30, 40, 50, 60, 80, 100, 120, 160, 200, and 400 days, and the minimum relaxation timescale τ_{min} was always one tenth the maximum relaxation timescale τ_{max} (consistent with HS94; Equation A.10).

A similar set of unperturbed dynamical core experiments was discussed previously (*Davis* 2019). However, while *Davis* (2019) used a wide variety of eddy-mean flow interaction frameworks to assess the effects of forcing configurations on the circulation (including diagnostics for eddy propagation and dissipation, metrics for energy transfer between eddies and the background flow, and analyses of large-scale annular modes; *Eliassen* 1960, *Lorenz* 1955, *Thompson and Wallace* 2000), the results presented in this thesis focus on the ability of simpler thermodynamic constraints to account for differences in the unperturbed circulation. These same frameworks are then used to interpret model responses to forcing perturbations. Further, while *Davis* (2019) provided

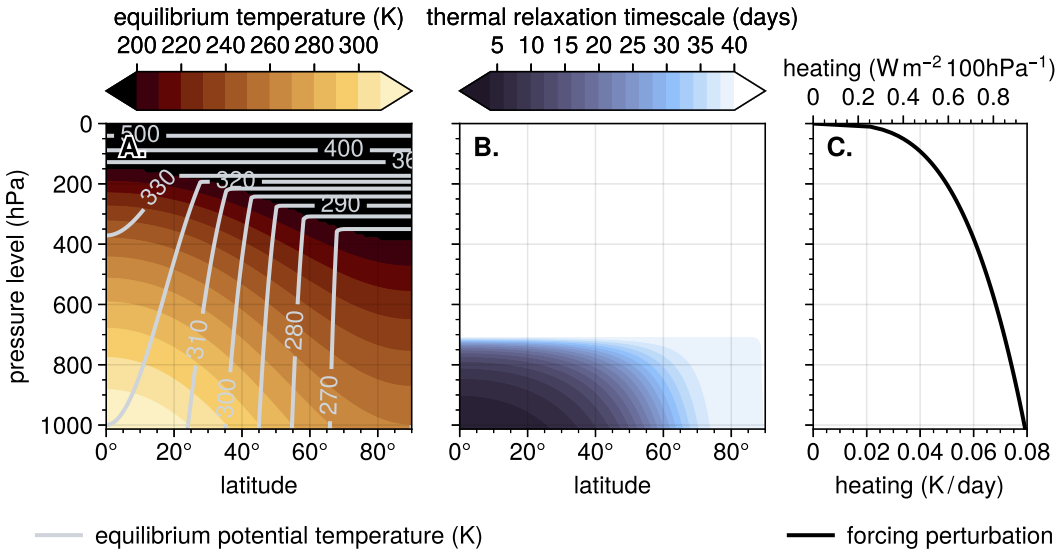

Figure 2.4: Dynamical core model forcing terms. Latitude-height cross-sections of the (A) equilibrium temperature T^{e} and (B) thermal relaxation timescale τ used to drive thermal forcing under the *Held and Suarez* (1994) configuration of a dynamical core model (Equations A.9 and A.10). The light gray contours in panel A indicate the potential temperatures $\theta^{\mathrm{e}} \equiv T^{\mathrm{e}}(p_0/p)^{\kappa}$ associated with the equilibrium temperature field. (C) Vertical profile of the "global warming" thermal forcing perturbation H (Equation 2.4).

a more heuristic statement of the relationship between global relaxation timescales and global climate sensitivity, this thesis emphasizes the much closer analogy between local thermal relaxation timescales and radiative feedback kernels. I later leverage this analogy to aid in the interpretation of both the unperturbed and perturbed experiment results (Chapter 3) and to develop proposals for future model hierarchy experiments with prescribed climate feedbacks (Chapter 6).

The perturbed dynamical core experiment consists of simulations with forcing perturbations imposed upon a subset of the unperturbed simulations. Since it is not possible to increase the optical depth or greenhouse gas concentrations of a dynamical core model, I instead perturbed the model with a horizontally uniform, vertically decaying forcing perturbation H (Figure 2.4, C) analogous to a greenhouse gas radiative forcing perturbation:

$$H = h_0 C \left(\frac{p}{p_0} \right)^{\kappa} \tag{2.4}$$

Above, p is the pressure, $p_0 \equiv 10^5\,\mathrm{Pa}$ is the reference pressure, h_0 is the reference heating in units $\mathrm{K}\,/\,\mathrm{day}$, $C = c_p/g$ is the heat capacity density (see Equations 2.1 and 2.2), and $\kappa \equiv R_{\mathrm{d}}/c_p$ is the

Poisson constant (where R_d is the dry air gas constant). The vertical structure of the perturbation is designed to mimic the effect of perturbing the global average surface equilibrium temperature $\overline{T}_\mathrm{s}^\mathrm{e}$ (compare Equation 2.4 with Equation A.9). The reference heating h_0 was set to 0.079 K / day, such that the vertically integrated forcing perturbation is equivalent to the CMIP5 consensus for the radiative forcing perturbation due to an instantaneous quadrupling of CO_2 (*Andrews et al.* 2012): $\langle\!\langle H \rangle\!\rangle = h_0 p_0 C (p_\mathrm{s}/p_0)^{\kappa+1} (\kappa+1)^{-1} = 7.4 \text{ W m}^{-2}$, where $p_\mathrm{s} = 101325 \,\mathrm{Pa}$ is the global average surface pressure and the double angle brackets denote a vertical integral.

I used the forcing perturbation H rather than a perturbation in the global average surface equilibrium temperature $\overline{T}_\mathrm{s}^\mathrm{e}$ (Equation A.9) because the magnitude of the response to any equilibrium temperature perturbation ΔT^e is independent of relaxation climate sensitivity. It can be seen from Equations 2.1 and 2.2 that the perturbation ΔT^e leads to the feedback-dependent heating $\hat{H} = -\lambda_\tau \Delta T^\mathrm{e}$. Since the magnitude of this heating is scaled by the strength of the feedback $\lambda_\tau = -C/\tau$, the temperature response is always roughly the same. The constant heating term H is thus more appropriate than the feedback-dependent heating term $\hat{H}$ for investigating links between relaxation climate sensitivity and the large-scale circulation.

Chapter 3

Dynamical core: Experiments

3.1 Unperturbed circulation

In the previous chapter, I established a framework for interpreting climate forcings and climate feedbacks in the dynamical core model, finding that the thermal relaxation timescale τ is largely responsible for setting the climate sensitivity of the model. I also proposed a set of simple experiments for explicitly testing the influence of these feedbacks on both *unperturbed* global circulations and *perturbed* responses to external forcings. I summarize the steady-state results of these experiments using 5000-day climatological averages for a dynamical core model with moderately high resolution (see Appendix A.4 for details).

Figure 3.1 summarizes the climatological large-scale circulation under different relaxation climate sensitivities. In general, lower relaxation climate sensitivities (i.e., shorter thermal relaxation timescales) are associated with stronger thermal forcing (i.e., larger thermal relaxation rates; Figure 3.1, D-F, shading), increased baroclinicity (Figure 3.1, A-C, shading), intensified eddy static energy transport (Figure 3.1, D-F, contours), and a faster jet stream (Figure 3.1, A-C, black contours). That is, reducing the relaxation climate sensitivity of a dynamical core model tends to invigorate the large-scale circulation. This relationship arises from the dual role of relaxation climate sensitivity in governing both the strength of the forcing toward the baroclinically unstable equilibrium state (Figure 2.4, A; Equation A.9) and the amplitude of the temperature anomalies resulting from external forcing perturbations.

For example, consider the climatological thermal forcing $\widetilde{Q}$ in a dynamical core model (Equation 2.1):

$$\widetilde{Q} = -C\left(\frac{\widetilde{T} - T^{\mathrm{e}}}{\tau}\right) \tag{3.1}$$

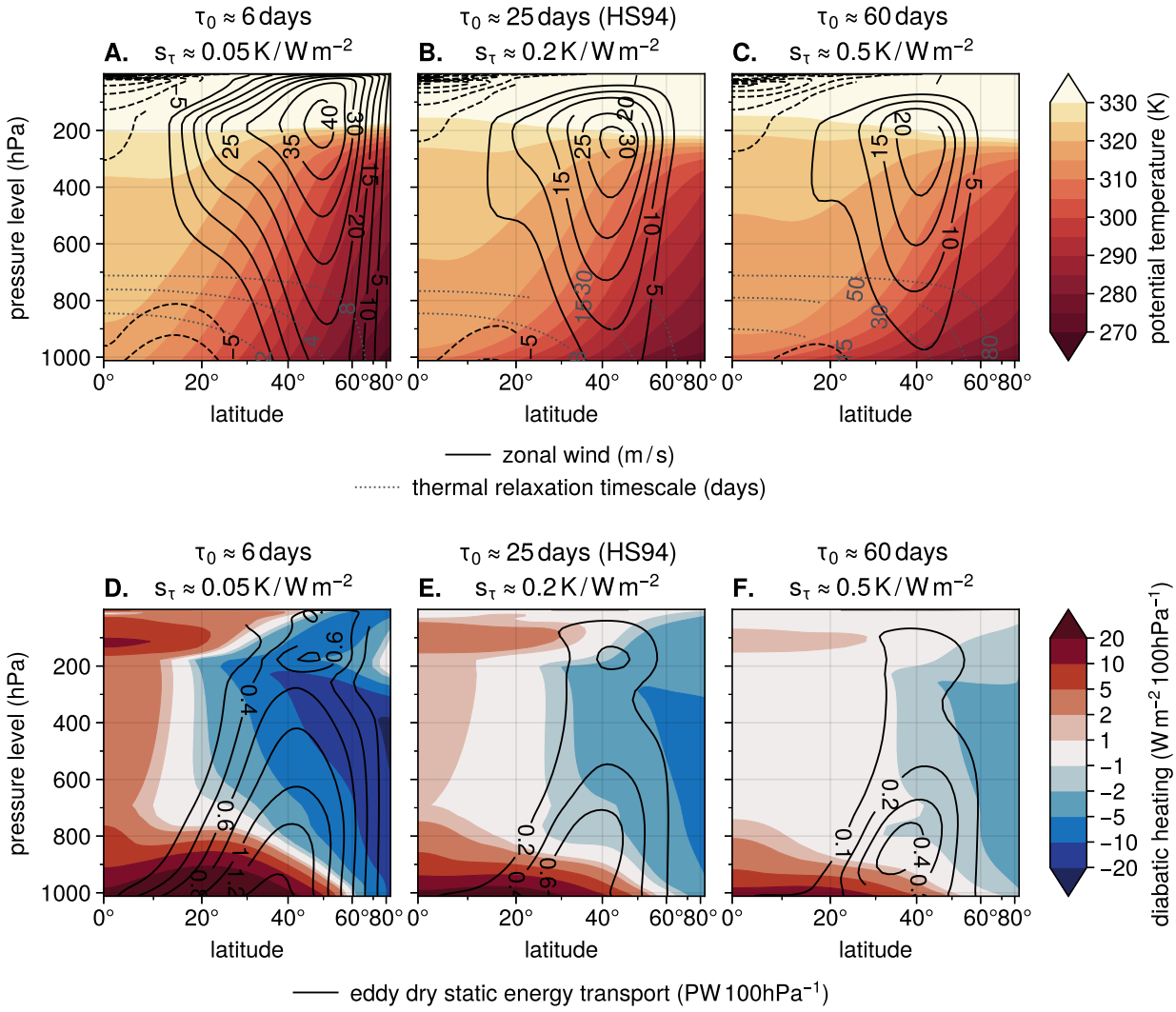

Figure 3.1: Relaxation climate sensitivity and the large-scale circulation. Average latitude-height cross-sections from simulations with relaxation climate sensitivities (A, D) less than, (B, E) equal to, and (C, F) greater than the *Held and Suarez* (1994) relaxation climate sensitivity. The top row (A–C) shows the zonal-mean potential temperature (shading) and zonal wind (contours). The thermal relaxation timescales are shown with gray dotted contours. The bottom row (D–F) shows the zonal-mean diabatic heating rate (i.e., thermal relaxation rate; shading) and eddy static energy transport (contours). The relaxation sensitivity parameters and associated reference thermal relaxation timescales are indicated above each panel.

where the tilde indicates a climatological time average. The direct effect of reducing the relaxation climate sensitivity (and, thus, the thermal relaxation timescale τ) is to amplify the thermal forcing $\widetilde{Q}$ (Figure 3.1, D–F, shading; Figure 3.2, A, dashed line). But there is also an indirect effect, by which reducing τ increases the meridional temperature gradient and decreases the climatological temperature $\widetilde{T}$ at high latitudes (Figure 3.1, A–C, shading), as the static energy transport becomes less effective at wiping out deviations from the equilibrium state T^{e}. Thus, the indirect effect of reducing τ is to suppress the thermal forcing $\widetilde{Q}$ by reducing $\widetilde{T} - T^{\mathrm{e}}$ in the extratropics (Figure 3.2, A, dotted line). Taken together, the direct effect of reducing τ dominates the indirect effect for $\tau \gtrsim 2$ days, as the energy transport by eddies is able to sustain significant deviations from T^{e} (Figure 3.1, D–F, contours; Figure 3.2, A, solid line). The indirect effect is only dominant for $\tau \lesssim 1$ day, where the energy transport is unable to sustain significant deviations from the baroclinically unstable state T^{e} (Figure 3.2, A, solid line). At such short timescales, the relaxation rates exceed the maximum growth rates of baroclinic disturbances, and the energy transport shuts off.

At steady state, the static energy transport responsible for sustaining $\widetilde{T} - T^{\mathrm{e}}$ must balance the associated thermal forcing $\widetilde{Q}$. At high latitudes, the energy transport required to balance $\widetilde{Q}$ is dominated by the eddies rather than the zonal-mean transport (compare solid medium gray and light gray lines, Figure 3.2, B). Notably, the response of the eddy component of the transport to changing relaxation timescales does not follow a simple, constant-diffusivity closure. Instead, reduced relaxation climate sensitivity is associated with increased static energy diffusivity (defined as the ratio of the 850 hPa meridional static energy gradient to the vertically integrated eddy static energy transport; compare solid and dashed medium gray lines, Figure 3.2, B). Since shorter thermal relaxation timescales (i.e., lower relaxation climate sensitivities) tend to amplify the thermal forcing, and since amplified forcing must be balanced by increased energy transport, it is clear in general that lower relaxation climate sensitivity must be associated with a more vigorous large-scale circulation.

The influence of relaxation climate sensitivity on the large-scale circulation is manifest in two key features of the extratropical circulation: The storm track and the eddy-driven jet. Following

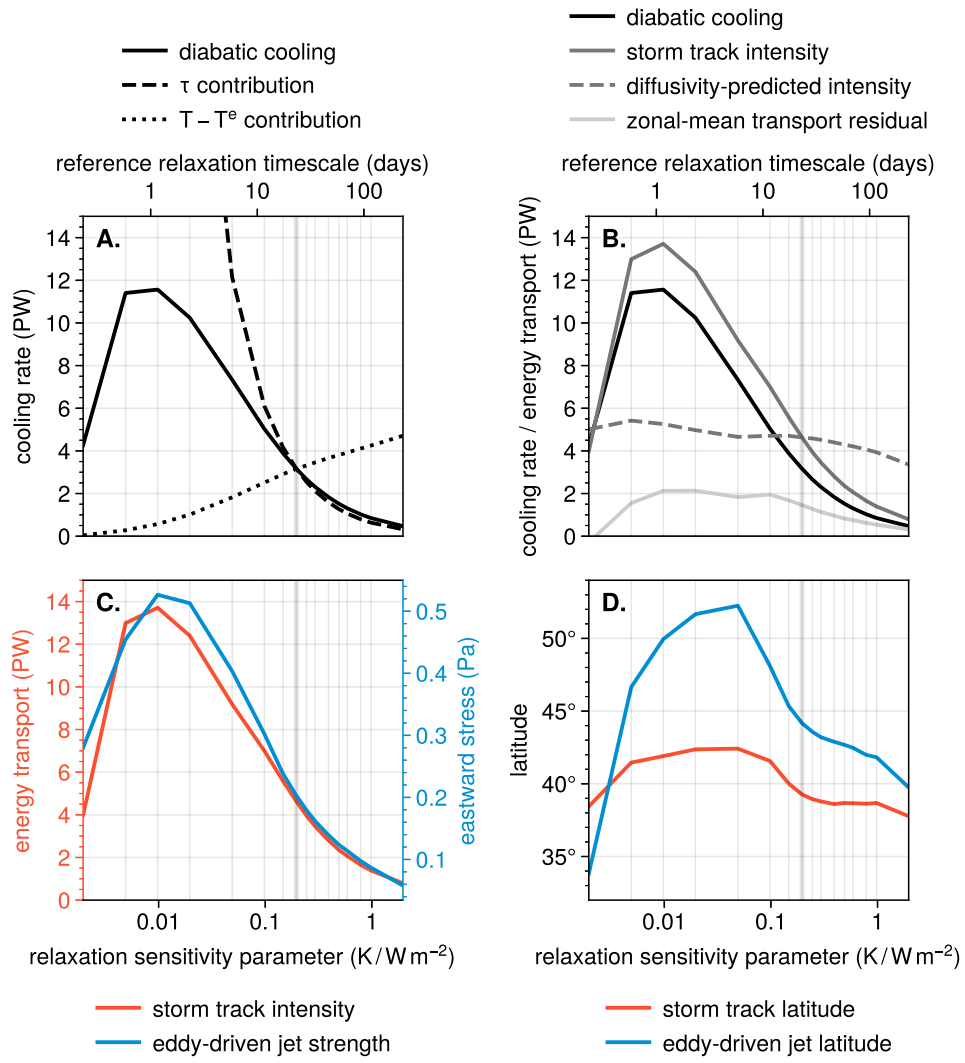

Figure 3.2: Relaxation climate sensitivity and the extratropical circulation. Average extratropical circulation metrics as a function of the relaxation sensitivity parameter s_τ (bottom x-axis) and the reference thermal relaxation timescale τ_0 (top x-axis). (A) The vertically integrated diabatic cooling (i.e., negative thermal relaxation rate) integrated from the storm track to the pole, where the storm track is defined as the maximum vertically integrated eddy static energy transport. The dashed and dotted lines indicate the individual contributions of the denominator and numerator of Equation 2.1 to changes in net cooling relative to the *Held and Suarez* (1994; hereafter HS94) configuration, calculated as the diabatic cooling resulting from setting the climatological temperatures (dashed line) and relaxation timescales (dotted line) to their HS94 values. (B) The diabatic cooling from panel A (black), the storm track intensity (medium gray), and the residual due to energy transport by the zonal-mean circulation (calculated as the storm track intensity minus the diabatic cooling; light gray). The dashed gray line indicates the storm track intensity predicted by the HS94 static energy diffusivity (calculated as the product of the 850 hPa meridional static energy gradient at the storm track with the ratio of storm track intensity to static energy gradient from HS94). (C) The storm track (red) and eddy-driven jet (blue) intensities. (D) The storm track (red) and eddy-driven jet (blue) latitudes. The configurations I explicitly tested are indicated with vertical grid lines, and the HS94 configuration is indicated with the thick vertical grid line. The eddy-driven jet is defined in Section 3.1.

Shaw et al. (2018), I define the *storm track* as the maximum vertically integrated eddy static energy transport $F_{\mathrm{E}} = 2\pi a \cos\phi \left\langle\!\left\langle [v^* s^*] \right\rangle\!\right\rangle$ (where a is the Earth radius; ϕ is the latitude; v is the meridional wind; $s = c_p T + \Phi$ is the static energy, where c_p is the specific heat at constant pressure and Φ is the geopotential; and the square brackets and asterisks denote the zonal average and deviations thereof, respectively). This metric captures the same internal variations as more common storm track metrics (see *Shaw et al.* 2018, Appendix A), but also lets us connect storm track changes to the static energy budget, since the latitudinal maximum in F_{E} must be balanced by the zonal-mean static energy transport $F_{\mathrm{M}} = 2\pi a \cos\phi \left\langle\!\left\langle [v] \right\rangle\!\right\rangle \left\langle\!\left\langle [s] \right\rangle\!\right\rangle$ at the storm track and the thermal forcing Q integrated from the storm track to the pole (*Shaw et al.* 2018; Figure 3.2, solid lines). Note that stationary eddy transport is zero in the HS94 configuration of a dynamical core model since the topography and forcing parameters are zonally uniform. Similarly, I define the *eddy-driven jet* as the maximum vertically integrated eddy angular momentum flux forcing of the zonal-mean zonal wind budget $M_{\mathrm{E}} = \partial_\phi \left(\cos^2\phi \left\langle\!\left\langle [v^* u^*] \right\rangle\!\right\rangle \right) / a \cos^2\phi$. This metric captures the same internal variations as the surface wind maximum definition, but is insensitive to changes in vertical shear within the friction layer (i.e., below $\sim$700 hPa; *Held and Suarez* 1994).

A key result is that the intensities and latitudes of the storm tracks and eddy-driven jets are both dependent on relaxation climate sensitivity (Figure 3.2, C–D). Notably, this dependence is non-monotonic: The storm track and eddy-driven jet intensities are maximized for relaxation climate sensitivities around $s_\tau \approx 0.01\,\mathrm{K\,/\,W\,m^{-2}}$ (i.e., $\tau_0 \approx 1$ day; Figure 3.2, C). At these values, the tendency of strong thermal forcing to invigorate the circulation is countered by its tendency to suppress baroclinic eddy growth. Interestingly, the latitudes of the storm track and eddy-driven jet are maximized for larger relaxation climate sensitivities around $s_\tau \approx 0.05\,\mathrm{K\,/\,W\,m^{-2}}$ (i.e., $\tau_0 \approx 5$ days; Figure 3.2, D). While the storm track and eddy-driven jet intensities scale mostly in tandem across the range of sampled relaxation climate sensitivities (Figure 3.2, C), the eddy-driven jet latitude is much more dependent on relaxation climate sensitivity than the storm track latitude (Figure 3.2, D).

The pronounced influence of relaxation climate sensitivity on the extratropical circulation suggests that the circulation characteristics of more complex models might also be linked to their climate sensitivity. Such relationships could be used to construct *emergent constraints* on multi-model estimates of climate sensitivity (e.g., *Hall et al.* 2019, *Klein and Hall* 2015). We can test the likelihood that a circulation characteristic might serve as a useful emergent constraint by comparing its dependence on relaxation climate sensitivity with its dependence on equilibrium temperature. Since equilibrium temperature is independent from relaxation climate sensitivity (Equation 2.1), a circulation characteristic that is strongly dependent on equilibrium temperature is less likely to be a unique indicator of climate sensitivity. A more realistic analogue for this might be circulation differences arising from model disagreements in climatological radiative heating and cooling rates that are independent of climate sensitivity.

To test the dependence of the circulation on equilibrium temperature, I carried out an additional experiment holding the thermal relaxation timescale fixed and running the model with surface equator-pole equilibrium temperature differences $\Delta_{\mathrm{h}}^{\mathrm{e}}$ of 10, 20, 40, 60, 90, 120, and 150 K (Equation A.9). Figure 3.3 compares extratropical circulation characteristics from the relaxation climate sensitivity experiment (blue lines) and equilibrium temperature experiment (orange lines) as a function of the diabatic cooling integrated from the storm track to the pole (i.e., the black line in Figure 3.2, B). Perturbations in equilibrium temperature clearly lead to significant responses in both the storm track and eddy-driven jet intensity (Figure 3.3, orange lines). Importantly, a nearly identical circulation response results from perturbations in either the equilibrium temperature or relaxation climate sensitivity, as long as their effects on the thermal forcing constraint are identical (compare orange and blue lines, Figure 3.3). This suggests that while relaxation climate sensitivity plays an important role in determining the extratropical circulation, it is unlikely that circulation intensity could be used to construct a useful emergent constraint on climate sensitivity.

By contrast, *isentropic slope* appears to be a potentially useful predictor of climate sensitivity (Figure 3.3, C). Isentropic slope, defined as the meridional slope of potential temperature surfaces, characterizes the extent to which the background state is conducive to baroclinic instabil-

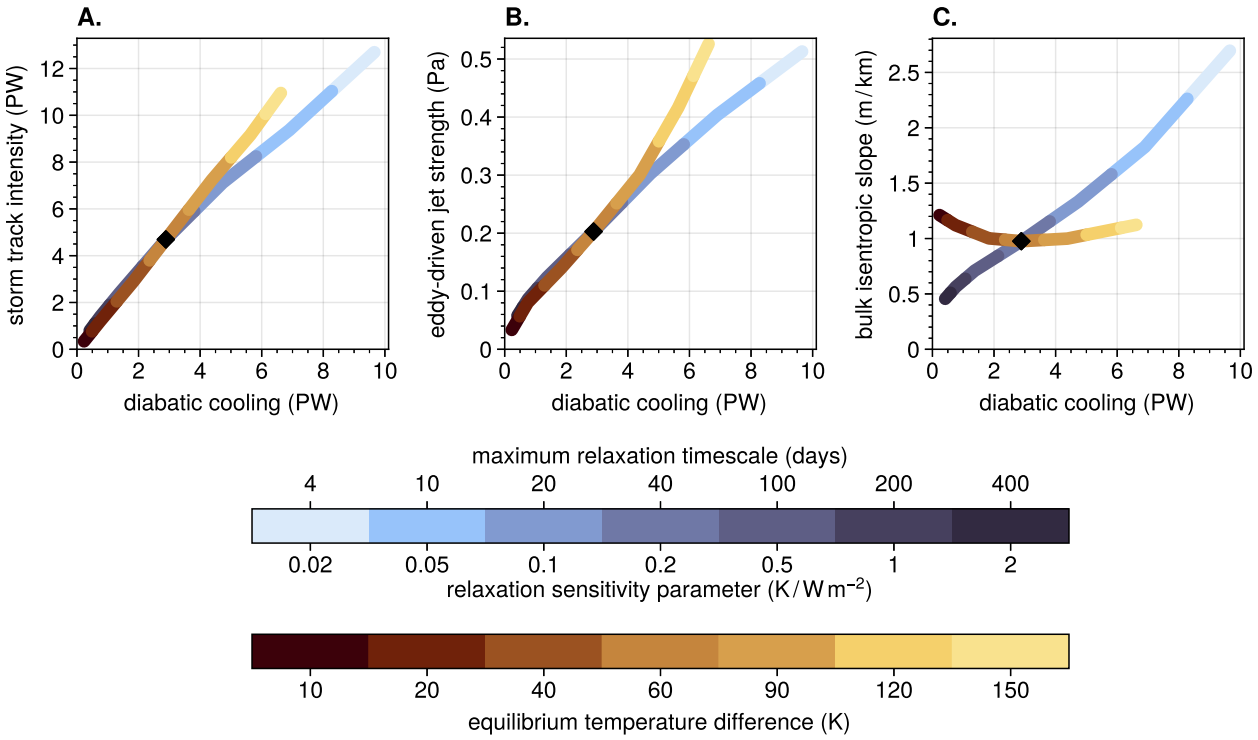

Figure 3.3: Thermodynamic constraints on the extratropical circulation. Each distinct line segment represents the steady-state climatology from a simulation where the relaxation climate sensitivity (i.e., reference thermal relaxation timescale; blue) or surface equator-pole equilibrium temperature difference (orange) was perturbed relative to the *Held and Suarez* (1994) configuration (indicated by the black diamond). The lines can be thought of as parametric functions of the x- and y-axis variables, where the independent variable (the forcing parameter) is indicated by the position along the line. For each panel, the x-axis indicate vertically integrated diabatic cooling, integrated from the storm track to the pole (see Figure 3.2, B). The y-axes indicate the (A) storm track intensity, (B) eddy-driven jet strength, and (C) bulk isentropic slope. Where the y-axis parameter is constrained by the diabatic cooling, the orange and blue lines should coincide. Where the y-axis parameter is constrained by the relaxation climate sensitivity, the orange line should be horizontal. The storm track and eddy-driven jet are defined in Section 3.1, and the bulk isentropic slope is defined as the ratio of the average meridional potential temperature gradient to the average vertical potential temperature gradient, with the averages taken between latitudes 20° and 70° and from the surface to 200 hPa.

ity (*Schneider* 2004, *Schneider and Walker* 2006). The relationship between thermal damping timescales and isentropic slopes was noted by *Zurita-Gotor* (2008), and arises from the fact that the thermal damping timescale regulates the resemblance of the mean climate to a steep-isentrope equilibrium state (where dynamics are too slow to affect the mean temperature; Figure 2.4, A, gray contours) versus a flat-isentrope isothermal state (where dynamics have infinite time to equilibrate the equator with the poles). The isentropic slope relationship may also be connected to the larger storm track-diagnosed thermal diffusivity observed with faster thermal relaxation timescales (Figure 3.2, B; *Zurita-Gotor* 2008). The viability of an emergent constraint based on climatological isentropic slope is unclear, since the bulk of the uncertainty in coupled climate model estimates of climate sensitivity is due to the effects of clouds on radiation (e.g., *Caldwell et al.* 2016, *Dufresne and Bony* 2008, *Vial et al.* 2013). Nevertheless, it would be interesting to test this relationship in the CMIP5 and CMIP6 ensembles.

In sum, Figures 3.1–3.3 demonstrate that relaxation climate sensitivity plays a central role in governing the structure and amplitude of the large-scale circulation. Lower relaxation climate sensitivities (i.e., shorter relaxation timescales) lead to a more vigorous extratropical circulation by strengthening the thermal forcing. The relationship only breaks down for extremely low relaxation climate sensitivities, under which baroclinic eddies are unable to grow. In the following section, I explore the implications of these results for the large-scale circulation response to global warming.

3.2 Perturbed circulation

In addition to the unperturbed simulations, I carried out several perturbed "global warming" simulations using a wide range of relaxation climate sensitivities. This was done by imposing a horizontally uniform heating term analogous to a greenhouse gas radiative forcing perturbation (see Section 2.3 for details). The perturbed simulations provide insight into the role of relaxation climate sensitivity in governing the large-scale circulation response to global warming.

By construction, given the same forcing perturbation H, the dynamical core responds with greater warming for model configurations with higher relaxation climate sensitivity (Figure 3.4,

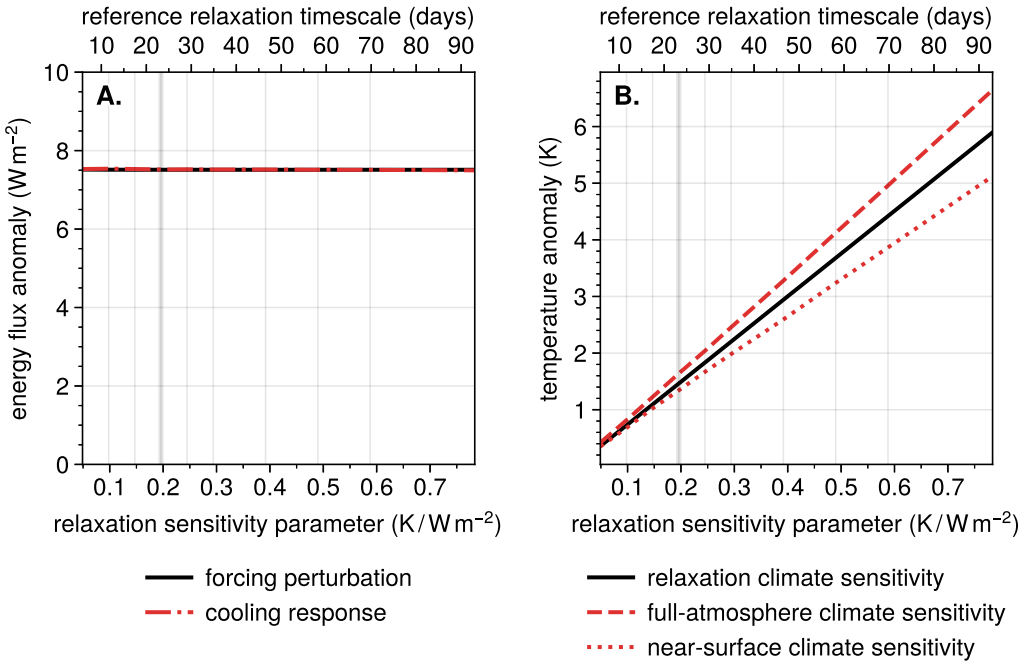

Figure 3.4: Relaxation climate sensitivity and the thermodynamic response to global warming. (A) The global average vertical integral of the imposed forcing perturbation H (solid black; Equation 2.4) and the simulated diabatic cooling response ΔQ (i.e., negative thermal relaxation response; dash-dotted red; Equation 2.2). (B) The prescribed relaxation climate sensitivity ΔT_τ (solid black; Equation A.7) and the simulated temperature response ΔT averaged over the entire atmosphere (dashed red; Equation A.1) and over the near-surface 900 hPa pressure level (dotted red; Equation A.2). Note that the black lines indicate quantities prescribed *a priori* and the red lines indicate quantities diagnosed from simulations. The configurations I explicitly tested are indicated with vertical grid lines, and the *Held and Suarez* (1994) configuration is indicated with the thick vertical grid line.

B; Figure 3.5, A–C, shading). The simulated warming scales almost linearly with respect to the reference sensitivity parameter, whether averaged over the entire atmosphere or a near-surface layer (Figure 3.4, B, red dashed and dotted lines). However, the magnitude of the warming deviates slightly from that predicted by the reference sensitivity parameter (Figure 3.4, B, black solid line). This is due to the non-zero spatial covariance between the temperature response and the relaxation feedback parameter (compare shading and dotted contours, Figure 3.5, A–C), which decreases the full-atmosphere effective feedback parameter $\hat{\lambda}_\tau$ (Equation A.1) and increases the near-surface effective feedback parameter $\hat{\lambda}_{i\tau}$ (Equation A.2). The results described here represent *steady-state* responses, since the diabatic cooling anomalies integrated over the entire atmosphere are equivalent to the imposed forcing perturbation $\overline{\langle\langle H \rangle\rangle}$ (Figure 3.4, A, red and black lines).

The dynamical core model captures the basic qualitative structure of the warming response from more complex general circulation models: There is enhanced warming near the polar surface, analogous to polar amplification (Figure 3.5, A–C, shading; e.g., *Alexeev et al.* 2005, *Crook et al.* 2011, *Holland and Bitz* 2003, *Pithan and Mauritsen* 2014), and enhanced warming in the tropical upper troposphere, analogous to moist adiabatic adjustment (Figure 3.5, A–C, shading; e.g., *Held and Soden* 2000, 2006, *O'Gorman and Muller* 2010). The warming pattern is similar for all simulations, but larger in magnitude for simulations with higher relaxation climate sensitivity. Importantly, when I repeat the unperturbed and perturbed experiments with spatially uniform relaxation feedback parameters (accomplished by setting $\tau_{\min} = \tau_{\max}$; Equations 2.3 and A.10), the warming is virtually horizontally uniform and decays with height according to H (compare Figures 3.5 and 3.6, A–C and Figure 2.4, C).

The qualitative agreement with warming patterns from more complex models may appear surprising given that the dominant physics creating these patterns (i.e., increased latent heat release, moisture transport changes, and ice-albedo feedback) are not represented in the dynamical core model. They come about somewhat fortuitously due to the non-uniform pattern of relaxation feedback parameters (i.e., thermal relaxation timescales; Figure 3.5, A–C, dotted contours). In particular, the enhanced polar lower-tropospheric warming appears to derive from meridional gradients in the relaxation feedback parameter (compare shading and dotted contours, Figure 3.5, A–C), analogous to meridional gradients in the temperature radiative kernel (Figure 2.2, A and D). Similarly, the enhanced tropical upper-tropospheric warming appears to derive from vertical gradients in the relaxation feedback parameter (compare shading and dotted contours, Figure 3.5, A–C), analogous to vertical gradients in the Clausius-Clapeyron-scaled specific humidity radiative kernel (Figure 2.2, B and D).

The warming response to the forcing perturbation H is associated with notable changes in the large-scale circulation. The storm track and the eddy-driven jet both shift poleward, with a generally larger shift for model configurations with higher relaxation climate sensitivity (Figure 3.7, C–D). For every climate sensitivity, the spatial pattern of the zonal wind response is characterized

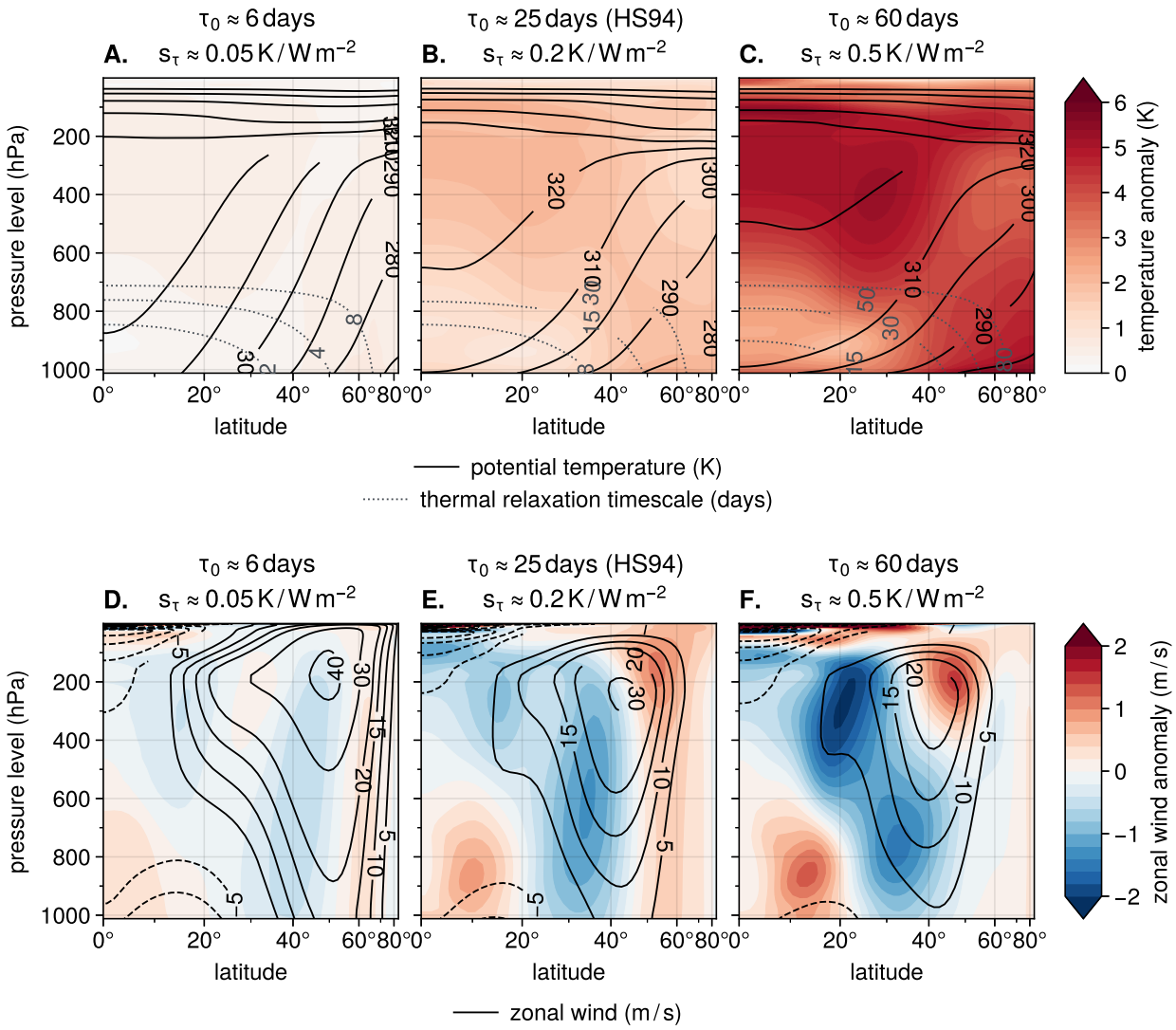

Figure 3.5: Relaxation climate sensitivity and the large-scale circulation response to global warming. Steady-state latitude-height cross-sections from the global warming simulations with relaxation climate sensitivities (A, D) less than, (B, E) equal to, and (C, F) greater than the *Held and Suarez* (1994) relaxation climate sensitivity. The top row (A–C) shows the unperturbed zonal-mean potential temperature (contours) and the temperature response to the forcing perturbation (shading). The thermal relaxation timescales are shown with gray dotted contours. The bottom row (D–F) shows the unperturbed zonal-mean zonal wind (contours) and the zonal wind response to the forcing perturbation (shading). The relaxation sensitivity parameters and associated reference thermal relaxation timescales are indicated above each panel.

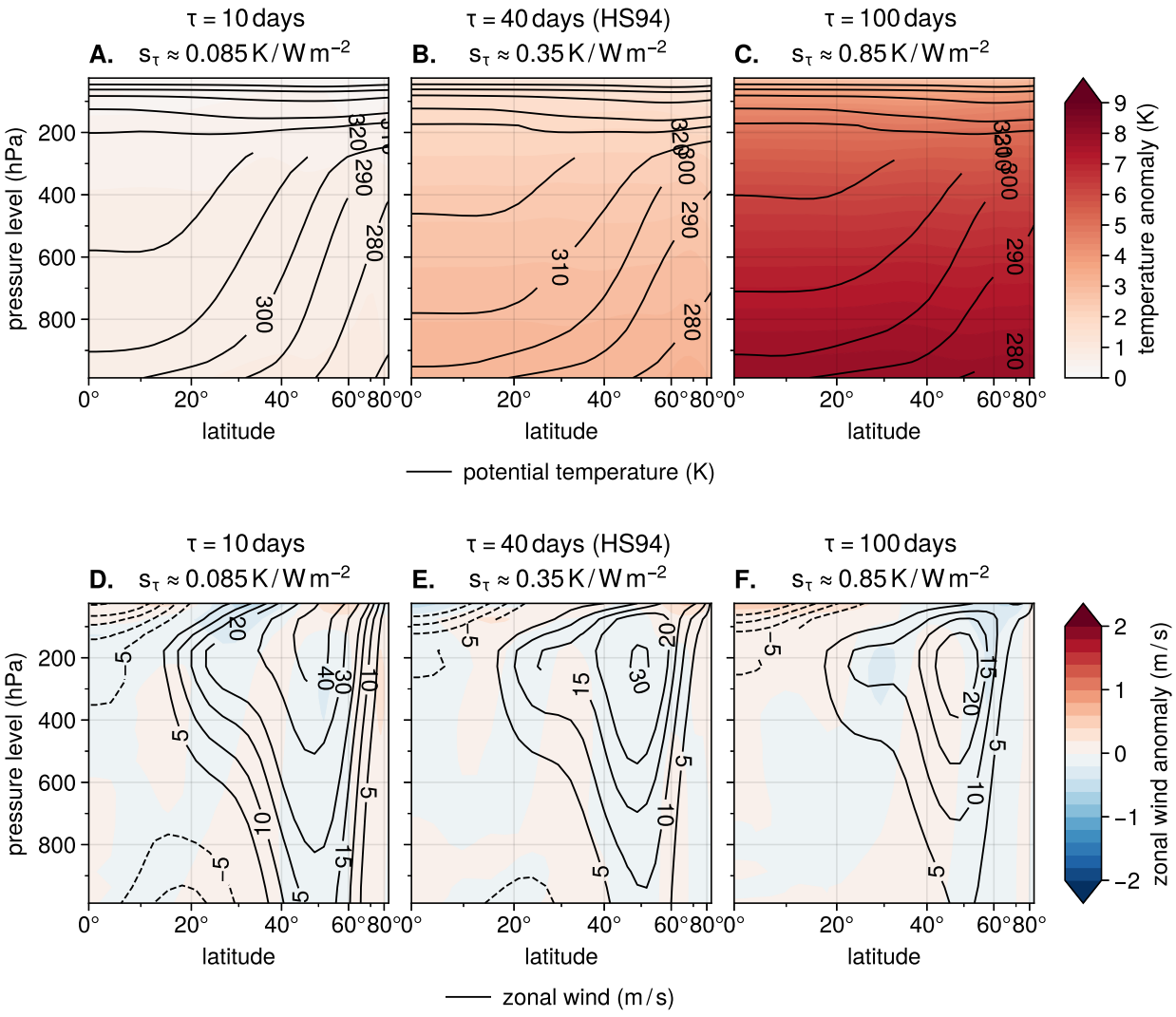

Figure 3.6: As in Figure 3.5, but for the experiments with uniform thermal relaxation timescales.

by a deceleration of the equatorward flank of the eddy-driven jet and a deceleration of the upper-level subtropical jet extension (Figure 3.5, D–F, shading). The responses scale with relaxation climate sensitivity because under a fixed pattern of relaxation feedback parameters, higher relaxation climate sensitivity corresponds to larger horizontal temperature gradient anomalies (Figure 3.5, A–C, shading). In the case of spatially uniform relaxation feedback parameters, where there are no changes to the horizontal temperature gradient (Figure 3.6, A–C, shading), the zonal wind response and poleward storm track and eddy-driven jet shifts entirely disappear (compare Figures 3.5 and 3.6, D–F; Figures 3.7 and 3.8, C–D).

The warming response is also associated with a robust reduction in storm track intensity (Figure 3.7, A–B, red lines). At first glance, the increased temperature gradients in the middle and upper troposphere would seem to imply an increase in storm track intensity (Figure 3.5, A–C, shading). However, since the thermal relaxation coefficients are stronger in the boundary layer, changes to the temperature gradients in the lower troposphere result in comparatively larger changes to the thermal forcing. Thus, the lower tropospheric temperature gradients play an outsize role in determining the total heat transport response. The magnitude of the response is small due to the competing effects of the decreased lower troposphere temperature gradients and increased middle and upper troposphere temperature gradients, again analogous to more complex models (*Shaw et al.* 2016). In the case of spatially uniform relaxation feedback parameters, since there is no meridional contrast in the thermal forcing response, the storm track intensity reduction disappears (compare Figures 3.7 and 3.8, A–B, red lines).

Notably, whereas the zonal wind response and latitude shifts depend on relaxation climate sensitivity, the storm track intensity response does not (Figure 3.7, B, red line). This is due to the fact that 1) the latitude-height thermal relaxation coefficient pattern (i.e., relaxation feedback parameter pattern; Figure 2.2, D) is unchanged between model configurations (Figure 3.5, A–C, dotted contours) and 2) the global average thermal forcing response is necessarily constant (Figure 3.4, A, red line). While the global warming forcing perturbation always increases global temperature and decreases near-surface meridional temperature gradients, the magnitude of the

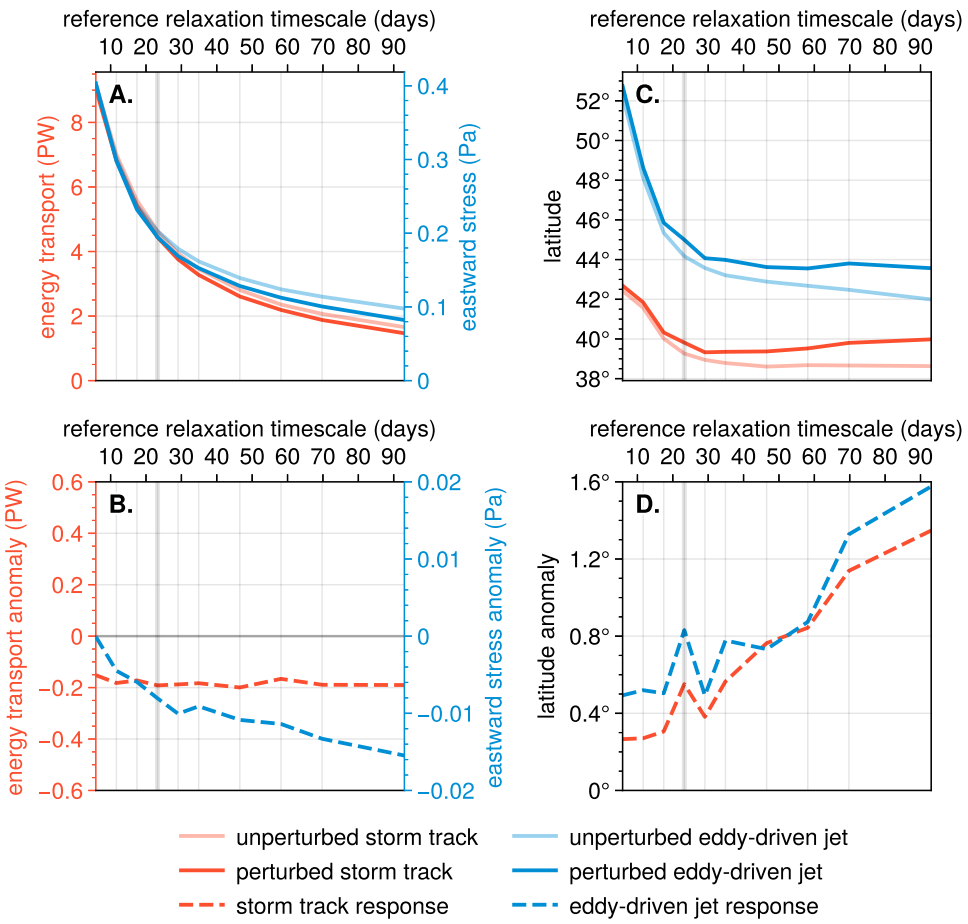

Figure 3.7: Relaxation climate sensitivity and the extratropical circulation response to global warming. Steady-state extratropical circulation responses as a function of the relaxation sensitivity parameter s_τ (bottom x-axis) and the reference thermal relaxation timescale τ_0 (top x-axis). (A) The storm track intensity (solid red) and eddy-driven jet strength (solid blue) for the unperturbed control experiments (faded colors) and the perturbed global warming experiments (saturated colors). (B) The perturbed minus unperturbed storm track intensity (dashed red) and eddy-driven jet strength (dashed blue). (C, D) As in A, B, but for the latitudes and latitude shifts of the storm track (red) and eddy-driven jet (blue). The configurations I explicitly tested are indicated with vertical grid lines, and the *Held and Suarez* (1994) configuration is indicated with the thick vertical grid line. The storm track and eddy-driven jet are defined in Section 3.1.

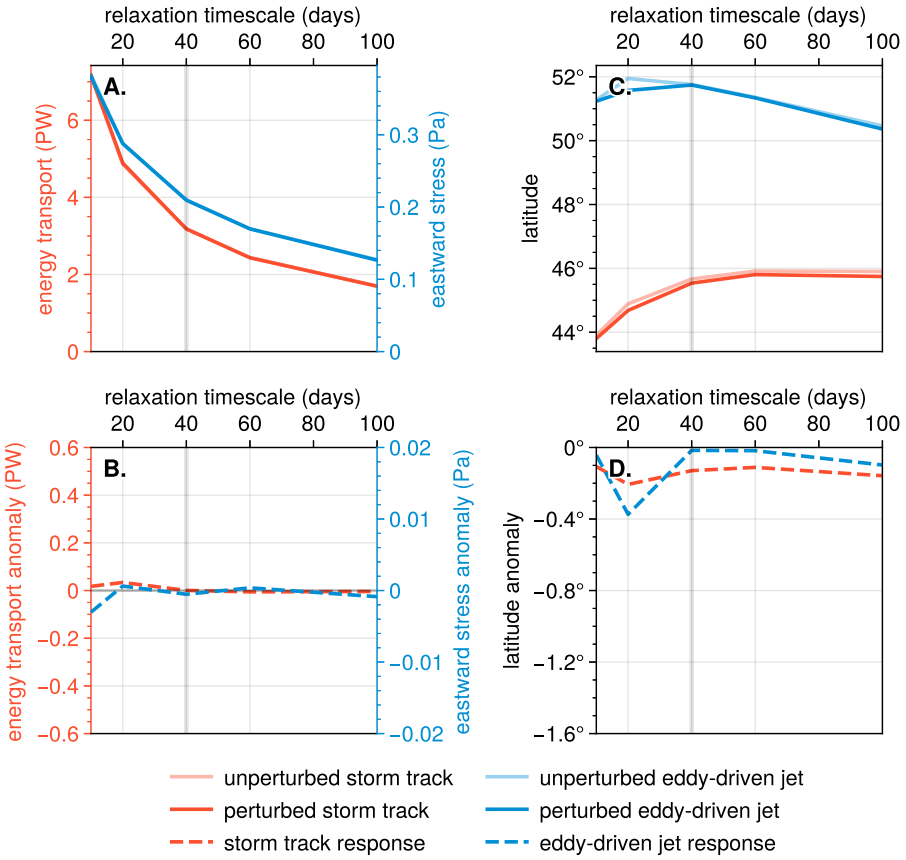

Figure 3.8: As in Figure 3.7, but for the experiments with uniform thermal relaxation timescales.

temperature change is scaled everywhere by the relaxation feedback parameter. Thus, the thermal forcing response associated with the temperature change is roughly constant. Since the storm track intensity is constrained by thermal forcing, the storm track response to the forcing perturbation is necessarily independent of relaxation climate sensitivity and decoupled from the temperature response. This decoupling is consistent with the differing static energy diffusivities of climates with different relaxation climate sensitivities (Figure 3.2, B, solid and dashed medium gray lines).

The forcing perturbation H also leads to a weakening of the eddy-driven jet (Figure 3.7, A–B, blue lines), consistent with the strong coupling between eddy-driven jet strength and storm track intensity (Figure 3.2, C, red and blue lines). However, unlike the storm track response, the eddy-driven jet response is generally larger for configurations with higher relaxation climate sensitivity (Figure 3.7, B). This may come about because the eddy-driven jet strength is not energetically constrained, but rather determined by the structure of eddy momentum fluxes. These momentum fluxes reflect characteristics of wave propagation and dissipation, which itself depends on meridional and vertical temperature gradients. The larger eddy-driven jet response is then consistent with the larger temperature pattern response found under higher relaxation climate sensitivity (Figure 3.5, A–C, shading). Similarly, the absence of an eddy-driven jet response under spatially uniform relaxation feedback parameters (compare Figures 3.7 and 3.8, A–B, blue lines) is consistent with the absence of a temperature pattern response under any corresponding relaxation climate sensitivity (Figure 3.6, A–C, shading).

In sum, Figures 3.4–3.8 highlight the key role of the relaxation climate sensitivity in determining not only the temperature response but also the large-scale circulation response to external forcing perturbations. Under a fixed spatial pattern of relaxation feedback parameters, the warming response pattern is larger for higher relaxation climate sensitivity, resulting in a larger zonal wind response and larger poleward shifts in the storm track and eddy-driven jet. By contrast, the thermal forcing response pattern is mainly independent of relaxation climate sensitivity, resulting in a constant reduction in storm track intensity. Importantly, the circulation response virtually disappears under spatially uniform relaxation feedback parameters. This highlights the critical roles of both

the feedback parameters and the warming response pattern in guiding the circulation response to forcing perturbations.

Chapter 4

Coupled models: Feedbacks

4.1 Context and motivation

Chapters 2 and 3 investigated the relationships between climate feedbacks and the global circulation in an idealized GCM. In the next chapters, I extend this investigation to much more complex, fully-coupled GCMs from the most recent two versions of the Coupled Model Intercomparison Project (CMIP5 and CMIP6; *Eyring et al.* 2016, *Taylor et al.* 2012). Throughout these chapters, I quantify climate feedbacks using the *traditional forcing-feedback framework* rather than the *relaxation forcing-feedback framework* developed in Chapter 2. The differences between these frameworks can be summarized as follows:

- Relaxation climate feedbacks are defined as a function of space and height, reflecting the local sensitivity of diabatic (or "radiative") cooling to air temperature. By construction, they are time-invariant, and they behave identically under both externally imposed forcing perturbations and perturbations generated by internal variability. In this way, relaxation feedbacks have more in common with radiative feedback kernels than climate feedback parameters (Appendix A.2; *Kramer et al.* 2019, *Soden and Held* 2006, *Soden et al.* 2008, *Zelinka et al.* 2012). Feedback kernels are typically used to decompose more complex radiative responses into contributions from individual processes, and are known to be much more robust than the fully-resolved radiative responses themselves (e.g., *Soden et al.* 2008, *Zelinka et al.* 2020).

- Traditional climate feedbacks are defined either globally (*Hansen et al.* 1985, *Roe* 2009, *Rugenstein and Armour* 2021) or as a function of horizontal space (*Andrews et al.* 2015, *Armour et al.* 2012, *Hedemann et al.* 2022). Unlike relaxation feedbacks, they reflect the non-local sensitivity of top-of-atmosphere (TOA) radiation to surface temperature. Thus, rather than arising from local relationships between temperature and energetics, they emerge from a broad spatial distribution of energetic responses and the coupled, possibly non-linear

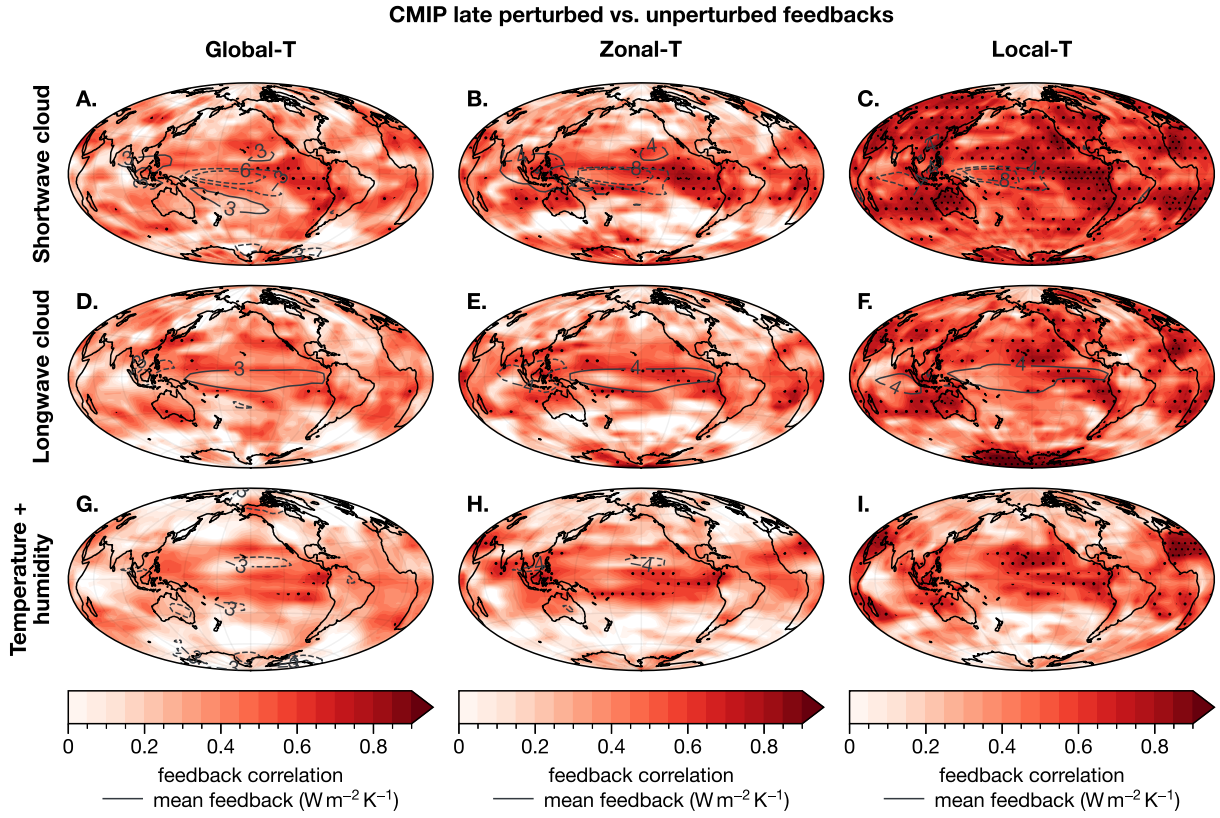

Figure 4.1: Inter-model correlation between local CMIP6 perturbed and unperturbed feedbacks. Shading indicates inter-model correlation coefficients r, while light stippling (heavy stippling) indicates r^2 values above 33% (66%). The first, second, and third columns denote feedbacks calculated with Gregory regressions against global-average surface temperature, zonal-average surface temperature, and local surface temperature (respectively). The first, second, and third rows denote shortwave cloud feedbacks, longwave cloud feedbacks, and combined temperature-humidity feedbacks (respectively). The temperature-humidity feedbacks consist of the sum of the Planck, water vapor, and lapse rate feedbacks.

circulation adjustments controlling their distribution (e.g., *Feldl and Roe* 2013b, *Williams et al.* 2023). As a consequence, traditional climate feedbacks are known to vary substantially as a function of ocean heat uptake patterns (*Liu et al.* 2018a,b, *Rose et al.* 2014, *Rugenstein et al.* 2016a), radiative forcing agents (*Hansen et al.* 1997, *Haugstad et al.* 2017, *Paynter and Frölicher* 2015, *Richardson et al.* 2019), and perturbation response timescales (*Andrews et al.* 2022, *Armour et al.* 2012, *Gregory et al.* 2004, *Held et al.* 2010, *Williams et al.* 2008). This variation is especially pronounced for global feedbacks, but is also present for most simple definitions of the local climate feedback (*Hedemann et al.* 2022).

Given the significant uncertainty of traditional feedback definitions, any relationships between climate feedbacks and the large-scale circulation inferred from coupled models will be harder to interpret. The rest of this thesis therefore focuses on the feedback definitions themselves, leaving further investigations of feedback-circulation relationships to future work. In particular, I examine differences between local and global estimates of traditional climate feedbacks across both unperturbed experiments (guided by coupled atmosphere-ocean internal variability alone) and perturbed experiments (driven by an abrupt quadrupling of CO_2 concentrations). Thus unlike Chapter 3, which used an explicit parameter to change the climate feedback, this section leverages inter-model spread across ensembles of CMIP5 and CMIP6 experiments as an effective, *emergent* scaling of the simulated climate feedback. I then investigate the mechanisms behind these emergent relationships and their differences across each CMIP generation.

Previous research with CMIP ensembles has typically found relatively weak relationships between internal, unperturbed climate feedbacks and perturbed climate feedbacks (*Lutsko* 2018, *Lutsko and Takahashi* 2018). However, the idealized model results from Chapter 3 pointed to the robustness of local relaxation climate feedbacks over global climate feedbacks diagnosed from model experiments (Figure 3.4; Equations A.1 and A.2). Thus, an initial hypothesis informed by the dynamical core experiments is that inter-model spread in *local* unperturbed climate feedbacks might tell us more about *local* perturbed climate feedbacks than global versus global inter-model relationships. Figure 4.1 tests part of this hypothesis by showing inter-model correlation coefficients between local unperturbed and perturbed climate feedbacks, using local feedbacks defined with either local surface temperature (first column), zonal-average surface temperature (second column), or global-average surface temperature (third column; *Feldl and Roe* 2013a, *Hedemann et al.* 2022). The feedbacks were estimated using Gregory regressions of both unperturbed global temperature variability and perturbed responses to abrupt CO_2 quadrupling (*Gregory et al.* 2004), then decomposed into contributions from cloud and non-cloud changes using radiative kernels (*Soden and Held*, 2006; *Soden et al.*, 2008; see Appendix B.1 for details).

The results show relatively strong relationships between local unperturbed climate feedbacks and local perturbed climate feedbacks – especially over the East Pacific (Figure 4.1; A–C). The inter-model relationships are also stronger for feedbacks defined with local surface temperature (Figure 4.1; right column) compared to feedbacks defined with global surface temperature (Figure 4.1; left column). This is surprising, given that local surface temperature feedbacks have been shown to be less robust than global surface temperature feedbacks over the time-evolving response to abrupt CO_2 quadrupling (*Hedemann et al.* 2022). Nevertheless, in each case, only a few regions exhibit local unperturbed-perturbed feedback correlations that are as strong as the correlations between global average unperturbed climate feedbacks and global average perturbed climate feedbacks (see following section, Figure 4.3, annotations). Thus, despite the mixed results of past research, constraints based on global or regional climate feedbacks may be more promising candidates for inferring the global climate response from internal climate variability.

4.2 Cloud feedback constraints

Figure 4.2 shows distributions of early perturbed, late perturbed, and unperturbed climate feedbacks from each CMIP generation. The feedbacks and their cloud and non-cloud components were estimated as in Figure 4.1 (see above). The results are also averaged across unique institutes before computing inter-model statistics to help reduce double counting biases (*Abramowitz et al.* (2018), *Leduc et al.* (2016); see Appendix B.2 for details). Note that the distributions in Figure 4.2 are similar when using individual models instead of institute-averages (Figure B.4). In CMIP5, net unperturbed climate feedbacks are typically more positive than both the early and late perturbed feedbacks (compare pale gray to blue and red, far left, Figure 4.2). The CMIP5 perturbed feedbacks are also spread more narrowly and less evenly than the unperturbed feedbacks. Notably, the late perturbed feedback values are closer to the unperturbed feedbacks than the early perturbed feedbacks (compare gray to red, far left, Figure 4.2). In CMIP6, the net unperturbed feedbacks are slightly more negative (compare pale and dark colors, far left, Figure 4.2), while both the early and late perturbed feedbacks are more positive (consistent with *Zelinka et al.* 2020). Further, inter-

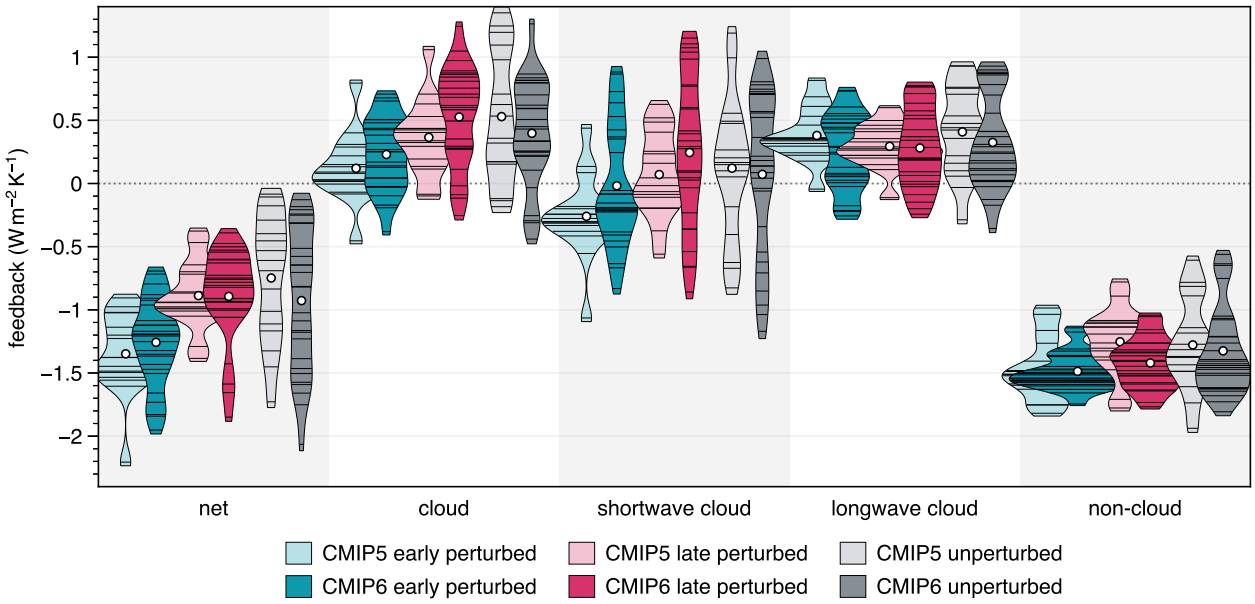

Figure 4.2: Multi-model distributions of perturbed and unperturbed climate feedback parameters. "Violin" shapes indicate Gaussian kernel density fits to the institute-averaged feedback distributions using a bandwidth of 0.3 W m^{-2} K^{-1}. For each violin, horizontal lines indicate the institute-averages comprising the distribution and white markers indicate the average of the lines. The violin widths are scaled such that the shapes have approximately equivalent areas. Each background shading zone corresponds to the feedback component indicated on the x axis. Blue, red, and gray indicate the early perturbed period (years 0–20), late perturbed period (years 20–150), and unperturbed period, respectively. Pale and dark colors indicate the CMIP5 and CMIP6 ensembles, respectively.

model spread in the early and late perturbed feedbacks is significantly higher, while unperturbed feedback spread is similar to CMIP5. This results in unperturbed and perturbed feedbacks spanning similar values in CMIP6 (dark colors, far left, Figure 4.2). Notably, differences between early and late perturbed feedbacks also appear unchanged in CMIP6 (consistent with *Dong et al.* 2020).

Across both CMIP5 and CMIP6, shortwave cloud radiative effects largely drive the differences between unperturbed and perturbed climate feedbacks (white markers, far left to center-right, Figure 4.2). Clouds also drive inter-model spread in the net feedback, with even larger shortwave cloud spread partly compensated by longwave cloud spread (shapes, far left to center-right, Figure 4.2). While the CMIP6 unperturbed feedbacks are very similar to CMIP5 (gray, center-left to far right, Figure 4.2), the CMIP6 perturbed feedbacks are characterized by much less non-cloud spread and much greater cloud, shortwave cloud, and longwave cloud spread (blue and red, center-left to far right, Figure 4.2). As a result, for CMIP6, inter-model spread in perturbed and unperturbed cloud feedbacks is comparable; both the early and late perturbed shortwave and longwave cloud feedbacks occupy ranges similar to their unperturbed counterparts (dark colors, center-left to center-right, Figure 4.2). This contrasts sharply with CMIP5, in which perturbed cloud feedbacks are much more clustered together than unperturbed feedbacks (light colors, center-left to center-right, Figure 4.2).

The increased perturbed feedback spread in CMIP6 is accompanied by significant changes to inter-model relationships between unperturbed and perturbed feedbacks. I assess these relationships by linearly regressing perturbed feedbacks against unperturbed feedbacks across each CMIP generation. These coefficient represent unperturbed *constraints* on the response to increasing CO_2. Figure 4.3 summarizes the constraints for each CMIP generation and perturbation response time. Individual bars indicate regression coefficients β of early and late perturbed climate feedbacks (blue and red, Figure 4.2) against unperturbed climate feedbacks (gray, Figure 4.2); thin (thick) whiskers indicate 95% (50%) uncertainty ranges for the regression coefficients; and annotations indicate the percent variance explained for each regression (i.e., the squared correlation coefficient r^2). As with Figure 4.1, the results are based on institute-averages rather than individual models;

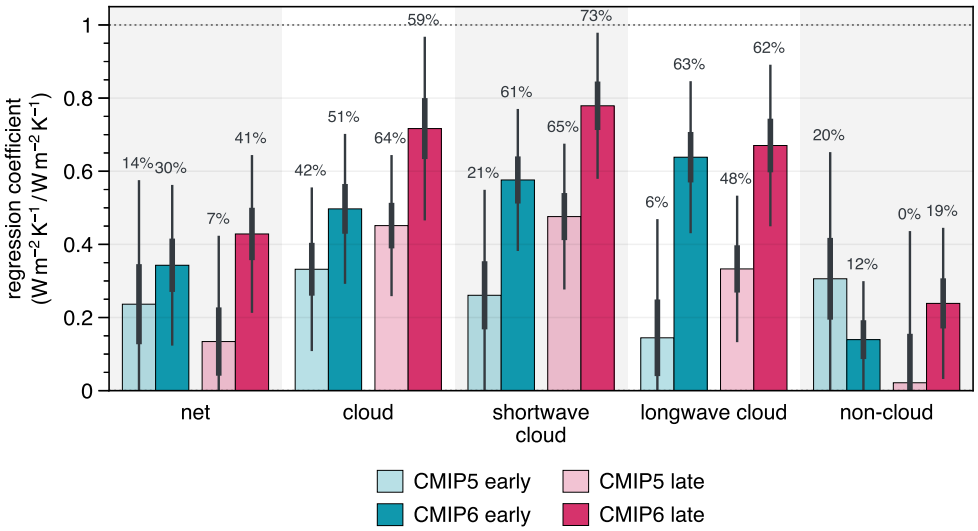

Figure 4.3: Inter-model regressions of perturbed climate feedback parameters against unperturbed feedback parameters. Bars indicate the linear regression coefficients in units $\mathrm{W\,m^{-2}\,K^{-1}}$ / $\mathrm{W\,m^{-2}\,K^{-1}}$. Thin whiskers (thick whiskers) indicate the 95% (50%) uncertainty intervals for the regression coefficients according to two-sided student's t tests. Annotations indicate the percent variance explained (i.e., squared correlation coefficient r^2) for each regression model. Each background shading zone corresponds to the feedback component indicated on the x axis. Blue and red indicate regressions coefficients for the early perturbed feedbacks (years 0–20) and late perturbed feedbacks (years 20–150), respectively. Pale and dark colors indicate regressions across the CMIP5 and CMIP6 ensembles, respectively.

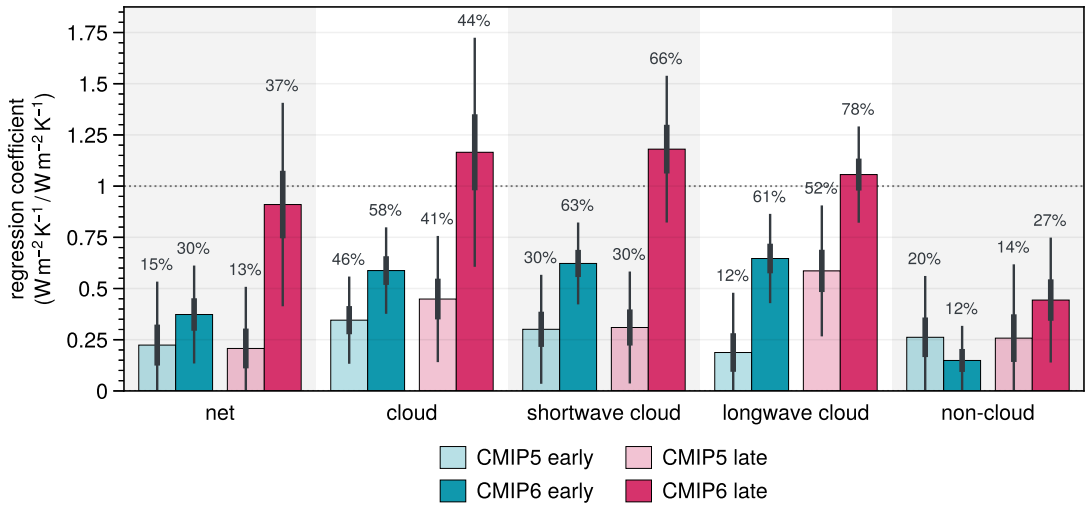

Figure 4.4: As in Figure 4.3 but with the early perturbed feedbacks calculated for years 0–50 and late perturbed feedbacks calculated for years 100–150.

the main effect of institute-averaging is to increase the uncertainty range (Figure B.5). For CMIP5, the constraints on perturbed climate feedbacks are statistically indistinguishable from zero at the 95% confidence level (pale colors, far left, Figure 4.3). For CMIP6, the regression coefficients are statistically significant, with unperturbed feedbacks explaining $\sim$40% of inter-model spread in late perturbed feedbacks (dark colors, far left, Figure 4.3). The higher regression coefficients in CMIP6 are due to both an increased correlation r between unperturbed and perturbed feedbacks (r^2 annotations, far left, Figure 4.3) and greater perturbed feedback spread σ_1 (blue and red, Figure 4.2). Surprisingly, the CMIP6 constraints are more effective for late perturbed feedbacks than early perturbed feedbacks – that is, the far-future radiative response to increasing CO_2 is more predictable from internal variability than the near-future response.

For both CMIP5 and CMIP6, the perturbed climate feedback relationships are largely due to the cloud component (compare center-left and far right, Figure 4.3). Unperturbed cloud feedbacks explain $\sim$50% of inter-model spread in perturbed cloud feedbacks across CMIP5 and CMIP6, while non-cloud feedbacks explain very little inter-model spread (consistent with *He et al.* 2021). Notably, the CMIP6 cloud constraints are stronger when considering the shortwave and longwave components separately, while the CMIP5 cloud constraints are weaker (center-left to center-right, Figure 4.3). As with the net constraints, the regression coefficients for the perturbed cloud feedbacks are higher in CMIP6 than CMIP5. For the total cloud feedback, this is mainly due to greater inter-model spread σ_1 in CMIP6 (blue and red, Figure 4.2); for the shortwave and longwave components, this is due to both greater inter-model spread σ_1 and stronger inter-model correlation r (annotations, Figure 4.3). Similarly, the late perturbed cloud feedbacks are more closely related to internal variability than the early perturbed feedbacks. For both CMIP5 and CMIP6, this is due to both greater inter-model spread σ_1 in late perturbed feedbacks (blue and red, Figure 4.2) and stronger correlations r between late feedbacks and unperturbed feedbacks (annotations, Figure 4.3). The difference between the early and late relationships also holds for an alternative early-late partitioning that uses an equal number of years in each period (years 0–50 for "early",

100–150 for "late"; Figure 4.4). Thus, the weak constraints on the early response are not simply due to internal variability rendering the shorter early period more uncertain.

Any investigation of similarities between unperturbed and perturbed climate feedbacks can be used to build *emergent constraints* on the perturbed climate feedbacks (*Caldwell et al.* 2018, *Hall and Qu* 2006, *Hall et al.* 2019, *Qu et al.* 2018, *Williamson et al.* 2021). This is typically done by identifying "emergent" inter-model relationships between simulated future climate feedbacks and aspects of historical warming or variability, then identifying the most plausible model-simulated futures as those whose pasts agree with observations. In the absence of ensemble convergence onto one solution for the future climate, emergent constraints thus seek to leverage inter-model spread itself into reduced climate feedback uncertainty. Here, we can build emergent constraints on the perturbed cloud feedback by combining inter-model regression coefficients from Figure 4.3 with observational estimates of the unperturbed cloud feedback as follows (e.g., *He et al.* 2021, *Lutsko et al.* 2021, *Uribe et al.* 2022):

$$\hat{\lambda}_1 = \overline{\lambda_1} + \beta(\lambda_0^* - \overline{\lambda_0}) \tag{4.1}$$

Above, λ_0 is the model-simulated unperturbed climate feedback, λ_0^* is the observational estimate of the unperturbed climate feedback, λ_1 is the model-simulated perturbed climate feedback, $\hat{\lambda}_1$ is the observationally-constrained perturbed climate feedback, $\beta \equiv \sum \lambda_1' \lambda_0' / \sum {\lambda_0'}^2$ is the inter-model regression coefficient between unperturbed and perturbed feedbacks, and the overbars and primes indicate multi-model averages and deviations thereof (respectively). The regression coefficients can also be expressed as the product of an inter-model correlation coefficient r and standard deviation ratio σ_1/σ_0 (i.e., $\beta \equiv r\sigma_1/\sigma_0$), where $r \equiv \sum \lambda_1' \lambda_0' / \sigma_1 \sigma_0$ and $\sigma_n \equiv \sqrt{\sum {\lambda_n'}^2}$. Thus, through slight increases in $\overline{\lambda_1}$, slight decreases in $\overline{\lambda_0}$, significant increases in σ_1, and negligible changes in σ_0, the CMIP6 feedback distributions alone (Figure 4.2) promote higher inter-model regression coefficients (Figure 4.3) and more positive observational constraints.

Figure 4.5 evaluates Equation 4.1 using a recent observational estimate of the unperturbed cloud feedback λ_{obs} (*He et al.* 2021). As expected, CMIP6 produces much higher observationally-constrained estimates of the perturbation response than CMIP5. The CMIP6 ensemble produces

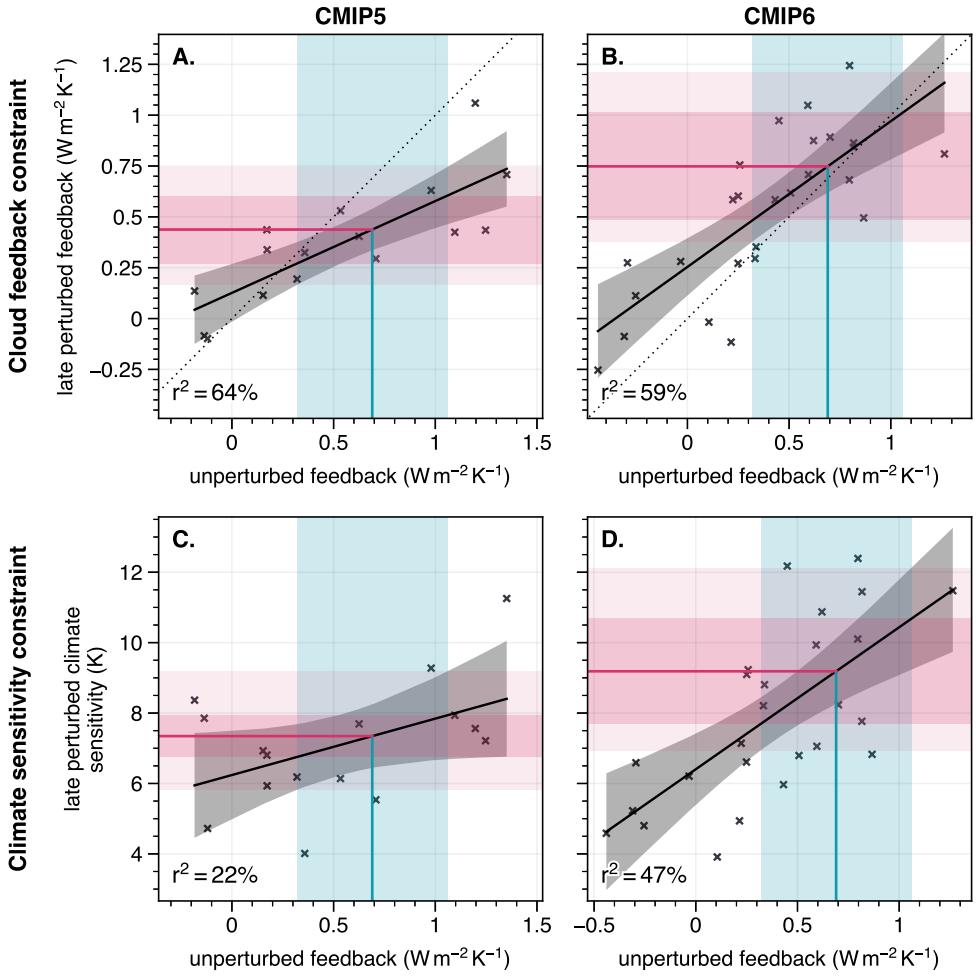

Figure 4.5: Emergent constraints on the perturbation response from observed unperturbed cloud feedbacks. For each panel, the x axes indicate unperturbed cloud feedbacks and the y axes indicate either late perturbed cloud feedbacks (A, B; first row) or late effective climate sensitivity – i.e., the x-intercept of the Gregory regression for the net radiative response to CO_2 quadrupling (C, D; second row). The left and right columns indicate the CMIP5 and CMIP6 ensembles, respectively. Individual markers indicate institute-average results from either ensemble. The black lines indicate linear least-squares regressions, with shading indicating 95% uncertainty bounds according to a Student's t-distribution (assuming the regression residuals are normally distributed). The blue line and shading indicate the mean and 95% uncertainty bounds for the observational unperturbed cloud feedback estimate from *He et al.* (2021). The pink line and shading indicate the mean constrained estimate and 95% uncertainty bounds for the perturbation response variable, taking into account just observational uncertainty (darker pink shading) or both observational and regression slope uncertainty (lighter pink shading). The *He et al.* (2021) observational cloud feedback estimate was evaluated over 2001–2019 using the NASA GISTEMP4 surface temperature dataset (*Lenssen et al.* 2019), the CERES EBAF4.1 satellite estimates of all-sky and clear-sky radiation, (*Loeb et al.* 2018), and cloud masking adjustments calculated from 1) a set of radiative feedback kernels derived from CERES observations (*Kramer et al.* 2019) and 2) time series of tropospheric air temperature and specific humidity estimated by the ERA5 reanalysis

constrains the early and late cloud perturbed feedbacks to 0.39 $\mathrm{W\,m^{-2}\,K^{-1}}$ (95% CI: 0.12–0.74) and 0.75 $\mathrm{W\,m^{-2}\,K^{-1}}$ (95% CI 0.38–1.19; Figure 4.5, A, red), respectively, while the CMIP5 ensemble constrains them to only 0.17 $\mathrm{W\,m^{-2}\,K^{-1}}$ (95% CI: -0.09–$+0.45$) and 0.44 $\mathrm{W\,m^{-2}\,K^{-1}}$ (95% CI: 0.17–0.75; Figure 4.5, B, red). Notably, despite the reduced sample size arising from our use of institute-averages rather than individual models, these constraints are less uncertain than the constraints from *He et al.* (2021). This may be due to our use of 18 additional CMIP6 models or our use of reanalysis-based radiative kernels (*Huang et al.* 2017) rather than satellite-based radiative kernels (*Kramer et al.* 2019) for the cloud masking adjustments. Overall, however, unperturbed cloud feedbacks in CMIP6 suggest that moderately to highly positive late cloud feedbacks are more likely than weakly positive or negative cloud feedbacks, with a constrained 95% uncertainty range ($0.81\,\mathrm{W\,m^{-2}\,K^{-1}}$) that is significantly narrower than the original, unconstrained uncertainty range ($1.28\,\mathrm{W\,m^{-2}\,K^{-1}}$). In the following chapter, I use regional decompositions to investigate the role of warming patterns and circulation adjustments on the constraint differences across both CMIP generations and perturbation response times.

Chapter 5

Coupled models: Patterns

5.1 Context and motivation

Emergent constraints targeting different processes can lead to divergent conclusions on the physical plausibility of particular feedback values. Several studies have pointed to strong relationships between model simulations of anthropogenically forced future warming and historical warming (*Cox et al.* 2018, *Nijsse et al.* 2020, *Tokarska et al.* 2020b). These studies typically find that 1) near-term warming is more effectively constrained than long-term warming, and 2) since observed historical warming is on the lower end of model simulations, models with less warming and more negative feedbacks are more consistent with observations. However, other studies have pointed to the importance of pattern effects on the evolution of historical and future climate feedbacks (*Andrews et al.* 2015, 2018, 2022, *Armour et al.* 2012, *Gregory and Andrews* 2016, *Senior and Mitchell* 2000, *Stevens et al.* 2016, *Zhou et al.* 2016). These studies suggest that the relative inability of coupled models to simulate historical warming patterns may render emergent constraints based on historical warming untrustworthy (*Andrews et al.* 2022, *Dong et al.* 2021, *Heede et al.* 2020, *Marvel et al.* 2018). Adjustments to these constraints based on model-simulated regional warming and feedback patterns produce much higher observationally-constrained climate feedback estimates (*Andrews et al.* 2018, *Armour* 2017, *Watanabe et al.* 2021). Similarly, constraints based on cloud feedback mechanisms rather than historical warming or surface temperature often produce higher climate feedback estimates (*Bretherton and Caldwell* 2020, *Brient* 2020, *Kamae et al.* 2016, *Klein and Hall* 2015, *Lutsko et al.* 2021).

This chapter aims to bridge these two perspectives by considering how pattern effects influence the inter-model cloud feedback relationships described in Chapter 4. First, I hypothesize a fluctuation-dissipation relation (FDR) explanation for the inter-model relationships, with the strength of each constraint controlled by the projection of the response onto the El Niño-Southern

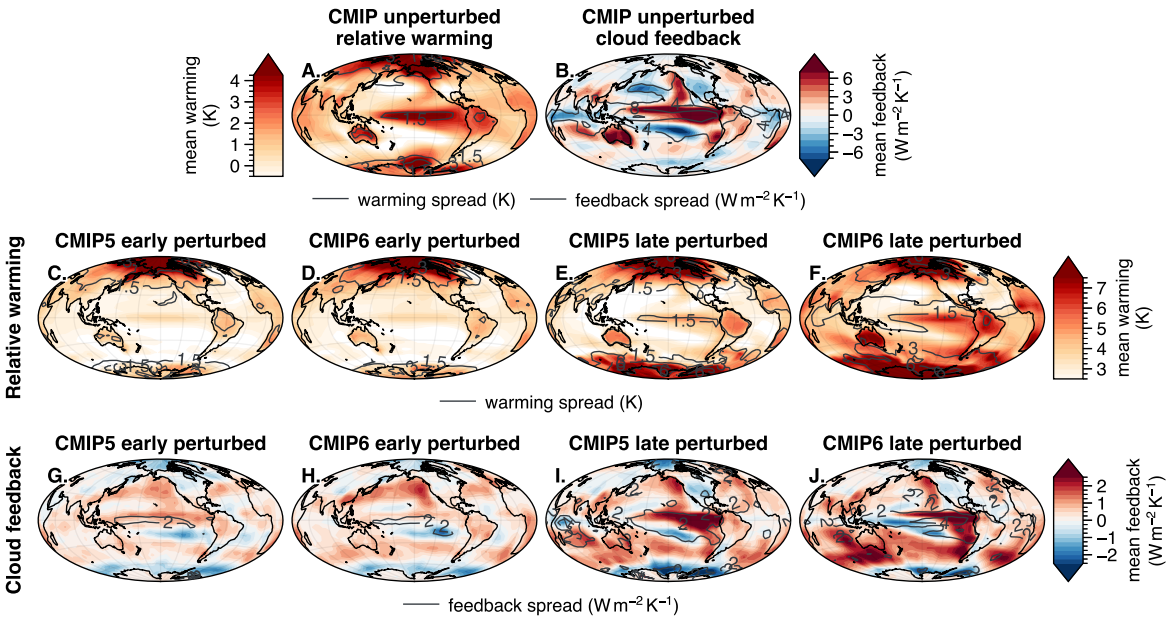

Figure 5.1: Local contributions to global warming and climate feedbacks. The first row indicates average unperturbed warming patterns (A) and cloud feedback patterns (B) across CMIP5 and CMIP6 models (see text for details). The second and third rows indicate perturbed warming patterns (C–F) and cloud feedback patterns (G–J) for the CMIP generation and perturbation response time indicated along columns. Shading indicates multi-model averages and contours indicate inter-model standard deviations.

Oscillation (ENSO). I test this hypothesis by decomposing ensemble average feedbacks and inter-model constraints into regional contributions (*Caldwell et al.* 2018). The results are consistent with other recent work demonstrating the dominance of ENSO-frequency variability on relationships between internal variability and perturbed cloud feedbacks (*Lutsko* 2018, *Lutsko and Takahashi* 2018, *Lutsko et al.* 2021). I then discuss the critical role of pattern effects on both 1) the time evolution of the ensemble average response to forcings (*Andrews et al.* 2022, *Armour et al.* 2012) and 2) the strength and physical interpretation of constraints on ensemble spread. I conclude by considering implications and recommendations for further research.

5.2 Multi-model average patterns

The above relationships between perturbed and unperturbed climate feedbacks can be understood in terms of contributions from different regions. To quantify these contributions, I decompose global-average temperature anomalies and global climate feedback parameters into spatial

warming patterns σ_{T_i} and feedback patterns λ_i for each of the unperturbed, early perturbed, and late perturbed periods (*Andrews et al.* 2015, *Armour et al.* 2012). The feedback patterns indicate the local changes in radiative flux that contribute to the global climate feedback, while the warming patterns provide a qualitative interpretation of the local temperature changes that both drive and respond to the global climate feedbacks. I define each warming pattern σ_{T_i} as a projection of temperature anomalies T_i' at each grid point i onto global-average temperature anomalies T', i.e. $\sigma_{T_i} = \sum_t T_i' T' / \sqrt{\sum_t T'^2}$. This is similar to the common "relative" warming Gregory regression metric $\sum_t T_i' T' / \sum_t T'^2$ (*Andrews et al.* 2015, *Armour et al.* 2012), except the units are K instead of K/K due to a scaling by the global average temperature standard deviation $\sigma_T \equiv \sqrt{\sum_t T'^2}$. The warming patterns σ_{T_i} thereby indicate the absolute warming associated with characteristic changes in global average temperature due to internal variability or increasing CO_2. Note the global average of each warming pattern $[\sigma_{T_i}] = \sigma_T$ is equivalent to the standard deviation of the global average temperature. Similarly, I define each feedback pattern λ_i as the Gregory regression of model-simulated or kernel-derived radiative flux anomalies R_i' at each grid point i against global average temperature anomalies T', i.e. $\lambda_i = \sum_t R_i' T' / \sum_t T'^2$ (*Andrews et al.* 2015, *Hedemann et al.* 2022). Note that global averages of each feedback pattern $[\lambda_i] = \lambda$ are equivalent to the global climate feedback parameters from Figure 4.2. I interpret changes to the climate feedback constraints across CMIP generations and perturbation response times in terms of 1) differences in the multi-model average warming and feedback patterns (this section), and 2) changing pattern contributions to global-average inter-model feedback spread (next section).

Figure 5.1 summarizes the multi-model average patterns (shading) and inter-model pattern spread (contours) for both perturbed and unperturbed climate feedbacks. Across both CMIP5 and CMIP6, unperturbed global-average temperature anomalies are associated with strongly enhanced East Pacific warming and weaker subtropical and West Pacific warming (Figure 5.1, A). This is due to the El Niño-Southern Oscillation (ENSO) producing warm anomalies in global-average temperature by suppressing cold water upwelling in the eastern tropical Pacific (*Halpert and Ropelewski* 1992, *McLean et al.* 2009, *Seager et al.* 2003, *Trenberth et al.* 2002, 2010). The unperturbed cli-

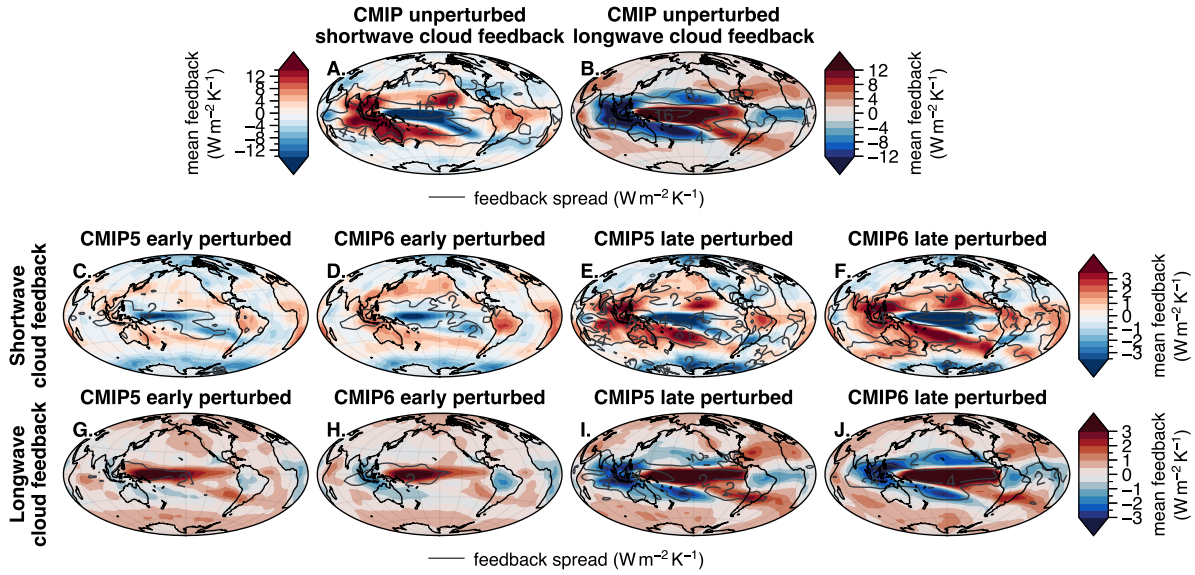

Figure 5.2: As in Figure 5.1 but for the unperturbed and perturbed shortwave and longwave cloud feedbacks. Panel A and the first row indicate regression coefficients for the shortwave component of the cloud feedback. Panel B and the second row indicate regression coefficients for the longwave component of the cloud feedback.

mate feedbacks thus reflect the circulation changes associated with an average El Niño event – that is, an eastward and southward shift in Pacific convection, a reversal of the zonal Walker circulation, and a destabilization of the boundary layer under descending branches of the Walker cells (*Alexander et al.* 2002, *Bjerknes* 1966, 1969, *Di Lorenzo et al.* 2015, *Rasmusson and Carpenter* 1982, *Schneider et al.* 2014, *Seager et al.* 2003). These changes manifest as positive cloud feedbacks over both 1) the central and eastern tropical Pacific, where shallow clouds are replaced by convective towers that reduce outgoing longwave radiation (Figure 5.1, B; Figure 5.2, A–B), and 2) the eastern subtropical Pacific and Indian oceans, where the weakened boundary layer inversion dissipates trade and stratocumulus clouds, thereby increasing shortwave absorption (*Bellomo et al.* 2014, *Klein and Hartmann* 1993, *Middlemas et al.* 2019, *Myers and Norris* 2015, *Park and Leovy* 2004, *Rädel et al.* 2016, *Scott et al.* 2020, *Zhu et al.* 2007). There are also slightly negative unperturbed cloud feedbacks over the south and north central Pacific, likely due to increased shallow clouds and large-scale descent in these regions. The positive and negative unperturbed feedback

regions are asymmetric, resulting in a net positive global unperturbed cloud feedback (Figure 4.2, gray).

The early perturbed warming pattern bears little resemblance to the unperturbed variability (Figure 5.1, C, D), with weak warming over the oceans, moderate warming over land, and polar amplification mostly confined to the northern hemisphere. There is only moderately enhanced warming over the central tropical Pacific, indicative of the nascent (but not fully realized) El Niño-like response. By contrast, the late perturbed warming patterns strongly resemble unperturbed variability (Figure 5.1, E, F), with amplified warming in the eastern Pacific, suppressed warming in the central and western extratropical Pacific, and polar amplification in both hemispheres. The regional variations are also very similar in magnitude, despite the much smaller magnitude of global average temperature changes under unperturbed variability (compare colorbars; Figure 5.1, A, E, F). The cloud feedback patterns reflect these warming pattern differences; the early response exhibits weakly positive cloud feedbacks over the central tropics (Figure 5.1, G, H), while the late response exhibits strong patterns of negative and positive cloud feedbacks over the same parts of the tropics and subtropics as the unperturbed patterns (compare panel B to panels I and J, Figure 5.1). The shortwave and longwave cloud feedback patterns show that this reflects weak increases in convective clouds over the central Pacific during the early response (Figure 5.2; C, D, G, H), with stronger, more El Niño-like increases over the central and eastern Pacific during the late response (Figure 5.2; E, F, I, J). The late response also exhibits positive cloud feedbacks over the Southern Ocean and North Pacific not present during unperturbed variability (Figure 5.1, I, J). Consistent with Figure 4.2, inter-model spread in the late perturbed patterns also resembles spread in the unperturbed patterns better than the early perturbed patterns (gray contours, Figure 5.1), with the greatest inter-model spread found over the central and eastern tropical Pacific (gray contours; Figure 5.1, A–B, E–F, I–J).

Differences between the average CMIP5 and CMIP6 patterns are more subtle. The early warming patterns are nearly identical between CMIP5 and CMIP6, (Figure 5.1, C and D), while the late CMIP6 response exhibits notably more warming in the eastern tropical and southeastern Pacific

(Figure 5.1, E and F). The tropical and subtropical cloud feedbacks also project slightly more strongly onto the unperturbed feedbacks in CMIP6, with more negative feedbacks in the central subtropical Pacific and more positive feedbacks in the eastern Pacific (Figure 5.1, H and J). The differences are clearer for the shortwave and longwave components, where CMIP6 exhibits an amplified El Niño-like tropical feedback pattern in both the early and late response (Figure 5.2; D, F, H, J). CMIP6 also exhibits more inter-model spread in tropical warming and tropical cloud feedbacks than CMIP5 (contours; Figure 5.1, D, F, H, J). However, the most notable differences between CMIP5 and CMIP6 are found in the extratropics rather than the tropics. In the early response, CMIP6 exhibits more positive cloud feedbacks over the North Pacific and Southern Ocean; in the late response, CMIP6 exhibits even more positive cloud feedbacks over just the Southern Ocean (Figure 5.1, H and J). This has been attributed to reduced brightening from cloud phase transitions and greater cloud cover reductions over extratropical oceans (*Zelinka et al.* 2020).

5.3 Inter-model pattern contributions

I next provide a more quantitative interpretation of pattern effects on the relationships between perturbed and unperturbed feedbacks. Where Figure 5.1 showed ensemble average warming and cloud feedback patterns, Figure 5.3 shows pattern contributions to inter-model relationships between unperturbed and perturbed global warming and cloud feedbacks. I define each warming contribution α_i shown in Figure 5.3 (panels A, C–F) as an inter-model regression of a warming pattern σ_{T_i} against the unperturbed standard deviation in global average temperature $\sigma_{T,0}$, i.e. $\alpha_i \equiv \sum_k \sigma'_{T_i}\sigma'_{T,0} / \sum_k \sigma'^2_{T,0}$ (where k indicates the model or institute, primes indicate deviations from the ensemble mean, and 0 indicates the unperturbed experiment). The global average of each warming pattern contribution $[\alpha_i] = \alpha$ is equivalent to an inter-model regression of perturbed global warming σ_T against unperturbed global warming $\sigma_{T,0}$ (note these averages are subtracted from the patterns in Figure 5.3). While global inter-model relationships between perturbed warming and unperturbed temperature variability are weak ($r^2 \lesssim 10\%$), the pattern relationships can be regionally significant and an help identify similarities with temperature variability. Similarly,

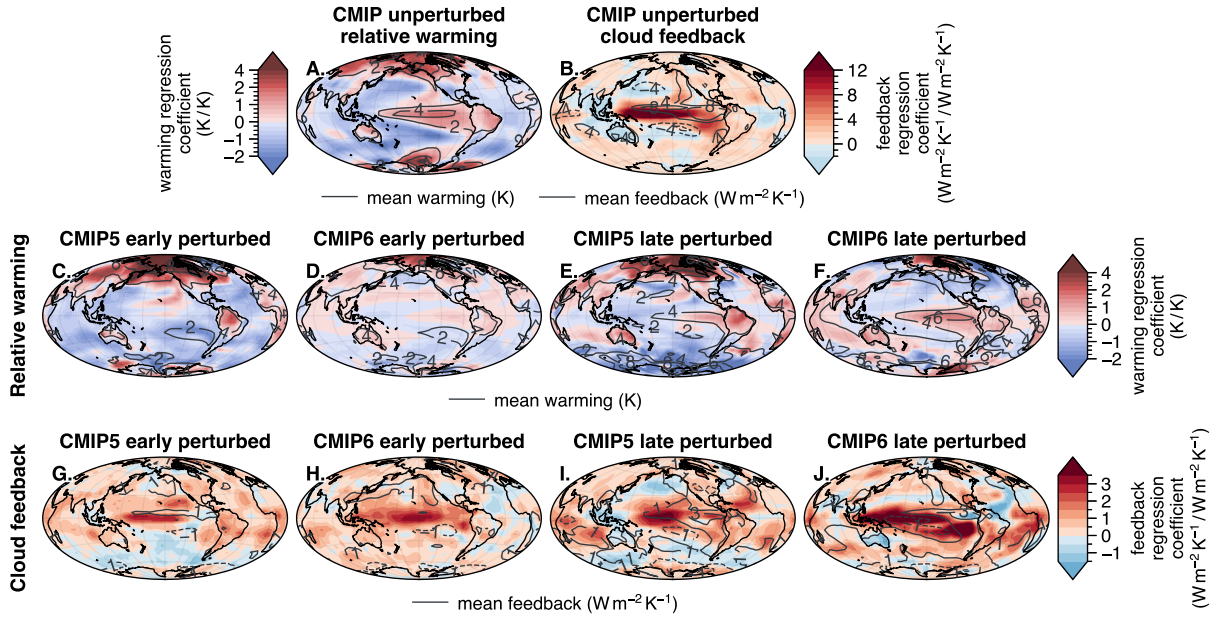

Figure 5.3: Local contributions to inter-model spread in global warming and global cloud feedbacks. The first row indicates inter-model regressions of (A) unperturbed warming patterns onto their global average and (B) unperturbed cloud feedback patterns onto their global average (see text for details). The second and third rows indicate inter-model regressions of (C–F) perturbed warming patterns against global average unperturbed warming and (G–J) perturbed cloud feedback patterns against global average unperturbed cloud feedbacks for the CMIP generation and perturbation response time indicated along columns. In each panel, shading indicates inter-model regression coefficients and contours indicate the multi-model average patterns from Figure 5.1. For the warming pattern panels (A, C–F), the global average regression coefficient is subtracted.

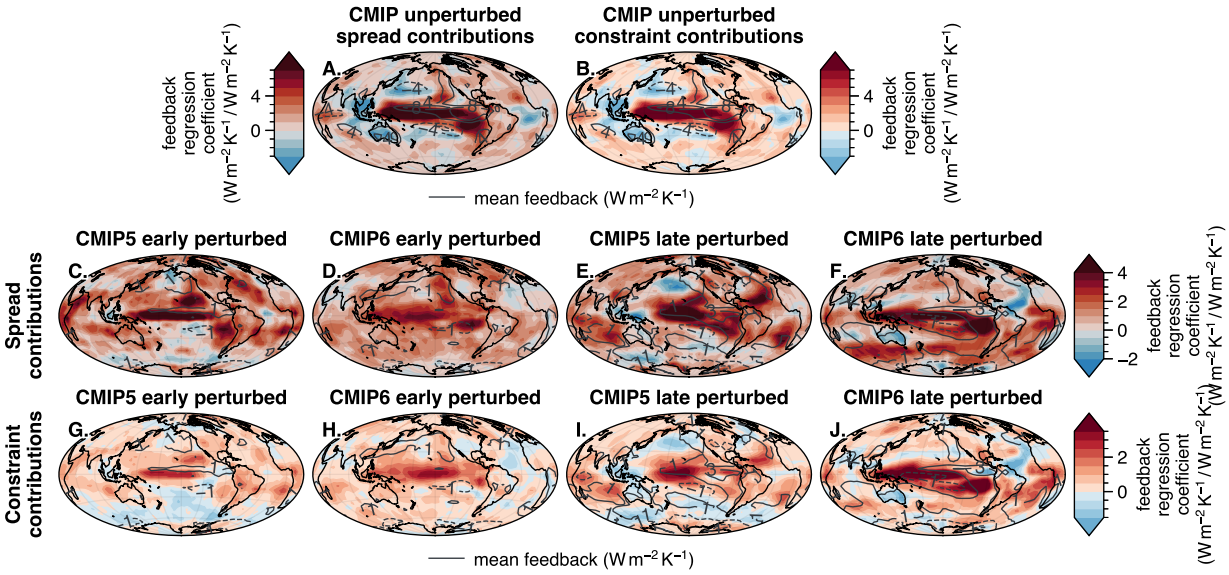

Figure 5.4: As in Figure 5.3 but showing local contributions to inter-model spread in global cloud feedbacks alongside local contributions to the unperturbed global cloud feedback constraints. The first row shows regressions of cloud feedback patterns against global cloud feedbacks from the CMIP generation and response period indicated along columns; each panel thus indicates local contributions to the global cloud feedback spread shown in Figure 4.2. The second row is as in Figure 5.3; each panel indicates local contributions to the regression coefficients shown in Figure 4.3. Note that panels A and B are identical by construction.

I define the feedback pattern contributions β_i shown in Figure 5.3 (panels B, G–J) as inter-model regressions of each feedback pattern λ_i onto the unperturbed global cloud feedback parameter λ_0, i.e. $\beta_i \equiv \sum_k \lambda_i' \lambda_0' / \sum_k \lambda_0'^2$. The global average of each feedback pattern contribution $[\beta_i] = \beta$ is equivalent to an inter-model regression coefficient of λ against λ_0 from Figure 4.3. Also note that the cloud feedback pattern regressions onto unperturbed global cloud feedbacks in Figure 5.3 are qualitatively similar to regressions onto the perturbed global cloud feedbacks themselves (Figure 5.4) – thus, just as the cloud feedback constraints (Figure 4.3) are influenced by perturbed cloud feedback spread (Figure 4.2), pattern contributions to cloud feedback constraints are strongly influenced by pattern contributions to cloud feedback spread.

Across CMIP5 and CMIP6, higher global temperature variability is associated with an amplification of the El Niño-like East Pacific pattern that drives the variability (Figure 5.3, A; compare shading and contours). Likewise, models with higher global temperature variability exhibit amplified El Niño-like East Pacific warming in the late perturbed response (Figure 5.3, E, F, red shading). The East Pacific region connected to internal variability is very broad for the CMIP6 ensemble, closely matching the region driving unperturbed global temperature variability, while it is narrower and weaker for the CMIP5 ensemble (compare A to E and F, Figure 5.3). CMIP6 also exhibits a weak relationship between early perturbed East Pacific warming and unperturbed variability, while CMIP5 exhibits no such relationship (compare H and G, J and I; Figure 5.3). The CMIP5 warming pattern connected to internal variability is also characterized by strong hemispheric asymmetry, while the CMIP6 pattern exhibits little hemispheric asymmetry (compare C and D, E and F, Figure 5.3).

Consistent with its role in guiding global temperature variability, the tropical Pacific dominates inter-model spread in unperturbed global cloud feedbacks (Figure 5.3, B). Likewise, the predictability of perturbed global cloud feedbacks from unperturbed cloud feedbacks largely derives from tropical Pacific clouds (compare B and G–J; Figure 5.3). The tropical contributions are stronger in the late response than the early response, especially for CMIP6 (compare H and G, J and I, Figure 5.3). The predictability of perturbed shortwave and longwave cloud feedbacks is like-

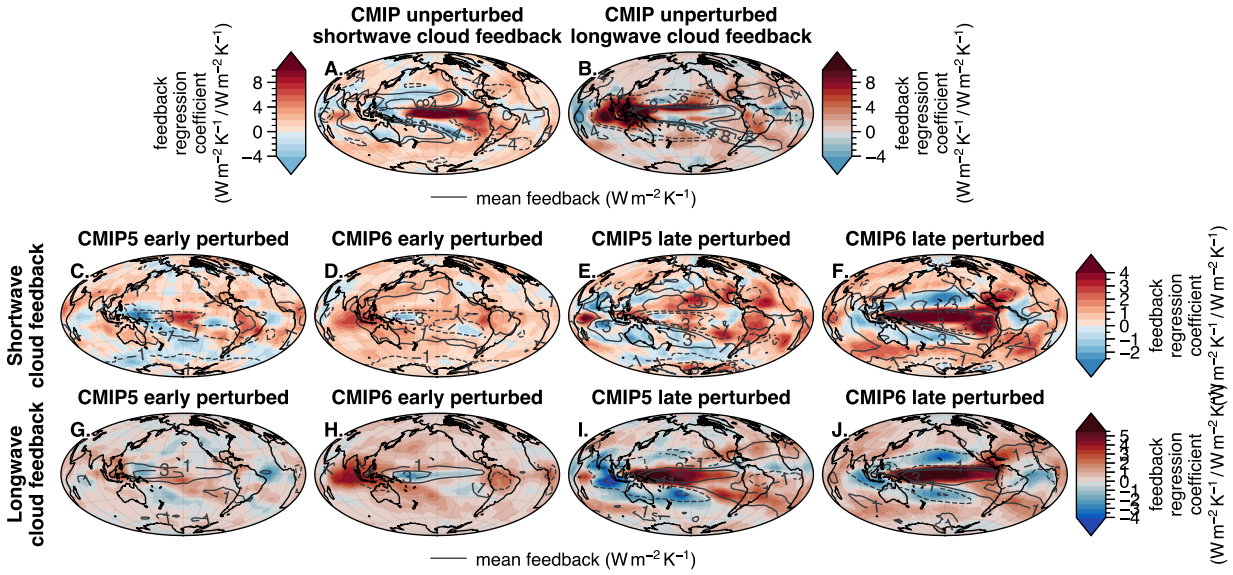

Figure 5.5: As in Figure 5.3 but for the shortwave and longwave cloud feedbacks. Panel A and the first row indicate regression coefficients for the shortwave component of the cloud feedback. Panel B and the second row indicate regression coefficients for the longwave component of the cloud feedback.

wise due to tropical clouds: Constraints on the early response are determined by clouds over the maritime continent, corresponding to spread in the initial La Niña-like response (Figure 5.5, C, D, G, H), while constraints on the late response are determined by clouds over the central and eastern tropical Pacific (plus compensating negative contributions from subtropical clouds), corresponding to spread in the eventual El Niño-like response (Figure 5.5, E, F, I, J). While the extratropics play a smaller role on the cloud feedback constraints, the sign of contributions from Southern Ocean clouds switches from negative to positive between CMIP5 and CMIP6 (compare G and H, I and J; Figure 5.3).

Overall, the above results demonstrate that tropical clouds dominate both inter-model cloud feedback spread and perturbed cloud feedback constraints. However, Southern Ocean clouds contribute significantly to the different strengths of the CMIP5 and CMIP6 constraints. This is more clearly illustrated by zonal averages: the Southern Ocean and tropics contribute comparably to the increased predictability of the late CMIP6 response, while the Southern Ocean actually dominates the increased predictability of the early CMIP6 response (Figure 5.6, G). Southern Ocean contributions are also evident for each of the shortwave and longwave components, indicating a role for

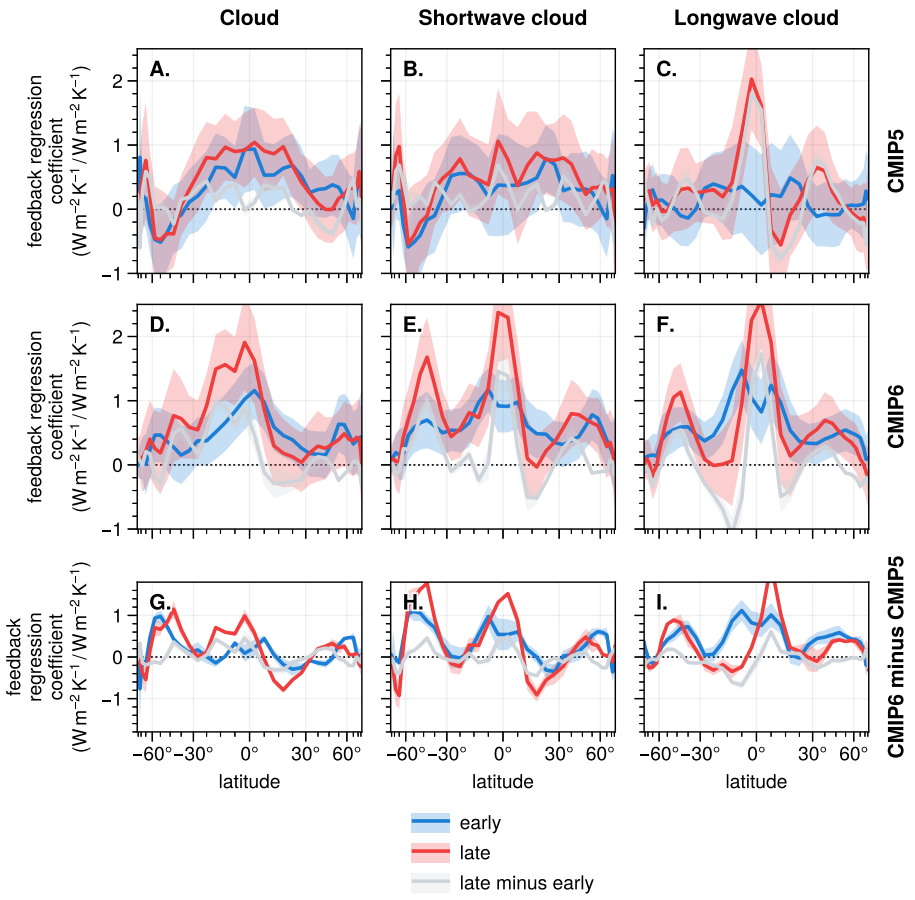

Figure 5.6: As in Figure 5.3 but showing zonal averages and including the shortwave and longwave cloud feedback. Blue, red, and gray lines indicate inter-model regression coefficients for early perturbed, late perturbed, and late minus early perturbed feedback patterns (respectively) regressed onto global unperturbed feedbacks. The first, second, and third rows indicate regression coefficients for CMIP5 models, CMIP6 models, and their difference (respectively). The columns indicate the feedback components used for the inter-model regressions.

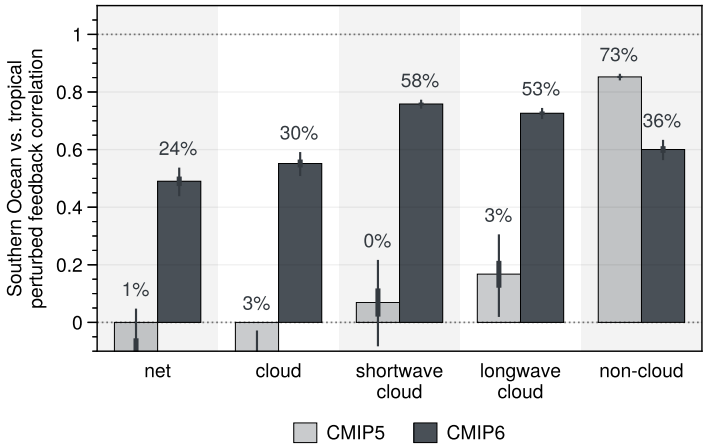

Figure 5.7: Inter-model relationships between perturbed tropical and Southern Ocean feedbacks. Bars indicate correlation coefficients between full (year 0–150) perturbed climate feedbacks averaged over 1) the tropics (30°S to 30°N) and 2) the Southern Ocean (60°S to 30°S). Pale and dark colors indicate the CMIP5 and CMIP6 ensembles, respectively. Thin whiskers (thick whiskers) indicate the 99% (90%) uncertainty ranges according to two-sided student's t tests. Annotations indicate the percent variance explained (i.e., squared correlation coefficient r^2) for the associated regression models.

both shallow and convective clouds (Figure 5.6, H–I). The role of the Southern Ocean on unperturbed feedback constraints may appear surprising, given that extratropical clouds contribute little to unperturbed global cloud feedbacks (Figure 5.1, B) and the extratropical circulation responses to El Niño are distinct from the responses to increasing CO_2 (*Lu et al.* 2008). However, rather than arising from direct connections to tropical variability, the enhanced CMIP6 contributions may simply arise from strong inter-model correlations with tropical cloud feedbacks that are entirely absent from CMIP5 (Figure 5.7). This correlation may be related to weaker negative cloud-phase feedbacks and strengthened positive low-level cloud feedbacks over the Southern Ocean (*Lutsko et al.* 2021, *Zelinka et al.* 2020), which could lead to cloud responses over extratropical oceans that more closely resemble cloud responses over the tropics. The high correlation is evident for both response timescales (not shown), consistent with the increased predictability of both early and late cloud feedbacks in CMIP6 (Figure 4.3). The Southern Ocean contributions could also be related to two-way teleconnections between the tropics and Southern Ocean in some CMIP6-era models (*Dong et al.* 2022, *Kim et al.* 2022, *Luongo et al.* 2023). The presence of these teleconnec-

tions in each CMIP ensemble, their effect on regional cloud feedbacks, and their consistency with observations requires further investigation.

Chapter 6

Conclusions and discussion

6.1 Dynamical core model

In the first part of this thesis (Chapter 2), I explored how the forcing-feedback framework can be adapted for use with idealized general circulation models. I found that the thermal relaxation coefficient used with dynamical core models (i.e., the *relaxation feedback parameter*) is analogous to the local climate feedback parameter, and the inverse average of the thermal relaxation coefficient (i.e., the *relaxation sensitivity parameter*) is analogous to the reference climate sensitivity parameter. Correspondingly, the warming response to forcing perturbations is proportional to the thermal relaxation timescale (Figure 2.1; Figure 3.4, B), and latitude-height patterns of relaxation coefficients that resemble clear-sky radiative kernels from more complex models lead to similar latitude-height patterns of warming (Figure 2.2; Figure 3.5, A–C). Dynamical core models are thus effective tools for studying relationships between climate sensitivity, climate feedbacks, and the large-scale circulation.

I then used this adapted relaxation feedback framework to identify the first-order effects of climate feedbacks on the global circulation (Chapter 3). I found that, given the same equilibrium temperature and the same spatial pattern of feedbacks, lower relaxation climate sensitivity (i.e., shorter relaxation timescales) is associated with a more vigorous large-scale circulation (Figure 3.1), including increased thermal diffusivity and stronger and more poleward storm tracks and eddy-driven jets (Figure 3.2). Differences in the large-scale circulation under different relaxation climate sensitivities are effectively characterized by energetic constraints: Lower relaxation climate sensitivity leads to stronger thermal forcing in the extratropics that must be balanced by enhanced eddy static energy transport and thus stronger storm tracks in the steady-state average; in the model, this balance is accomplished by reductions in both baroclinicity and thermal diffusivity. This suggests that expected increases in equilibrium climate sensitivity under future warming

scenarios (e.g., *Meraner et al.* 2013, *Senior and Mitchell* 2000, *Williams et al.* 2008) may further complicate a mechanistic understanding of the circulation response to warming.

I also tested the relaxation feedback framework with a horizontally uniform "global warming" forcing perturbation (Figure 2.4, C). I found that, given the same equilibrium temperature field and same spatial pattern of feedbacks, lower relaxation climate sensitivity leads to a largely weaker large-scale circulation response (Figure 3.5), with less poleward displacement of the storm tracks and eddy-driven jets (Figure 3.7, C–D). The circulation response disappears if the perturbation experiment is repeated with a spatially uniform relaxation feedback parameter (compare Figures 3.5 and 3.6, D–F; Figures 3.7 and 3.8), suggesting that the circulation response to homogeneous forcing perturbations is dependent on spatial inhomogeneities in the local feedback parameter and the warming pattern resulting from those inhomogeneities. Notably, under the same latitude-height pattern of relaxation feedback parameters (Figure 2.4, B), I found that relaxation climate sensitivity has relatively little effect on the magnitude of the storm track intensity response to forcing perturbations (Figure 3.7, A–B). This is because the eddy energy transport response is constrained by the energy budget response, which itself is the summation of 1) a constant forcing perturbation and 2) a mostly constant thermal forcing response arising from local temperature perturbations that are necessarily proportional to the local feedback parameters (Equation 2.2). The storm track intensity may thus have simpler constraints than most other aspects of the extratropical circulation.

It is important to emphasize that the latitude-height patterns of relaxation feedback parameters used in these experiments are highly idealized (Figure 2.2, D). Instead of matching the radiative feedback parameters from coupled GCMs (Equations A.4 and A.5), I scaled the idealized HS94 relaxation coefficients by constant factors. For greater consistency with more realistic estimates of the radiative feedback kernel and climate sensitivity parameter (Figure 2.2, C; Figure 2.1, red and blue lines), an alternative configuration might be obtained by 1) decreasing the depth of the boundary layer, 2) increasing the average thermal relaxation timescale, and 3) increasing the meridional equilibrium temperature gradient (to compensate for the effect of larger relaxation timescales on circulation intensity). Nevertheless, the unadjusted HS94 configuration was sufficient to repro-

duce the typical warming pattern generated by coupled GCMs with impressive fidelity (Figure 3.5, A–C). This suggests that the HS94 amplified boundary layer relaxation used in nearly all modern dynamical core model studies is as important to the maintenance of a realistic climate as it is to the realization of a realistic response to forcing perturbations.

Past dynamical core model studies of the circulation response to global warming have used localized heating terms to generate the warming patterns associated with spatially dependent climate feedback mechanisms (e.g., *Butler et al.* 2010, *Lu et al.* 2014, *Mbengue and Schneider* 2013, *Sun et al.* 2013). Other studies have tested the effects of clouds on the circulation by prescribing observational estimates of atmospheric cloud radiative effects into idealized models (*Li et al.* 2020, *Voigt et al.* 2020). But the interpretability of these results is somewhat limited, since the pattern and magnitude of the real-world warming response is itself determined by the circulation (e.g., *Davis and Birner* 2022, *Shaw* 2019, *Shaw and Tan* 2018). I therefore suggest that future studies use a "relaxation timescale-aware" approach to simulating global warming in dynamical core models. Relaxation timescales encode a first-order representation of the coupling between entropy-increasing processes and the atmospheric circulation, rather than the average diabatic heating that results from that coupling (*Shaw* 2019, *Shaw and Tan* 2018). Thus, by using relaxation timescales to model spatially dependent feedback mechanisms, the dynamics are given freedom to determine the combined warming patterns and circulation adjustments ultimately generated by forcing perturbations. Section 6.3 provides a thorough discussion of possible future research opportunities with the relaxation feedback framework.

6.2 Coupled models

In the second part of this thesis, I sought to identify the relationships between climate feedbacks and the global circulation across the CMIP5 (*Taylor et al.* 2012) and CMIP6 (*Eyring et al.* 2016) coupled model ensembles. However I first wanted to identify differences in the climate feedback definitions themselves across different experiments and perturbation response times. In the process, I developed emergent constraints on perturbed climate feedbacks based on unperturbed in-

ternal variability. I found that 1) cloud feedbacks are more closely related to internal, unperturbed variability in CMIP6 than CMIP5; 2) cloud feedbacks associated with the slow response to increasing CO_2 are more closely related to unperturbed variability than the fast, transient response; and 3) the relationship between internal cloud feedbacks and the feedbacks associated with increasing CO_2 is related to their projection onto (ENSO-dominated) internal global temperature variability.

Importantly, constraints based on internal variability depend only on the ability of CMIP models to simulate a realistic warming pattern and realistic cloud forcing adjustments in response to suppressed deep water upwelling in the East Pacific cold tongue. This stands in contrast to constraints derived from observed global warming (*Nijsse et al.* 2020, *Tokarska et al.* 2020a), which arguably violate a necessary condition for the validity of emergent constraints due to systematic biases in model-simulated historical warming patterns (*Caldwell et al.* 2018, *Hall et al.* 2019, *Heede et al.* 2020, *Marvel et al.* 2018). Since observed and modeled ENSO-driven internal variability are associated with more positive cloud feedbacks (*Bellomo et al.* 2014, *He et al.* 2021, *Kolly and Huang* 2018, *Middlemas et al.* 2019, *Rädel et al.* 2016), these results suggests that negative or only weakly positive net cloud feedbacks are difficult to reconcile with amplified East Pacific warming. This further raises the specter of accelerated future warming if Earth's Pacific warming pattern shifts to align better with expectations from simple energy balance models (Figure 1.2; see caption for details), coupled climate models (*Andrews et al.* 2015, 2022, *Rugenstein et al.* 2020), and lines of paleoclimate evidence (*Liu et al.* 2019, *Sherwood et al.* 2020, *Tierney et al.* 2019, 2020) in the coming decades to centuries.

For an emergent constraint to be robust or meaningful, we require a verifiable physical mechanism that can explain the inter-model relationship (*Caldwell et al.* 2018, *Hall et al.* 2019). I hypothesize that the unperturbed feedback constraints described above can be understood through the lens of fluctuation-dissipation relation (FDR). The FDR states that the dissipative response of a physical system to external perturbations is related to the internal fluctuations of that system (*Kubo* 1966, *Leith* 1975). The suitability of FDR for a climate model response should depend on both 1) the allowance of sufficient time for the dissipative response to be realized in the absence of addi-

tional forcing, and 2) the resemblance of the dissipative response to internal modes of fluctuation. The pattern contribution results thus bolster this hypothesis (*Caldwell et al.* 2018): I found that unperturbed feedback constraints are both 1) more effective for the slow part of the response to forcing perturbations than the fast, transient response (Figure 5.1), and 2) are largely driven by inter-model differences in tropical warming and tropical cloud responses rather than extratropical uncertainty (Figure 5.3).

The cloud feedback constraints described here arise despite vastly different forcings and extratropical circulation responses associated with unperturbed and perturbed global warming (i.e., El Niño-induced suppressed tropical cold water upwelling and equatorward shifts in the circulation, versus CO_2-induced suppressed outgoing longwave flux at all latitudes and poleward shifts in the circulation *Huang et al.* 2016, *Lu et al.* 2008, *Sun et al.* 2013, *Zhang and Huang* 2014). This may indicate distinct similarities of cloud feedback mechanisms and their sources of uncertainty across different modes of climate forcing. Since non-cloud feedbacks are closely tied to near-surface and extratropical processes (i.e., altered lapse rates, reduced polar surface albedo, land warming-driven relative humidity change; *Byrne and O'Gorman* 2016, *Colman and Soden* 2021, *Lambert and Taylor* 2014, *Sherwood et al.* 2010, *Thackeray and Fletcher* 2016), and since ENSO-driven variability and greenhouse gas warming are characterized by distinct effects on the surface and in the extratropics (*He et al.* 2021, *Lu et al.* 2008, *Po-Chedley et al.* 2018, *Sun et al.* 2013, *Trenberth et al.* 2010), internal variability provides very weak constraints (Figure 4.3, far right). By contrast, since cloud feedbacks are determined more broadly by the tropical and subtropical circulation adjustments associated with Pacific warming (*Bony and Dufresne* 2005, *Fasullo and Trenberth* 2012, *Hartmann and Larson* 2002, *Mackie and Byrne* 2022, *Schiro et al.* 2022), internal variability is able to provide much stronger constraints (Figure 4.3, center left). The distinction between "forcing" and "response" may also become blurred under long-term warming, with the cloud responses to East Pacific warming under CO_2 forcing resembling the cloud adjustments associated with East Pacific forcing under ENSO-driven variability (*Lutsko* 2018, *Lutsko and Takahashi* 2018, Section 6.3).

The comparative predictability of cloud feedbacks from internal variability is encouraging for prospects of further constraining future global warming. Clear-sky feedbacks exhibit lower spread and are driven by a narrower array of processes that can be more easily dissected by physical theory and existing model hierarchies (e.g., *Colman and Soden* 2021, *Held and Soden* 2000, *Ingram* 2013, *Jeevanjee et al.* 2021a, *Rose and Rencurrel* 2016, *Seeley and Jeevanjee* 2021, *Zhang et al.* 2020), while cloud feedbacks are driven by a much more complex array of dynamic and energetic processes (e.g., *Bretherton* 2015, *Ceppi and Hartmann* 2015, *Ceppi et al.* 2017, *Murray et al.* 2021, *Myers et al.* 2021, *Schiro et al.* 2022, *Scott et al.* 2020, *Stephens* 2005). However, this picture is complicated by the relatively weak extratropical warming associated with internal variability combined with the relatively stronger role of Southern Ocean clouds on both inter-model spread and constraints in CMIP6 (Figure 5.7). More sophisticated constraints on global cloud feedbacks will depend critically on the realism of Southern Ocean cloud responses in CMIP6 versus CMIP5 (*Fiddes et al.* 2022, *Lutsko et al.* 2021, *McCoy et al.* 2015, *Schuddeboom and McDonald* 2021, *Tan et al.* 2016, *Wall et al.* 2022b, *Zelinka et al.* 2020), and may require incorporating regional processes and other modes of internal variability to better understand non-tropical cloud feedback spread (*Ceppi and Hartmann* 2015, *Lutsko et al.* 2022, *McCoy et al.* 2020, *Wall and Hartmann* 2015, *Wall et al.* 2022a). Future work should seek to build a stronger understanding of teleconnections between regional cloud responses and their interactions with warming patterns, along with a stronger theoretical understanding of the relationships between different modes of tropical variability and simulated responses to forcing. Where possible, both of these tasks may be aided by model hierarchy approaches (*Held* 2005, *Jeevanjee et al.* 2017, *Kang et al.* 2019, *Maher et al.* 2019, *Medeiros et al.* 2015, *O'Gorman and Schneider* 2008, *Russotto and Biasutti* 2020).

6.3 Interpretation

Chapter 5 was initially intended to test whether the relationships between prescribed relaxation feedbacks and the global circulation described in Chapter 3 could help us understand inter-model spread in more complex models. I started by quantifying climate feedbacks using a traditional,

surface-relative forcing-feedback framework rather than the relaxation feedback framework from Chapter 2. Ultimately, the broad differences between traditional climate feedbacks and relaxation climate feedbacks prevented any more direct comparisons of these results. This was due to a few key factors. First, while relaxation feedbacks are constant by construction (Figure 2.2), traditional climate feedbacks vary in their magnitude and spatial patterns depending on the CMIP generation, perturbation response time, and whether the response is driven by internal variability or external forcing perturbations (Section 4.1; Figure 4.2). Second, due to the remote physical connection between surface temperature and top-of-atmosphere radiation, traditional climate feedbacks are subject to complex, two-way interactions with the circulation that are absent from the relaxation feedback framework (e.g., *Feldl and Roe* 2013b, *Grise and Kelleher* 2021, *Grise et al.* 2019, *Williams et al.* 2023). Finally, traditional feedbacks exhibit highly regional sources of feedback uncertainty, with amplified inter-model spread over the tropics and (in CMIP6) the Southern Ocean (Figure 5.1, contours), while experiments with scaled relaxation timescales result in more homogeneous feedback changes (Figure 2.2, D).

Overall, the substantial uncertainty associated with traditional climate feedbacks, combined with the diverse array of processes responsible for establishing these feedbacks (see Section 4.1), renders the interpretation of pattern effects and inter-model relationships difficult (*Feldl and Roe* 2013b, *Kajtar et al.* 2021, *Stevens et al.* 2016, *Williams et al.* 2023). This encourages us to seek novel, alternative frameworks that 1) explicitly account for patterns and circulation adjustments in the response, and 2) are largely robust to different forcings and constant in time. An early attempt at such a framework used a simple variant of the traditional feedback based on *local* surface temperature rather than global temperature (*Armour et al.* 2012, *Boer and Yu* 2003a,b, *Feldl and Roe* 2013a). According to this framework, the time-dependence of the global feedback parameter could be captured by the product of constant local feedbacks with time-varying warming patterns. However, subsequent work found that these feedbacks are just as non-robust as feedbacks based on global temperature (*Andrews et al.* 2015, *Hedemann et al.* 2022, *Po-Chedley et al.* 2018), but without the convenient role of the latter as a spatial decomposition of the global feedback parame-

ter (see Section 5.2). A more recent, promising framework is the Green's function approach, under which global, circulation-adjusted radiative responses to local temperature changes are estimated from successive simulations with perturbed-sea surface temperature "patches" in atmosphere-only GCMs (*Bloch-Johnson et al.* 2020, 2023, *Dong et al.* 2019, *Zhou et al.* 2017). Others have decomposed the response to forcing patterns instead of warming patterns: Some have estimated the warming and circulation responses to prescribed patches or bands with anomalous ocean heat uptake (*Liu et al.* 2018a,b, *Rose et al.* 2014, *Rugenstein et al.* 2016a), while others have estimated the responses to bands with prescribed CO_2 increases (*Shaw and Tan* 2018, *Stuecker et al.* 2018) or prescribed diabatic heating (*Baker et al.* 2017, *Kang and Xie* 2014).

The relaxation feedback framework may be an appealing alternative. Instead of linearizing the circulation adjustments into our spatial forcing and feedback definitions (as with Green's functions and ocean heat uptake patterns), relaxation feedbacks take the opposite approach of entirely separating circulation adjustments from the concept of the "climate feedback" by using local, linearized sensitivity to local changes in temperature, humidity, and clouds (see Appendix A.2). For example, under the relaxation feedback framework, positive polar lapse rate feedbacks and negative tropical lapse rate feedbacks arise from interactions between a freely-evolving circulation and a fixed feedback pattern (Figure 3.5). The core assumptions of this approach are that 1) relaxation feedbacks estimated from complex models are more linear and less sensitive to forcing and circulation differences than traditional feedbacks, and 2) relaxation feedbacks can successfully reproduce the large-scale responses to forcing perturbations from more complex models. While I have yet to explicitly test the first assumption, Chapter 2 and the close analogy between relaxation feedbacks and radiative kernels are encouraging. Radiative kernels are known to be more robust than traditional feedbacks themselves (hence the term "kernels"), and tend to produce similar breakdowns of traditional climate feedbacks when applied to different model data (see Section 4.1; *Soden et al.* 2008, *Zelinka et al.* 2020). Likewise, Chapter 3 is encouraging for the second assumption, since the resemblance of the *Held and Suarez* (1994) latitude-height relaxation feedback field to clear-sky radiative kernels (Figure 2.2) was sufficient to reproduce the canonical latitude-height warming

response to a forcing perturbation (Figure 3.5). Notably, *Henry and Merlis* (2019) also found that linearizing the Planck response to increasing optical depth in a gray radiation model (*Frierson et al.* 2006, 2007) results in similar warming patterns compared to non-linear radiation.

6.4 Reconciling the frameworks

While the relaxation feedback framework seems promising, there are important gaps between traditional and relaxation feedbacks that must be bridged before we can use the framework to address more complex problems. First, the role of surface-atmosphere energetic exchange in guiding the response to forcing is difficult to interpret in the context of relaxation feedbacks. The real world responds to increased CO_2 through the combined effects of reduced radiative cooling in the troposphere and net radiative heating at the surface (*Huang et al.* 2016, 2017, *Jeevanjee et al.* 2021b, *Zhang and Huang* 2014). The surface heating is subsequently communicated to the atmosphere via turbulent sensible and latent heat fluxes and radiative exchange with the atmosphere, combined with increased emission to space through the atmospheric window (e.g., *Hartmann* 2015, *Petty* 2006). While this surface pathway accounts for only a part of the longwave feedback, it accounts for a large majority of the shortwave cloud and surface albedo feedbacks, since the atmosphere is largely transparent to shortwave radiation. This is critical, since modeled responses to increasing CO_2 are driven substantially (or possibly even entirely) by shortwave energy accumulation rather than longwave accumulation (*Donohoe et al.* 2014, *Trenberth and Fasullo* 2009).

There may be several paths forward for reconciling surface-atmosphere interactions with the relaxation feedback framework. Most simply, if we base our relaxation feedbacks around top-of-atmosphere (TOA) radiative responses rather than net atmospheric (i.e., TOA minus surface) radiative responses, this may implicitly encode the missing surface-atmosphere interactions. As described in Chapter 2, it is possible that the amplified near-surface radiative kernels inferred from observations and assigned to the *Held and Suarez* (1994) configuration already reflect these missing interactions (Figure 2.2). More realistically, we might explicitly resolve surface-atmosphere exchange within the relaxation feedback framework by 1) coupling the atmosphere with an ideal-

ized surface that interacts with the atmosphere through turbulent heat flux parameterizations, then 2) encoding relaxation feedbacks based on both surface and top-of-atmosphere radiative responses rather than just top-of-atmosphere responses (*Huang and Zhang* 2014, *Huang et al.* 2016, 2017). This could also be done in a model with an explicit hydrological cycle and an ocean surface instead of a dry model (see Section 6.5).

Second, relaxation feedbacks seem to blur some of the traditional distinctions between climate forcings and feedbacks. The radiative forcing is typically defined as the summation of 1) a direct radiative imbalance due to some forcing agent (e.g., CO_2) and 2) an indirect radiative imbalance due to rapid surface and atmospheric adjustments (e.g., *Hansen et al.* 1997, *Sherwood et al.* 2015). The adjustments reflect thermodynamic and circulation changes that occur in the absence of significant ocean surface warming; they include stratospheric cooling, tropospheric warming, land surface warming, wind and cloud changes, and even ocean surface warming patterns (*Andrews and Forster* 2008, *Colman and McAvaney* 2011, *Gregory and Webb* 2008, *Hansen et al.* 1997, *Rugenstein et al.* 2016b, *Sherwood et al.* 2015, *Wang and Huang* 2019). By contrast, under the relaxation feedback framework, forcing adjustments are encoded into the "feedback" part of the climate response – tropospheric temperature simply takes on the same conceptual role as ocean surface temperature in driving the response (Equation 2.2). Thus, the forcing term in the relaxation feedback framework reflects only the direct radiative effects of forcing agents rather than the indirect effects of rapid adjustments by the surface and atmosphere.

I argue that this blurring between feedbacks and forcing adjustments may be an advantage rather than a deficiency of the relaxation feedback framework. Since the traditional framework was adopted, it has required assigning an increasingly diverse array of dynamic and thermodynamic processes into the "adjustment" category (e.g., *Hartmann* 2015, *Sherwood et al.* 2015). Rather than characterizing distinct processes, the adjustments establish the canonical warming patterns and circulation changes typically associated with global warming (i.e., polar amplification, moist adiabatic adjustment, poleward shifts in the circulation, and related cloud changes; *Grise and Polvani* 2014, 2016, *Rugenstein et al.* 2016b, *Wang and Huang* 2019, *Xia and Huang* 2017). Thus,

under the traditional framework, feedbacks are unable to uniquely account for either the pattern of the response or the warming and circulation changes that best characterize the response. The premise of top-of-atmosphere forcing also breaks down under internal variability, since energetic exchanges within the atmosphere and between the surface are more relevant to internal variability than the TOA energy budget (*Lutsko* 2018, *Lutsko and Takahashi* 2018, *Olonscheck and Rugenstein* 2023, *Trenberth et al.* 2010). By contrast, since relaxation forcings and feedbacks are vertically resolved, they should be able to characterize both unperturbed variability and perturbed responses.

6.5 Future work

The surface-driven perspective of climate change expressed by traditional climate feedbacks is an obvious first choice for linearizing the response to increasing greenhouse gases (*Hansen et al.* 1985, *Roe* 2009, *Rugenstein and Armour* 2021). Much of the response does seem to be driven by the surface, given the large thermal inertia of the ocean and the importance of surface emission through the atmospheric window for balancing radiative forcing. Moreover, this perspective is more clearly relevant for human impacts, easier to observationally constrain and describe with energy balance models, and has led to substantial advances in our understanding of global warming. However, as climate research has matured, important deficits of this formulation have become clear. I argue an atmosphere-driven perspective of climate change expressed by relaxation feedbacks may serve as a useful companion to the traditional framework. Under atmosphere-driven climate change, climate feedbacks and forcing adjustments are combined, and the ocean simply serves as a reservoir of thermal inertia that extends the timescale and modulates the time-evolving patterns of the response. This is more consistent with the ability of rapid forcing adjustments to establish the primary signals of the response, and more cleanly partitions the dynamic and thermodynamic adjustments associated with the response. Further, surface-relative feedbacks can be derived *a posteriori* from model experiments employing prescribed relaxation feedbacks (Figure 3.4) – thus, they are still compatible with the traditional framework, and may even help us better understand uncertainties in both traditional climate feedbacks and the surface climate sensitivity.

In addition to its physical advantages, the relaxation feedback framework offers promising opportunities for developing model hierarchies compatible with a linear, forcing-feedback perspective of climate change. This could help fill gaps in the hierarchy commonly used by forcing-feedback studies (*Jeevanjee et al.* 2017, *Maher et al.* 2019), which mainly consists of 1) highly idealized energy balance models and climate model emulators, with no explicit dynamics or cloud effects (e.g., *Castruccio et al.* 2014, *Geoffroy et al.* 2013b, *Hasselmann* 1976, *Held et al.* 2010, *North et al.* 1981), and 2) highly complex coupled models that explicitly simulate both dynamics and cloud effects (e.g., *Eyring et al.* 2016, *Murphy et al.* 2004, *Palmer and Stevens* 2019, *Roe and Baker* 2007, *Taylor et al.* 2012). As discussed in Appendix A.2, we might encode moisture and cloud responses within relaxation feedbacks by adding the linear component of their dependence on air temperature (or by adding parsimonious non-linear terms to the relaxation feedback expression). We might also use relaxation feedbacks with a moist model instead of a dry dynamical core, along with 1) an explicit hydrological cycle, 2) a slab or fully-dynamic ocean, and 3) possibly a humidity dependence term added to the relaxation feedback expression. Such a model could be run with either realistic topography or as a zonally-symmetric aquaplanet, and could be constructed from existing idealized modeling frameworks (*Monteiro et al.* 2018, *Rose* 2018, *Thatcher and Jablonowski* 2016, *Vallis et al.* 2018). Another option that could serve as a more advanced hierarchy member might be to impose spectrally-derived analytic expressions for atmospheric cooling as a function of temperature and humidity (*Jeevanjee and Fueglistaler* 2020a,b); the clear-sky relaxation feedbacks associated with such a model could then be derived from the analytic expressions (e.g., *Jeevanjee et al.* 2021a, *McKim et al.* 2021, *Zhang et al.* 2020).

As a possible first step, we could use this new hierarchy to assess the effects of model differences in local cloud feedbacks on time-evolving surface warming patterns and circulation responses. This could be done by replacing the forcing perturbation H (Equation 2.4) with coupled model estimates of the horizontally and vertically resolved CO_2 forcing, then matching the relaxation feedbacks λ_τ to coupled model estimates of the spatially resolved feedbacks into one of our idealized model configurations. The coupled model feedbacks might be estimated using a variety

of techniques, including 1) simple linear regression of radiative flux divergence against temperature (and optionally, humidity) for a given model layer, using either pre-industrial or abrupt $4\times CO_2$ experiments; 2) multiple linear regression of top-of-atmosphere or surface radiation against the vertical distribution of temperature (and optionally, humidity) in a time-evolving atmospheric column; or 3) by combining traditional radiative kernels (*Soden and Held* 2006, *Soden et al.* 2008) with binned cloud-type radiative kernels (*Kramer et al.* 2019, *Zelinka et al.* 2012, 2016) and translating the cloud-type kernels into physical space according to the cloud properties of individual models. Radiative cooling and heating might then be simulated by 1) pairing the feedbacks with an idealized or model-derived equilibrium temperature field T^{e} (see Chapter 2), or 2) adding constant radiative effects obtained from individual model climatologies to a feedback-determined deviation from that climatology (calculated from the product of the feedbacks with model-simulated temperature and humidity anomalies). I hope to further explore these possibilities in future work.

References

G. Abramowitz and C. H. Bishop. Climate Model Dependence and the Ensemble Dependence Transformation of CMIP Projections. *Journal of Climate*, 28(6):2332–2348, March 2015. ISSN 0894-8755, 1520-0442. doi: 10.1175/JCLI-D-14-00364.1.

Gab Abramowitz, Nadja Herger, Ethan Gutmann, Dorit Hammerling, Reto Knutti, Martin Leduc, Ruth Lorenz, Robert Pincus, and Gavin A. Schmidt. Model dependence in multi-model climate ensembles: Weighting, sub-selection and out-of-sample testing. *Earth System Dynamics Discussions*, pages 1–20, July 2018. ISSN 2190-4979. doi: 10.5194/esd-2018-51.

Michael A. Alexander, Ileana Bladé, Matthew Newman, John R. Lanzante, Ngar-Cheung Lau, and James D. Scott. The Atmospheric Bridge: The Influence of ENSO Teleconnections on Air–Sea Interaction over the Global Oceans. *Journal of Climate*, 15(16):2205–2231, August 2002. ISSN 0894-8755, 1520-0442. doi: 10.1175/1520-0442(2002)015<2205:TABTIO>2.0.CO;2.

V. A. Alexeev, P. L. Langen, and J. R. Bates. Polar amplification of surface warming on an aquaplanet in "ghost forcing" experiments without sea ice feedbacks. *Climate Dynamics*, 24(7-8): 655–666, June 2005. ISSN 0930-7575, 1432-0894. doi: 10.1007/s00382-005-0018-3.

Myles R. Allen and William J. Ingram. Constraints on future changes in climate and the hydrologic cycle. *Nature*, 419(6903):228–232, September 2002. ISSN 1476-4687. doi: 10.1038/nature01092.

Thomas R. Anderson, Ed Hawkins, and Philip D. Jones. CO2, the greenhouse effect and global warming: From the pioneering work of Arrhenius and Callendar to today's Earth System Models. *Endeavour*, 40(3):178–187, September 2016. ISSN 0160-9327. doi: 10.1016/j.endeavour.2016.07.002.

Timothy Andrews and Piers M. Forster. CO2 forcing induces semi-direct effects with consequences for climate feedback interpretations. *Geophysical Research Letters*, 35(4), 2008. ISSN 1944-8007. doi: 10.1029/2007GL032273.

Timothy Andrews and Mark J. Webb. The Dependence of Global Cloud and Lapse Rate Feedbacks on the Spatial Structure of Tropical Pacific Warming. *Journal of Climate*, 31(2):641–654, January 2018. ISSN 0894-8755, 1520-0442. doi: 10.1175/JCLI-D-17-0087.1.

Timothy Andrews, Jonathan M. Gregory, Mark J. Webb, and Karl E. Taylor. Forcing, feedbacks and climate sensitivity in CMIP5 coupled atmosphere-ocean climate models. *Geophysical Research Letters*, 39(9), May 2012. ISSN 1944-8007. doi: 10.1029/2012GL051607.

Timothy Andrews, Jonathan M. Gregory, and Mark J. Webb. The Dependence of Radiative Forcing and Feedback on Evolving Patterns of Surface Temperature Change in Climate Models. *Journal of Climate*, 28(4):1630–1648, February 2015. ISSN 0894-8755. doi: 10.1175/JCLI-D-14-00545.1.

Timothy Andrews, Jonathan M. Gregory, David Paynter, Levi G. Silvers, Chen Zhou, Thorsten Mauritsen, Mark J. Webb, Kyle C. Armour, Piers M. Forster, and Holly Titchner. Accounting for Changing Temperature Patterns Increases Historical Estimates of Climate Sensitivity. *Geophysical Research Letters*, 45(16):8490–8499, 2018. ISSN 1944-8007. doi: 10.1029/2018GL078887.

Timothy Andrews, Alejandro Bodas-Salcedo, Jonathan M. Gregory, Yue Dong, Kyle C. Armour, David Paynter, Pu Lin, Angshuman Modak, Thorsten Mauritsen, Jason N. S. Cole, Brian Medeiros, James J. Benedict, Hervé Douville, Romain Roehrig, Tsuyoshi Koshiro, Hideaki Kawai, Tomoo Ogura, Jean-Louis Dufresne, Richard P. Allan, and Chunlei Liu. On the Effect of Historical SST Patterns on Radiative Feedback. *Journal of Geophysical Research: Atmospheres*, 127(18): e2022JD036675, 2022. ISSN 2169-8996. doi: 10.1029/2022JD036675.

Kyle C. Armour. Energy budget constraints on climate sensitivity in light of inconstant climate feedbacks. *Nature Climate Change*, 7(5):331–335, May 2017. ISSN 1758-6798. doi: 10.1038/nclimate3278.

Kyle C. Armour, Cecilia M. Bitz, and Gerard H. Roe. Time-Varying Climate Sensitivity from Regional Feedbacks. *Journal of Climate*, 26(13):4518–4534, December 2012. ISSN 0894-8755. doi: 10.1175/JCLI-D-12-00544.1.

Kyle C. Armour, John Marshall, Jeffery R. Scott, Aaron Donohoe, and Emily R. Newsom. Southern Ocean warming delayed by circumpolar upwelling and equatorward transport. *Nature Geoscience*, 9(7):549–554, July 2016. ISSN 1752-0894, 1752-0908. doi: 10.1038/ngeo2731.

Kyle C. Armour, Nicholas Siler, Aaron Donohoe, and Gerard H. Roe. Meridional Atmospheric Heat Transport Constrained by Energetics and Mediated by Large-Scale Diffusion. *Journal of Climate*, 32(12):3655–3680, June 2019. ISSN 0894-8755. doi: 10.1175/JCLI-D-18-0563.1.

Svante Arrhenius. On the Influence of Carbonic Acid in the Air upon the Temperature of the Ground. *The London, Edinburgh, and Dublin Philosophical Magazine and Journal of Science*, 41 (251):237–276, April 1896.

Hugh S. Baker, Tim Woollings, and Cheikh Mbengue. Eddy-Driven Jet Sensitivity to Diabatic Heating in an Idealized GCM. *Journal of Climate*, 30(16):6413–6431, May 2017. ISSN 0894-8755. doi: 10.1175/JCLI-D-16-0864.1.

Pragallva Barpanda and Tiffany Shaw. Using the Moist Static Energy Budget to Understand Storm-Track Shifts across a Range of Time Scales. *Journal of the Atmospheric Sciences*, 74(8):2427–2446, April 2017. ISSN 0022-4928. doi: 10.1175/JAS-D-17-0022.1.

Katinka Bellomo, Amy Clement, Thorsten Mauritsen, Gaby Rädel, and Bjorn Stevens. Simulating the Role of Subtropical Stratocumulus Clouds in Driving Pacific Climate Variability. *Journal of Climate*, 27(13):5119–5131, July 2014. ISSN 0894-8755, 1520-0442. doi: 10.1175/JCLI-D-13-00548.1.

J. Bjerknes. A possible response of the atmospheric Hadley circulation to equatorial anomalies of ocean temperature. *Tellus*, 18(4):820–829, January 1966. ISSN 0040-2826. doi: 10.3402/tellusa.v18i4.9712.

J. Bjerknes. Atmospheric Teleconnections from the Equatorial Pacific. *Monthly Weather Review*, 97(3):163–172, March 1969. ISSN 1520-0493, 0027-0644. doi: 10.1175/1520-0493(1969)097<0163:ATFTEP>2.3.CO;2.

Jonah Bloch-Johnson, Maria Rugenstein, and Dorian S. Abbot. Spatial Radiative Feedbacks from Internal Variability Using Multiple Regression. *Journal of Climate*, 33(10):4121–4140, April 2020. ISSN 0894-8755, 1520-0442. doi: 10.1175/JCLI-D-19-0396.1.

Jonah Bloch-Johnson, Maria Rugenstein, Martin B. Stolpe, Tim Rohrschneider, Yiyu Zheng, and Jonathan M. Gregory. Climate Sensitivity Increases Under Higher CO_2 Levels Due to Feedback Temperature Dependence. *Geophysical Research Letters*, 48(4), February 2021. ISSN 0094-8276, 1944-8007. doi: 10.1029/2020GL089074.

Jonah Bloch-Johnson, Maria A.A. Rugenstein, Marc J. Alessi, Cristian Proistosescu, Ming Zhao, Bosong Zhang, Andrew I.L. Williams, Jonathan M. Gregory, Jason Cole, Yue Dong, Margaret L Duffy, Sarah M. Kang, and Chen Zhou. The Green's Function Model Intercomparison Project (GFMIP) Protocol. Preprint, Preprints, March 2023.

G. Boer and B. Yu. Climate sensitivity and response. *Climate Dynamics*, 20(4):415–429, February 2003a. ISSN 1432-0894. doi: 10.1007/s00382-002-0283-3.

G. J. Boer and B. Yu. Climate sensitivity and climate state. *Climate Dynamics*, 21(2):167–176, August 2003b. ISSN 1432-0894. doi: 10.1007/s00382-003-0323-7.

Bert Bolin and Erik Eriksson. Distribution of Matter in the Sea and Atmosphere: Changes in the Carbon Dioxide Content of the Atmosphere and Sea due to Fossil Fuel Combustion. *The atmosphere and the sea in motion*, 1:130–142, 1959.

Lina Boljka, Theodore G. Shepherd, and Michael Blackburn. On the Coupling between Barotropic and Baroclinic Modes of Extratropical Atmospheric Variability. *Journal of the Atmospheric Sciences*, 75(6):1853–1871, March 2018. ISSN 0022-4928. doi: 10.1175/JAS-D-17-0370.1.

Sandrine Bony and Jean-Louis Dufresne. Marine boundary layer clouds at the heart of tropical cloud feedback uncertainties in climate models. *Geophysical Research Letters*, 32(20), 2005. ISSN 1944-8007. doi: 10.1029/2005GL023851.

Sandrine Bony, Gilles Bellon, Daniel Klocke, Steven Sherwood, Solange Fermepin, and Sébastien Denvil. Robust direct effect of carbon dioxide on tropical circulation and regional precipitation. *Nature Geoscience*, 6(6):447–451, June 2013. ISSN 1752-0908. doi: 10.1038/ngeo1799.

David James Brayshaw, Brian Hoskins, and Michael Blackburn. The Storm-Track Response to Idealized SST Perturbations in an Aquaplanet GCM. *Journal of the Atmospheric Sciences*, 65(9): 2842–2860, September 2008. ISSN 0022-4928. doi: 10.1175/2008JAS2657.1.

Christopher S. Bretherton. Insights into low-latitude cloud feedbacks from high-resolution models. *Philosophical Transactions of the Royal Society A: Mathematical, Physical and Engineering Sciences*, 373(2054):20140415, November 2015. doi: 10.1098/rsta.2014.0415.

Christopher S. Bretherton and Peter M. Caldwell. Combining Emergent Constraints for Climate Sensitivity. *Journal of Climate*, 33(17):7413–7430, September 2020. ISSN 0894-8755. doi: 10.1175/JCLI-D-19-0911.1.

Florent Brient. Reducing Uncertainties in Climate Projections with Emergent Constraints: Concepts, Examples and Prospects. *Advances in Atmospheric Sciences*, 37(1):1–15, January 2020. ISSN 0256-1530, 1861-9533. doi: 10.1007/s00376-019-9140-8.

Amy H. Butler, David W. J. Thompson, and Ross Heikes. The Steady-State Atmospheric Circulation Response to Climate Change–like Thermal Forcings in a Simple General Circulation Model. *Journal of Climate*, 23(13):3474–3496, February 2010. ISSN 0894-8755. doi: 10.1175/2010JCLI3228.1.

Amy H. Butler, David W. J. Thompson, and Thomas Birner. Isentropic Slopes, Downgradient Eddy Fluxes, and the Extratropical Atmospheric Circulation Response to Tropical Tropospheric Heating. *Journal of the Atmospheric Sciences*, 68(10):2292–2305, June 2011. ISSN 0022-4928. doi: 10.1175/JAS-D-10-05025.1.

Michael P. Byrne and Paul A. O'Gorman. The Response of Precipitation Minus Evapotranspiration to Climate Warming: Why the "Wet-Get-Wetter, Dry-Get-Drier" Scaling Does Not Hold over

Land. *Journal of Climate*, 28(20):8078–8092, October 2015. ISSN 0894-8755. doi: 10.1175/JCLI-D-15-0369.1.

Michael P. Byrne and Paul A. O'Gorman. Understanding Decreases in Land Relative Humidity with Global Warming: Conceptual Model and GCM Simulations. *Journal of Climate*, 29(24): 9045–9061, December 2016. ISSN 0894-8755, 1520-0442. doi: 10.1175/JCLI-D-16-0351.1.

Peter M. Caldwell, Mark D. Zelinka, Karl E. Taylor, and Kate Marvel. Quantifying the Sources of Intermodel Spread in Equilibrium Climate Sensitivity. *Journal of Climate*, 29(2):513–524, January 2016. ISSN 0894-8755, 1520-0442. doi: 10.1175/JCLI-D-15-0352.1.

Peter M. Caldwell, Mark D. Zelinka, and Stephen A. Klein. Evaluating Emergent Constraints on Equilibrium Climate Sensitivity. *Journal of Climate*, 31(10):3921–3942, May 2018. ISSN 0894-8755, 1520-0442. doi: 10.1175/JCLI-D-17-0631.1.

G. S. Callendar. The artificial production of carbon dioxide and its influence on temperature. *Quarterly Journal of the Royal Meteorological Society*, 64(275):223–240, April 1938. ISSN 00359009. doi: 10.1002/qj.49706427503.

Mark A. Cane, Amy C. Clement, Alexey Kaplan, Yochanan Kushnir, Dmitri Pozdnyakov, Richard Seager, Stephen E. Zebiak, and Ragu Murtugudde. Twentieth-Century Sea Surface Temperature Trends. *Science*, 275(5302):957–960, February 1997. doi: 10.1126/science.275.5302.957.

Stefano Castruccio, David J. McInerney, Michael L. Stein, Feifei Liu Crouch, Robert L. Jacob, and Elisabeth J. Moyer. Statistical Emulation of Climate Model Projections Based on Precomputed GCM Runs. *Journal of Climate*, 27(5):1829–1844, March 2014. ISSN 0894-8755, 1520-0442. doi: 10.1175/JCLI-D-13-00099.1.

Paulo Ceppi and Jonathan M. Gregory. Relationship of tropospheric stability to climate sensitivity and Earth's observed radiation budget. *Proceedings of the National Academy of Sciences*, 114(50): 13126–13131, December 2017. ISSN 0027-8424, 1091-6490. doi: 10.1073/pnas.1714308114.

Paulo Ceppi and Jonathan M. Gregory. A refined model for the Earth's global energy balance. *Climate Dynamics*, 53(7):4781–4797, October 2019. ISSN 1432-0894. doi: 10.1007/s00382-019-04825-x.

Paulo Ceppi and Dennis L. Hartmann. Connections Between Clouds, Radiation, and Midlatitude Dynamics: A Review. *Current Climate Change Reports*, 1(2):undefined–undefined, 2015. ISSN 21986061. doi: 10.1007/s40641-015-0010-x.

Paulo Ceppi and Dennis L. Hartmann. Clouds and the Atmospheric Circulation Response to Warming. *Journal of Climate*, 29(2):783–799, January 2016. ISSN 0894-8755. doi: 10.1175/JCLI-D-15-0394.1.

Paulo Ceppi and Theodore G. Shepherd. Contributions of Climate Feedbacks to Changes in Atmospheric Circulation. *Journal of Climate*, 30(22):9097–9118, November 2017. ISSN 0894-8755, 1520-0442. doi: 10.1175/JCLI-D-17-0189.1.

Paulo Ceppi, Florent Brient, Mark D. Zelinka, and Dennis L. Hartmann. Cloud feedback mechanisms and their representation in global climate models. *WIREs Climate Change*, 8(4):e465, 2017. ISSN 1757-7799. doi: 10.1002/wcc.465.

Robin Chadwick, Duncan Ackerley, Tomoo Ogura, and Dietmar Dommenget. Separating the Influences of Land Warming, the Direct CO2 Effect, the Plant Physiological Effect, and SST Warming on Regional Precipitation Changes. *Journal of Geophysical Research: Atmospheres*, 124(2):624–640, 2019. ISSN 2169-8996. doi: 10.1029/2018JD029423.

Jule G. Charney, Akio Arakawa, D. James Baker, Bert Bolin, Robert E. Dickinson, Richard M. Goody, Cecil E. Leith, Henry M. Stommel, and Carl I. Wunsch. Carbon Dioxide and Climate: A Scientific Assessment. page 20, 1979.

Gang Chen, Isaac M. Held, and Walter A. Robinson. Sensitivity of the Latitude of the Surface Westerlies to Surface Friction. *Journal of the Atmospheric Sciences*, 64(8):2899–2915, August 2007. ISSN 0022-4928. doi: 10.1175/JAS3995.1.

Gang Chen, Pengfei Zhang, and Jian Lu. Sensitivity of the Latitude of the Westerly Jet Stream to Climate Forcing. *Geophysical Research Letters*, 47(4):e2019GL086563, 2020. ISSN 1944-8007. doi: 10.1029/2019GL086563.

Eui-Seok Chung, Axel Timmermann, Brian J. Soden, Kyung-Ja Ha, Lei Shi, and Viju O. John. Reconciling opposing Walker circulation trends in observations and model projections. *Nature Climate Change*, 9(5):405–412, May 2019. ISSN 1758-6798. doi: 10.1038/s41558-019-0446-4.

Amy C. Clement, Richard Seager, Mark A. Cane, and Stephen E. Zebiak. An Ocean Dynamical Thermostat. *Journal of Climate*, 9(9):2190–2196, September 1996. ISSN 0894-8755, 1520-0442. doi: 10.1175/1520-0442(1996)009<2190:AODT>2.0.CO;2.

S. Coats and K. B. Karnauskas. Are Simulated and Observed Twentieth Century Tropical Pacific Sea Surface Temperature Trends Significant Relative to Internal Variability? *Geophysical Research Letters*, 44(19):9928–9937, 2017. ISSN 1944-8007. doi: 10.1002/2017GL074622.

R. A. Colman and B. J. McAvaney. On tropospheric adjustment to forcing and climate feedbacks. *Climate Dynamics*, 36(9-10):1649–1658, May 2011. ISSN 0930-7575, 1432-0894. doi: 10.1007/s00382-011-1067-4.

Robert Colman and Brian J. Soden. Water vapor and lapse rate feedbacks in the climate system. *Reviews of Modern Physics*, 93(4):045002, November 2021. doi: 10.1103/RevModPhys.93.045002.

Peter M. Cox, Chris Huntingford, and Mark S. Williamson. Emergent constraint on equilibrium climate sensitivity from global temperature variability. *Nature*, 553(7688):319–322, January 2018. ISSN 1476-4687. doi: 10.1038/nature25450.

Julia A. Crook, Piers M. Forster, and Nicola Stuber. Spatial Patterns of Modeled Climate Feedback and Contributions to Temperature Response and Polar Amplification. *Journal of Climate*, 24(14):3575–3592, July 2011. ISSN 0894-8755. doi: 10.1175/2011JCLI3863.1.

Luke Lynden Benjamin Davis. *Connections between Climate Sensitivity and Large-Scale Extratropical Dynamics*. Thesis, 2019.

Nicholas A. Davis and Thomas Birner. Eddy Influences on the Hadley Circulation. *Journal of Advances in Modeling Earth Systems*, 11(6):1563–1581, 2019. ISSN 1942-2466. doi: 10.1029/2018MS001554.

Nicholas A. Davis and Thomas Birner. Eddy-Mediated Hadley Cell Expansion due to Axisymmetric Angular Momentum Adjustment to Greenhouse Gas Forcings. *Journal of the Atmospheric Sciences*, 79(1):141–159, January 2022. ISSN 0022-4928, 1520-0469. doi: 10.1175/JAS-D-20-0149.1.

D. P. Dee, S. M. Uppala, A. J. Simmons, P. Berrisford, P. Poli, S. Kobayashi, U. Andrae, M. A. Balmaseda, G. Balsamo, P. Bauer, P. Bechtold, A. C. M. Beljaars, L. van de Berg, J. Bidlot, N. Bormann, C. Delsol, R. Dragani, M. Fuentes, A. J. Geer, L. Haimberger, S. B. Healy, H. Hersbach, E. V. Hólm, L. Isaksen, P. Kållberg, M. Köhler, M. Matricardi, A. P. McNally, B. M. Monge-Sanz, J.-J. Morcrette, B.-K. Park, C. Peubey, P. de Rosnay, C. Tavolato, J.-N. Thépaut, and F. Vitart. The ERA-Interim reanalysis: Configuration and performance of the data assimilation system. *Quarterly Journal of the Royal Meteorological Society*, 137(656):553–597, 2011. ISSN 1477-870X. doi: 10.1002/qj.828.

Andrew E. Dessler. Potential Problems Measuring Climate Sensitivity from the Historical Record. *Journal of Climate*, 33(6):2237–2248, March 2020. ISSN 0894-8755, 1520-0442. doi: 10.1175/JCLI-D-19-0476.1.

E. Di Lorenzo, G. Liguori, N. Schneider, J. C. Furtado, B. T. Anderson, and M. A. Alexander. ENSO and meridional modes: A null hypothesis for Pacific climate variability. *Geophysical Research Letters*, 42(21):9440–9448, 2015. ISSN 1944-8007. doi: 10.1002/2015GL066281.

Yue Dong, Cristian Proistosescu, Kyle C. Armour, and David S. Battisti. Attributing Historical and Future Evolution of Radiative Feedbacks to Regional Warming Patterns using a Green's Function Approach: The Preeminence of the Western Pacific. *Journal of Climate*, 32(17):5471–5491, September 2019. ISSN 0894-8755, 1520-0442. doi: 10.1175/JCLI-D-18-0843.1.

Yue Dong, Kyle C. Armour, Mark D. Zelinka, Cristian Proistosescu, David S. Battisti, Chen Zhou, and Timothy Andrews. Intermodel Spread in the Pattern Effect and Its Contribution to Climate Sensitivity in CMIP5 and CMIP6 Models. *Journal of Climate*, 33(18):7755–7775, September 2020. ISSN 0894-8755. doi: 10.1175/JCLI-D-19-1011.1.

Yue Dong, Kyle C. Armour, Cristian Proistosescu, Timothy Andrews, David S. Battisti, Piers M. Forster, David Paynter, Christopher J. Smith, and Hideo Shiogama. Biased Estimates of Equilibrium Climate Sensitivity and Transient Climate Response Derived From Historical CMIP6 Simulations. *Geophysical Research Letters*, 48(24):e2021GL095778, 2021. ISSN 1944-8007. doi: 10.1029/2021GL095778.

Yue Dong, Kyle C. Armour, David S. Battisti, and Edward Blanchard-Wrigglesworth. Two-Way Teleconnections between the Southern Ocean and the Tropical Pacific via a Dynamic Feedback. *Journal of Climate*, 35(19):2667–2682, September 2022. ISSN 0894-8755, 1520-0442. doi: 10.1175/JCLI-D-22-0080.1.

Aaron Donohoe, Kyle C. Armour, Angeline G. Pendergrass, and David S. Battisti. Shortwave and longwave radiative contributions to global warming under increasing CO_2. *Proceedings of the National Academy of Sciences*, 111(47):16700–16705, November 2014. ISSN 0027-8424, 1091-6490. doi: 10.1073/pnas.1412190111.

Jean-Louis Dufresne and Sandrine Bony. An Assessment of the Primary Sources of Spread of Global Warming Estimates from Coupled Atmosphere–Ocean Models. *Journal of Climate*, 21 (19):5135–5144, October 2008. ISSN 0894-8755. doi: 10.1175/2008JCLI2239.1.

A. Eliassen. On the transfer of energy in stationary mountain waves. *Geophy. Publ.*, 22:1–23, 1960.

Veronika Eyring, Sandrine Bony, Gerald A. Meehl, Catherine A. Senior, Bjorn Stevens, Ronald J. Stouffer, and Karl E. Taylor. Overview of the Coupled Model Intercomparison Project Phase 6

(CMIP6) experimental design and organization. *Geoscientific Model Development*, 9(5):1937–1958, May 2016. ISSN 1991-959X. doi: 10.5194/gmd-9-1937-2016.

John T. Fasullo and Kevin E. Trenberth. A Less Cloudy Future: The Role of Subtropical Subsidence in Climate Sensitivity. *Science*, 338(6108):792–794, November 2012. doi: 10.1126/science.1227465.

N. Feldl and G. H. Roe. Four perspectives on climate feedbacks. *Geophysical Research Letters*, 40(15):4007–4011, 2013a. ISSN 1944-8007. doi: 10.1002/grl.50711.

Nicole Feldl and Gerard H. Roe. The Nonlinear and Nonlocal Nature of Climate Feedbacks. *Journal of Climate*, 26(21):8289–8304, November 2013b. ISSN 0894-8755. doi: 10.1175/JCLI-D-12-00631.1.

Nicole Feldl, Simona Bordoni, and Timothy M. Merlis. Coupled High-Latitude Climate Feedbacks and Their Impact on Atmospheric Heat Transport. *Journal of Climate*, 30(1):189–201, January 2017. ISSN 0894-8755, 1520-0442. doi: 10.1175/JCLI-D-16-0324.1.

Sonya L. Fiddes, Alain Protat, Marc D. Mallet, Simon P. Alexander, and Matthew T. Woodhouse. Southern Ocean cloud and shortwave radiation biases in a nudged climate model simulation: Does the model ever get it right? *Atmospheric Chemistry and Physics*, 22(22):14603–14630, November 2022. ISSN 1680-7316. doi: 10.5194/acp-22-14603-2022.

Joseph Fourier. Mémoire sur les températures du globe terrestre et des espaces planétaires. *Mémoires de l'Académie Royale des Sciences de l'Institut de France*, 7:570–604, 1827.

Dargan M. W. Frierson, Isaac M. Held, and Pablo Zurita-Gotor. A Gray-Radiation Aquaplanet Moist GCM. Part I: Static Stability and Eddy Scale. *Journal of the Atmospheric Sciences*, 63(10):2548–2566, October 2006. ISSN 0022-4928. doi: 10.1175/JAS3753.1.

Dargan M. W. Frierson, Isaac M. Held, and Pablo Zurita-Gotor. A Gray-Radiation Aquaplanet Moist GCM. Part II: Energy Transports in Altered Climates. *Journal of the Atmospheric Sciences*, 64(5):1680–1693, May 2007. ISSN 0022-4928. doi: 10.1175/JAS3913.1.

S. Fueglistaler. Observational Evidence for Two Modes of Coupling Between Sea Surface Temperatures, Tropospheric Temperature Profile, and Shortwave Cloud Radiative Effect in the Tropics. *Geophysical Research Letters*, 46(16):9890–9898, 2019. ISSN 1944-8007. doi: 10.1029/2019GL083990.

S. Fueglistaler and L.g. Silvers. The Peculiar Trajectory of Global Warming. *Journal of Geophysical Research: Atmospheres*, 126(4):e2020JD033629, 2021. ISSN 2169-8996. doi: 10.1029/2020JD033629.

O. Geoffroy, D. Saint-Martin, G. Bellon, A. Voldoire, D. J. L. Olivié, and S. Tytéca. Transient Climate Response in a Two-Layer Energy-Balance Model. Part II: Representation of the Efficacy of Deep-Ocean Heat Uptake and Validation for CMIP5 AOGCMs. *Journal of Climate*, 26(6): 1859–1876, March 2013a. ISSN 0894-8755, 1520-0442. doi: 10.1175/JCLI-D-12-00196.1.

O. Geoffroy, D. Saint-Martin, D. J. L. Olivié, A. Voldoire, G. Bellon, and S. Tytéca. Transient Climate Response in a Two-Layer Energy-Balance Model. Part I: Analytical Solution and Parameter Calibration Using CMIP5 AOGCM Experiments. *Journal of Climate*, 26(6):1841–1857, March 2013b. ISSN 0894-8755. doi: 10.1175/JCLI-D-12-00195.1.

Ada Gjermundsen, Aleksi Nummelin, Dirk Olivié, Mats Bentsen, Øyvind Seland, and Michael Schulz. Shutdown of Southern Ocean convection controls long-term greenhouse gas-induced warming. *Nature Geoscience*, 14(10):724–731, October 2021. ISSN 1752-0894, 1752-0908. doi: 10.1038/s41561-021-00825-x.

J. M. Gregory and T. Andrews. Variation in climate sensitivity and feedback parameters during the historical period. *Geophysical Research Letters*, 43(8):3911–3920, 2016. ISSN 1944-8007. doi: 10.1002/2016GL068406.

J. M. Gregory, W. J. Ingram, M. A. Palmer, G. S. Jones, P. A. Stott, R. B. Thorpe, J. A. Lowe, T. C. Johns, and K. D. Williams. A new method for diagnosing radiative forcing and climate

sensitivity. *Geophysical Research Letters*, 31(3), February 2004. ISSN 1944-8007. doi: 10.1029/2003GL018747.

J. M. Gregory, T. Andrews, P. Ceppi, T. Mauritsen, and M. J. Webb. How accurately can the climate sensitivity to $$\hbox {CO}_{2}$$CO2be estimated from historical climate change? *Climate Dynamics*, October 2019. ISSN 1432-0894. doi: 10.1007/s00382-019-04991-y.

Jonathan Gregory and Mark Webb. Tropospheric Adjustment Induces a Cloud Component in CO2 Forcing. *Journal of Climate*, 21(1):58–71, January 2008. ISSN 0894-8755. doi: 10.1175/2007JCLI1834.1.

Kevin M. Grise and Mitchell K. Kelleher. Midlatitude Cloud Radiative Effect Sensitivity to Cloud Controlling Factors in Observations and Models: Relationship with Southern Hemisphere Jet Shifts and Climate Sensitivity. *Journal of Climate*, -1(aop):1–59, April 2021. ISSN 0894-8755, 1520-0442. doi: 10.1175/JCLI-D-20-0986.1.

Kevin M. Grise and Lorenzo M. Polvani. Is climate sensitivity related to dynamical sensitivity? A Southern Hemisphere perspective. *Geophysical Research Letters*, 41(2):534–540, 2014. ISSN 1944-8007. doi: 10.1002/2013GL058466.

Kevin M. Grise and Lorenzo M. Polvani. Is climate sensitivity related to dynamical sensitivity? *Journal of Geophysical Research: Atmospheres*, 121(10):5159–5176, 2016. ISSN 2169-8996. doi: 10.1002/2015JD024687.

Kevin M. Grise, Brian Medeiros, James J. Benedict, and Jerry G. Olson. Investigating the Influence of Cloud Radiative Effects on the Extratropical Storm Tracks. *Geophysical Research Letters*, 46 (13):7700–7707, 2019. ISSN 1944-8007. doi: 10.1029/2019GL083542.

Alex Hall and Xin Qu. Using the current seasonal cycle to constrain snow albedo feedback in future climate change. *Geophysical Research Letters*, 33(3), 2006. ISSN 1944-8007. doi: 10.1029/2005GL025127.

Alex Hall, Peter Cox, Chris Huntingford, and Stephen Klein. Progressing emergent constraints on future climate change. *Nature Climate Change*, 9(4):269–278, April 2019. ISSN 1758-6798. doi: 10.1038/s41558-019-0436-6.

Michael S. Halpert and Chester F. Ropelewski. Surface Temperature Patterns Associated with the Southern Oscillation. *Journal of Climate*, 5(6):577–593, 1992. ISSN 0894-8755.

Moritz Hanke, René Redler, Teresa Holfeld, and Maxim Yastremsky. YAC 1.2.0: New aspects for coupling software in Earth system modelling. *Geoscientific Model Development*, 9(8):2755–2769, August 2016. ISSN 1991-959X. doi: 10.5194/gmd-9-2755-2016.

J. Hansen, G. Russell, A. Lacis, I. Fung, D. Rind, and P. Stone. Climate Response Times: Dependence on Climate Sensitivity and Ocean Mixing. *Science*, 229(4716):857–859, 1985. ISSN 0036-8075.

J. Hansen, M. Sato, and R. Ruedy. Radiative forcing and climate response. *Journal of Geophysical Research: Atmospheres*, 102(D6):6831–6864, 1997. ISSN 2156-2202. doi: 10.1029/96JD03436.

Dennis L. Hartmann. *Global Physical Climatology*. Elsevier Science, 2 edition, December 2015. ISBN 978-0-08-091862-4.

Dennis L. Hartmann. The Antarctic ozone hole and the pattern effect on climate sensitivity. *Proceedings of the National Academy of Sciences*, 119(35):e2207889119, August 2022. doi: 10.1073/pnas.2207889119.

Dennis L. Hartmann and Kristin Larson. An important constraint on tropical cloud - climate feedback. *Geophysical Research Letters*, 29(20):1951, October 2002. ISSN 1944-8007. doi: 10.1029/2002GL015835.

K. Hasselmann. Stochastic climate models Part I. Theory. *Tellus*, 28(6):473–485, January 1976. ISSN 0040-2826. doi: 10.3402/tellusa.v28i6.11316.

A. D. Haugstad, K. C. Armour, D. S. Battisti, and B. E. J. Rose. Relative roles of surface temperature and climate forcing patterns in the inconstancy of radiative feedbacks. *Geophysical Research Letters*, 44(14):7455–7463, 2017. ISSN 1944-8007. doi: 10.1002/2017GL074372.

Haozhe He, Ryan J. Kramer, and Brian J. Soden. Evaluating Observational Constraints on Intermodel Spread in Cloud, Temperature, and Humidity Feedbacks. *Geophysical Research Letters*, 48 (17):e2020GL092309, 2021. ISSN 1944-8007. doi: 10.1029/2020GL092309.

Jie He and Brian J. Soden. Anthropogenic Weakening of the Tropical Circulation: The Relative Roles of Direct CO2 Forcing and Sea Surface Temperature Change. *Journal of Climate*, 28(22): 8728–8742, November 2015. ISSN 0894-8755, 1520-0442. doi: 10.1175/JCLI-D-15-0205.1.

Christopher Hedemann, Thorsten Mauritsen, Johann Jungclaus, and Jochem Marotzke. Reconciling Conflicting Accounts of Local Radiative Feedbacks in Climate Models. *Journal of Climate*, 35(10):3131–3146, May 2022. ISSN 0894-8755, 1520-0442. doi: 10.1175/JCLI-D-21-0513.1.

Ulla K. Heede and Alexey V. Fedorov. Eastern equatorial Pacific warming delayed by aerosols and thermostat response to CO2 increase. *Nature Climate Change*, 11(8):696–703, August 2021. ISSN 1758-6798. doi: 10.1038/s41558-021-01101-x.

Ulla K. Heede and Alexey V. Fedorov. Colder Eastern Equatorial Pacific and Stronger Walker Circulation in the Early 21st Century: Separating the Forced Response to Global Warming From Natural Variability. *Geophysical Research Letters*, 50(3):e2022GL101020, 2023. ISSN 1944-8007. doi: 10.1029/2022GL101020.

Ulla K. Heede, Alexey V. Fedorov, and Natalie J. Burls. Time Scales and Mechanisms for the Tropical Pacific Response to Global Warming: A Tug of War between the Ocean Thermostat and Weaker Walker. *Journal of Climate*, 33(14):6101–6118, July 2020. ISSN 0894-8755, 1520-0442. doi: 10.1175/JCLI-D-19-0690.1.

Ulla K. Heede, Alexey V. Fedorov, and Natalie J. Burls. A stronger versus weaker Walker: Understanding model differences in fast and slow tropical Pacific responses to global warm-

ing. *Climate Dynamics*, 57(9):2505–2522, November 2021. ISSN 1432-0894. doi: 10.1007/s00382-021-05818-5.

Isaac M. Held. Large-Scale Dynamics and Global Warming. *Bulletin of the American Meteorological Society*, 74(2):228–242, February 1993. ISSN 0003-0007. doi: 10.1175/1520-0477(1993)074<0228:LSDAGW>2.0.CO;2.

Isaac M. Held. The macroturbulence of the troposphere. *Tellus A*, 51(1):59–70, January 1999. ISSN 1600-0870. doi: 10.1034/j.1600-0870.1999.t01-1-00006.x.

Isaac M. Held. The Gap between Simulation and Understanding in Climate Modeling. *Bulletin of the American Meteorological Society*, 86(11):1609–1614, November 2005. ISSN 0003-0007. doi: 10.1175/BAMS-86-11-1609.

Isaac M. Held and Karen M. Shell. Using Relative Humidity as a State Variable in Climate Feedback Analysis. *Journal of Climate*, 25(8):2578–2582, April 2012. ISSN 0894-8755, 1520-0442. doi: 10.1175/JCLI-D-11-00721.1.

Isaac M. Held and Brian J. Soden. Water Vapor Feedback and Global Warming. *Annual Review of Energy and the Environment*, 25(1):441–475, November 2000. ISSN 1056-3466. doi: 10.1146/annurev.energy.25.1.441.

Isaac M. Held and Brian J. Soden. Robust Responses of the Hydrological Cycle to Global Warming. *Journal of Climate*, 19(21):5686–5699, November 2006. ISSN 0894-8755. doi: 10.1175/JCLI3990.1.

Isaac M. Held and Max J. Suarez. A Proposal for the Intercomparison of the Dynamical Cores of Atmospheric General Circulation Models. *Bulletin of the American Meteorological Society*, 75(10):1825–1830, October 1994. ISSN 0003-0007. doi: 10.1175/1520-0477(1994)075<1825:APFTIO>2.0.CO;2.

Isaac M. Held, Michael Winton, Ken Takahashi, Thomas Delworth, Fanrong Zeng, and Geoffrey K. Vallis. Probing the Fast and Slow Components of Global Warming by Returning Abruptly

to Preindustrial Forcing. *Journal of Climate*, 23(9):2418–2427, May 2010. ISSN 0894-8755, 1520-0442. doi: 10.1175/2009JCLI3466.1.

Matthew Henry and Timothy M. Merlis. The Role of the Nonlinearity of the Stefan–Boltzmann Law on the Structure of Radiatively Forced Temperature Change. *Journal of Climate*, 32(2):335–348, January 2019. ISSN 0894-8755, 1520-0442. doi: 10.1175/JCLI-D-17-0603.1.

M. M. Holland and C. M. Bitz. Polar amplification of climate change in coupled models. *Climate Dynamics*, 21(3):221–232, September 2003. ISSN 1432-0894. doi: 10.1007/s00382-003-0332-6.

Brian J. Hoskins and Paul J. Valdes. On the Existence of Storm-Tracks. *Journal of the Atmospheric Sciences*, 47(15):1854–1864, August 1989. ISSN 0022-4928. doi: 10.1175/1520-0469(1990)047<1854:OTEOST>2.0.CO;2.

Brian J. Hoskins, Ian N. James, and Glenn H. White. The Shape, Propagation and Mean-Flow Interaction of Large-Scale Weather Systems. *Journal of the Atmospheric Sciences*, 40(7):1595–1612, July 1983. ISSN 0022-4928. doi: 10.1175/1520-0469(1983)040<1595:TSPAMF>2.0.CO;2.

Yi Huang and Minghong Zhang. The implication of radiative forcing and feedback for meridional energy transport. *Geophysical Research Letters*, 41(5):1665–1672, 2014. ISSN 1944-8007. doi: 10.1002/2013GL059079.

Yi Huang, Xiaoxiao Tan, and Yan Xia. Inhomogeneous radiative forcing of homogeneous greenhouse gases. *Journal of Geophysical Research: Atmospheres*, 121(6):2780–2789, 2016. ISSN 2169-8996. doi: 10.1002/2015JD024569.

Yi Huang, Yan Xia, and Xiaoxiao Tan. On the pattern of CO2 radiative forcing and poleward energy transport. *Journal of Geophysical Research: Atmospheres*, 122(20):10,578–10,593, 2017. ISSN 2169-8996. doi: 10.1002/2017JD027221.

Yen-Ting Hwang and Dargan M. W. Frierson. Increasing atmospheric poleward energy transport with global warming. *Geophysical Research Letters*, 37(24), 2010. ISSN 1944-8007. doi: 10.1029/2010GL045440.

Yen-Ting Hwang, Dargan M. W. Frierson, and Jennifer E. Kay. Coupling between Arctic feedbacks and changes in poleward energy transport. *Geophysical Research Letters*, 38(17), 2011. ISSN 1944-8007. doi: 10.1029/2011GL048546.

Yen-Ting Hwang, Shang-Ping Xie, Clara Deser, and Sarah M. Kang. Connecting tropical climate change with Southern Ocean heat uptake. *Geophysical Research Letters*, 44(18):9449–9457, 2017. ISSN 1944-8007. doi: 10.1002/2017GL074972.

William Ingram. A new way of quantifying GCM water vapour feedback. *Climate Dynamics*, 40 (3):913–924, February 2013. ISSN 1432-0894. doi: 10.1007/s00382-012-1294-3.

Nadir Jeevanjee and Stephan Fueglistaler. On the Cooling-to-Space Approximation. *Journal of the Atmospheric Sciences*, 77(2):465–478, February 2020a. ISSN 0022-4928, 1520-0469. doi: 10.1175/JAS-D-18-0352.1.

Nadir Jeevanjee and Stephan Fueglistaler. Simple Spectral Models for Atmospheric Radiative Cooling. *Journal of the Atmospheric Sciences*, 77(2):479–497, February 2020b. ISSN 0022-4928, 1520-0469. doi: 10.1175/JAS-D-18-0347.1.

Nadir Jeevanjee, Pedram Hassanzadeh, Spencer Hill, and Aditi Sheshadri. A perspective on climate model hierarchies. *Journal of Advances in Modeling Earth Systems*, 9(4):1760–1771, August 2017. ISSN 1942-2466. doi: 10.1002/2017MS001038.

Nadir Jeevanjee, Daniel D. B. Koll, and Nicholas Lutsko. "Simpson's Law" and the Spectral Cancellation of Climate Feedbacks. *Geophysical Research Letters*, 48(14):e2021GL093699, 2021a. ISSN 1944-8007. doi: 10.1029/2021GL093699.

Nadir Jeevanjee, Jacob T. Seeley, David Paynter, and Stephan Fueglistaler. An Analytical Model for Spatially Varying Clear-Sky CO2 Forcing. *Journal of Climate*, 34(23):9463–9480, December 2021b. ISSN 0894-8755, 1520-0442. doi: 10.1175/JCLI-D-19-0756.1.

Jules B. Kajtar, Agus Santoso, Matthew Collins, Andréa S. Taschetto, Matthew H. England, and Leela M. Frankcombe. CMIP5 Intermodel Relationships in the Baseline Southern Ocean Climate

System and With Future Projections. *Earth's Future*, 9(6), June 2021. ISSN 2328-4277, 2328-4277. doi: 10.1029/2020EF001873.

Youichi Kamae, Tomoo Ogura, Hideo Shiogama, and Masahiro Watanabe. Recent progress toward reducing the uncertainty in tropical low cloud feedback and climate sensitivity: A review. *Geoscience Letters*, 3(1):17, June 2016. ISSN 2196-4092. doi: 10.1186/s40562-016-0053-4.

Sarah M. Kang and Shang-Ping Xie. Dependence of Climate Response on Meridional Structure of External Thermal Forcing. *Journal of Climate*, 27(14):5593–5600, July 2014. ISSN 0894-8755, 1520-0442. doi: 10.1175/JCLI-D-13-00622.1.

Sarah M. Kang, Matt Hawcroft, Baoqiang Xiang, Yen-Ting Hwang, Gabriel Cazes, Francis Codron, Traute Crueger, Clara Deser, Øivind Hodnebrog, Hanjun Kim, Jiyeong Kim, Yu Kosaka, Teresa Losada, Carlos R. Mechoso, Gunnar Myhre, Øyvind Seland, Bjorn Stevens, Masahiro Watanabe, and Sungduk Yu. Extratropical–Tropical Interaction Model Intercomparison Project (Etin-Mip): Protocol and Initial Results. *Bulletin of the American Meteorological Society*, 100(12): 2589–2606, December 2019. ISSN 0003-0007, 1520-0477. doi: 10.1175/BAMS-D-18-0301.1.

Jennifer E. Kay, Marika M. Holland, Cecilia M. Bitz, Edward Blanchard-Wrigglesworth, Andrew Gettelman, Andrew Conley, and David Bailey. The Influence of Local Feedbacks and Northward Heat Transport on the Equilibrium Arctic Climate Response to Increased Greenhouse Gas Forcing. *Journal of Climate*, 25(16):5433–5450, August 2012. ISSN 0894-8755, 1520-0442. doi: 10.1175/JCLI-D-11-00622.1.

Charles D. Keeling. Is Carbon Dioxide from Fossil Fuel Changing Man's Environment? *Proceedings of the American Philosophical Society*, 114(1):10–17, 1970. ISSN 0003-049X.

Hanjun Kim, Sarah M. Kang, Jennifer E. Kay, and Shang-Ping Xie. Subtropical clouds key to Southern Ocean teleconnections to the tropical Pacific. *Proceedings of the National Academy of Sciences*, 119(34):e2200514119, August 2022. doi: 10.1073/pnas.2200514119.

Stephen A. Klein and Alex Hall. Emergent Constraints for Cloud Feedbacks. *Current Climate Change Reports*, 1(4):276–287, December 2015. ISSN 2198-6061. doi: 10.1007/s40641-015-0027-1.

Stephen A. Klein and Dennis L. Hartmann. The Seasonal Cycle of Low Stratiform Clouds. *Journal of Climate*, 6(8):1587–1606, August 1993. ISSN 0894-8755, 1520-0442. doi: 10.1175/1520-0442(1993)006<1587:TSCOLS>2.0.CO;2.

Reto Knutti. The end of model democracy? *Climatic Change*, 102(3):395–404, October 2010. ISSN 1573-1480. doi: 10.1007/s10584-010-9800-2.

Reto Knutti and Maria A. A. Rugenstein. Feedbacks, climate sensitivity and the limits of linear models. *Philosophical Transactions of the Royal Society A: Mathematical, Physical and Engineering Sciences*, 373(2054):20150146, November 2015. doi: 10.1098/rsta.2015.0146.

Reto Knutti, Reinhard Furrer, Claudia Tebaldi, Jan Cermak, and Gerald A. Meehl. Challenges in Combining Projections from Multiple Climate Models. *Journal of Climate*, 23(10):2739–2758, May 2010. ISSN 0894-8755, 1520-0442. doi: 10.1175/2009JCLI3361.1.

Reto Knutti, Maria A. A. Rugenstein, and Gabriele C. Hegerl. Beyond equilibrium climate sensitivity. *Nature Geoscience*, 10(10):727–736, October 2017. ISSN 1752-0908. doi: 10.1038/ngeo3017.

A. Kolly and Y. Huang. The Radiative Feedback During the ENSO Cycle: Observations Versus Models. *Journal of Geophysical Research: Atmospheres*, 123(17):9097–9108, 2018. ISSN 2169-8996. doi: 10.1029/2018JD028401.

Ryan J. Kramer, Alexander V. Matus, Brian J. Soden, and Tristan S. L'Ecuyer. Observation-Based Radiative Kernels From CloudSat/CALIPSO. *Journal of Geophysical Research: Atmospheres*, 124(10):5431–5444, 2019. ISSN 2169-8996. doi: 10.1029/2018JD029021.

R. Kubo. The fluctuation-dissipation theorem. *Reports on Progress in Physics*, 29(1):255, January 1966. ISSN 0034-4885. doi: 10.1088/0034-4885/29/1/306.

Peter Kuma. Climate model code genealogy and its relation to climate feedbacks and sensitivity, 2023.

Paul J. Kushner and Lorenzo M. Polvani. Stratosphere–Troposphere Coupling in a Relatively Simple AGCM: The Role of Eddies. *Journal of Climate*, 17(3):629–639, February 2004. ISSN 0894-8755. doi: 10.1175/1520-0442(2004)017<0629:SCIARS>2.0.CO;2.

Paul J. Kushner and Lorenzo M. Polvani. Stratosphere–Troposphere Coupling in a Relatively Simple AGCM: Impact of the Seasonal Cycle. *Journal of Climate*, 19(21):5721–5727, November 2006. ISSN 0894-8755. doi: 10.1175/JCLI4007.1.

Andrew A. Lacis, Gavin A. Schmidt, David Rind, and Reto A. Ruedy. Atmospheric CO2: Principal Control Knob Governing Earth's Temperature. *Science*, 330(6002):356–359, October 2010. doi: 10.1126/science.1190653.

F. Hugo Lambert and Patrick C. Taylor. Regional variation of the tropical water vapor and lapse rate feedbacks. *Geophysical Research Letters*, 41(21):7634–7641, 2014. ISSN 1944-8007. doi: 10.1002/2014GL061987.

Martin Leduc, René Laprise, Ramón de Elía, and Leo Šeparović. Is Institutional Democracy a Good Proxy for Model Independence? *Journal of Climate*, 29(23):8301–8316, December 2016. ISSN 0894-8755, 1520-0442. doi: 10.1175/JCLI-D-15-0761.1.

Sukyoung Lee, Michelle L'Heureux, Andrew T. Wittenberg, Richard Seager, Paul A. O'Gorman, and Nathaniel C. Johnson. On the future zonal contrasts of equatorial Pacific climate: Perspectives from Observations, Simulations, and Theories. *npj Climate and Atmospheric Science*, 5(1):1–15, October 2022. ISSN 2397-3722. doi: 10.1038/s41612-022-00301-2.

C. E. Leith. Climate Response and Fluctuation Dissipation. *Journal of the Atmospheric Sciences*, 32(10):2022–2026, October 1975. ISSN 0022-4928. doi: 10.1175/1520-0469(1975)032<2022:CRAFD>2.0.CO;2.

Nathan J. L. Lenssen, Gavin A. Schmidt, James E. Hansen, Matthew J. Menne, Avraham Persin, Reto Ruedy, and Daniel Zyss. Improvements in the GISTEMP Uncertainty Model. *Journal of Geophysical Research: Atmospheres*, 124(12):6307–6326, 2019. ISSN 2169-8996. doi: 10.1029/2018JD029522.

Ying Li, David W. J. Thompson, Sandrine Bony, and Timothy M. Merlis. Thermodynamic Control on the Poleward Shift of the Extratropical Jet in Climate Change Simulations: The Role of Rising High Clouds and Their Radiative Effects. *Journal of Climate*, 32(3):917–934, February 2019. ISSN 0894-8755. doi: 10.1175/JCLI-D-18-0417.1.

Ying Li, David W. J. Thompson, and Dirk Olonscheck. A Basic Effect of Cloud Radiative Effects on Tropical Sea Surface Temperature Variability. *Journal of Climate*, 33(10):4333–4346, May 2020. ISSN 0894-8755. doi: 10.1175/JCLI-D-19-0298.1.

Fukai Liu, Jian Lu, Oluwayemi Garuba, L. Ruby Leung, Yiyong Luo, and Xiuquan Wan. Sensitivity of Surface Temperature to Oceanic Forcing via q-Flux Green's Function Experiments. Part I: Linear Response Function. *Journal of Climate*, 31(9):3625–3641, May 2018a. ISSN 0894-8755, 1520-0442. doi: 10.1175/JCLI-D-17-0462.1.

Fukai Liu, Jian Lu, Oluwayemi A. Garuba, Yi Huang, L. Ruby Leung, Bryce E. Harrop, and Yiyong Luo. Sensitivity of Surface Temperature to Oceanic Forcing via q-Flux Green's Function Experiments. Part II: Feedback Decomposition and Polar Amplification. *Journal of Climate*, 31(17):6745–6761, September 2018b. ISSN 0894-8755, 1520-0442. doi: 10.1175/JCLI-D-18-0042.1.

Jingjing Liu, Jun Tian, Zhonghui Liu, Timothy D. Herbert, Alexey V. Fedorov, and Mitch Lyle. Eastern equatorial Pacific cold tongue evolution since the late Miocene linked to extratropical climate. *Science Advances*, 5(4):eaau6060, April 2019. doi: 10.1126/sciadv.aau6060.

Norman G. Loeb, David R. Doelling, Hailan Wang, Wenying Su, Cathy Nguyen, Joseph G. Corbett, Lusheng Liang, Cristian Mitrescu, Fred G. Rose, and Seiji Kato. Clouds and the Earth's

Radiant Energy System (CERES) Energy Balanced and Filled (EBAF) Top-of-Atmosphere (TOA) Edition-4.0 Data Product. *Journal of Climate*, 31(2):895–918, January 2018. ISSN 0894-8755, 1520-0442. doi: 10.1175/JCLI-D-17-0208.1.

David J. Lorenz and Dennis L. Hartmann. Eddy–Zonal Flow Feedback in the Southern Hemisphere. *Journal of the Atmospheric Sciences*, 58(21):3312–3327, November 2001. ISSN 0022-4928. doi: 10.1175/1520-0469(2001)058<3312:EZFFIT>2.0.CO;2.

David J. Lorenz and Dennis L. Hartmann. Eddy–Zonal Flow Feedback in the Northern Hemisphere Winter. *Journal of Climate*, 16(8):1212–1227, April 2003. ISSN 0894-8755. doi: 10.1175/1520-0442(2003)16<1212:EFFITN>2.0.CO;2.

Edward N. Lorenz. Available Potential Energy and the Maintenance of the General Circulation. *Tellus*, 7(2):157–167, May 1955. ISSN 2153-3490. doi: 10.1111/j.2153-3490.1955.tb01148.x.

Jian Lu, Gang Chen, and Dargan M. W. Frierson. Response of the Zonal Mean Atmospheric Circulation to El Niño versus Global Warming. *Journal of Climate*, 21(22):5835–5851, November 2008. ISSN 0894-8755. doi: 10.1175/2008JCLI2200.1.

Jian Lu, Gang Chen, and Dargan M. W. Frierson. The Position of the Midlatitude Storm Track and Eddy-Driven Westerlies in Aquaplanet AGCMs. *Journal of the Atmospheric Sciences*, 67(12):3984–4000, September 2010. ISSN 0022-4928. doi: 10.1175/2010JAS3477.1.

Jian Lu, Lantao Sun, Yutian Wu, and Gang Chen. The Role of Subtropical Irreversible PV Mixing in the Zonal Mean Circulation Response to Global Warming–Like Thermal Forcing. *Journal of Climate*, 27(6):2297–2316, March 2014. ISSN 0894-8755. doi: 10.1175/JCLI-D-13-00372.1.

Kezhou Lu, Jie He, Boniface Fosu, and Maria Rugenstein. Mechanisms of Fast Walker Circulation Responses to CO2 Forcing. *Geophysical Research Letters*, 48(23):e2021GL095708, 2021. ISSN 1944-8007. doi: 10.1029/2021GL095708.

Matthew T. Luongo, Shang-Ping Xie, Ian Eisenman, Yen-Ting Hwang, and Hung-Yi Tseng. A Pathway for Northern Hemisphere Extratropical Cooling to Elicit a Tropical Response. *Geophysical Research Letters*, 50(2):e2022GL100719, 2023. ISSN 1944-8007. doi: 10.1029/2022GL100719.

Nicholas J. Lutsko. The Relationship Between Cloud Radiative Effect and Surface Temperature Variability at El Niño-Southern Oscillation Frequencies in CMIP5 Models. *Geophysical Research Letters*, 45(19):10,599–10,608, 2018. ISSN 1944-8007. doi: 10.1029/2018GL079236.

Nicholas J. Lutsko and Ken Takahashi. What Can the Internal Variability of CMIP5 Models Tell Us about Their Climate Sensitivity? *Journal of Climate*, 31(13):5051–5069, April 2018. ISSN 0894-8755. doi: 10.1175/JCLI-D-17-0736.1.

Nicholas J. Lutsko, Max Popp, Robert H. Nazarian, and Anna Lea Albright. Emergent Constraints on Regional Cloud Feedbacks. *Geophysical Research Letters*, 48(10), May 2021. ISSN 0094-8276, 1944-8007. doi: 10.1029/2021GL092934.

Nicholas J. Lutsko, Matthew T. Luongo, Casey J. Wall, and Timothy A. Myers. Correlation Between Cloud Adjustments and Cloud Feedbacks Responsible for Larger Range of Climate Sensitivities in CMIP6. *Journal of Geophysical Research: Atmospheres*, 127(23):e2022JD037486, 2022. ISSN 2169-8996. doi: 10.1029/2022JD037486.

Anna Mackie and Michael Byrne. Effects of circulation on tropical cloud feedbacks in high-resolution simulations. 2022. doi: 10.1002/essoar.10509780.1.

Penelope Maher, Edwin P. Gerber, Brian Medeiros, Timothy M. Merlis, Steven Sherwood, Aditi Sheshadri, Adam H. Sobel, Geoffrey K. Vallis, Aiko Voigt, and Pablo Zurita-Gotor. Model Hierarchies for Understanding Atmospheric Circulation. *Reviews of Geophysics*, 57(2):250–280, 2019. ISSN 1944-9208. doi: 10.1029/2018RG000607.

Syukuro Manabe and Richard T. Wetherald. Thermal Equilibrium of the Atmosphere with a Given Distribution of Relative Humidity. *Journal of the Atmospheric Sciences*, 24(3):241–259, May 1967. ISSN 0022-4928. doi: 10.1175/1520-0469(1967)024<0241:TEOTAW>2.0.CO;2.

Syukuro Manabe and Richard T. Wetherald. The Effects of Doubling the CO2 Concentration on the climate of a General Circulation Model. *Journal of the Atmospheric Sciences*, 32(1):3–15, January 1975. ISSN 0022-4928. doi: 10.1175/1520-0469(1975)032<0003:TEODTC>2.0.CO;2.

Kate Marvel, Robert Pincus, Gavin A. Schmidt, and Ron L. Miller. Internal Variability and Disequilibrium Confound Estimates of Climate Sensitivity From Observations. *Geophysical Research Letters*, 45(3):1595–1601, 2018. ISSN 1944-8007. doi: 10.1002/2017GL076468.

D. Masson and R. Knutti. Climate model genealogy. *Geophysical Research Letters*, 38(8), 2011. ISSN 1944-8007. doi: 10.1029/2011GL046864.

V. Masson-Delmotte, P. Zhai, A. Pirani, S.L. Connors, C. Péan, S. Berger, N. Caud, Y. Chen, L. Goldfarb, M.I. Gomis, M. Huang, K. Leitzell, E. Lonnoy, J.B.R. Matthews, T.K. Maycock, T. Waterfield, O. Yelekçi, R. Yu, and B. Zhou, editors. *Climate Change 2021: The Physical Science Basis. Contribution of Working Group I to the Sixth Assessment Report of the Intergovernmental Panel on Climate Change*. Cambridge University Press, Cambridge, United Kingdom and New York, NY, USA, 2021.

Cheikh Mbengue and Tapio Schneider. Storm Track Shifts under Climate Change: What Can Be Learned from Large-Scale Dry Dynamics. *Journal of Climate*, 26(24):9923–9930, October 2013. ISSN 0894-8755. doi: 10.1175/JCLI-D-13-00404.1.

Daniel T. McCoy, Dennis L. Hartmann, Mark D. Zelinka, Paulo Ceppi, and Daniel P. Grosvenor. Mixed-phase cloud physics and Southern Ocean cloud feedback in climate models. *Journal of Geophysical Research: Atmospheres*, 120(18):9539–9554, 2015. ISSN 2169-8996. doi: 10.1002/2015JD023603.

Daniel T. McCoy, Paul Field, Alejandro Bodas-Salcedo, Gregory S. Elsaesser, and Mark D. Zelinka. A Regime-Oriented Approach to Observationally Constraining Extratropical Shortwave Cloud Feedbacks. *Journal of Climate*, 33(23):9967–9983, December 2020. ISSN 0894-8755, 1520-0442. doi: 10.1175/JCLI-D-19-0987.1.

Brett A. McKim, Nadir Jeevanjee, and Geoffrey K. Vallis. Joint Dependence of Longwave Feedback on Surface Temperature and Relative Humidity. *Geophysical Research Letters*, 48(18): e2021GL094074, 2021. ISSN 1944-8007. doi: 10.1029/2021GL094074.

J. D. McLean, C. R. de Freitas, and R. M. Carter. Influence of the Southern Oscillation on tropospheric temperature. *Journal of Geophysical Research: Atmospheres*, 114(D14), 2009. ISSN 2156-2202. doi: 10.1029/2008JD011637.

Brian Medeiros, Bjorn Stevens, and Sandrine Bony. Using aquaplanets to understand the robust responses of comprehensive climate models to forcing. *Climate Dynamics*, 44(7):1957–1977, April 2015. ISSN 1432-0894. doi: 10.1007/s00382-014-2138-0.

Katharina Meraner, Thorsten Mauritsen, and Aiko Voigt. Robust increase in equilibrium climate sensitivity under global warming. *Geophysical Research Letters*, 40(22):5944–5948, 2013. ISSN 1944-8007. doi: 10.1002/2013GL058118.

Timothy M. Merlis and Tapio Schneider. Changes in Zonal Surface Temperature Gradients and Walker Circulations in a Wide Range of Climates. *Journal of Climate*, 24(17):4757–4768, September 2011. ISSN 0894-8755, 1520-0442. doi: 10.1175/2011JCLI4042.1.

Eleanor A. Middlemas, Amy C. Clement, Brian Medeiros, and Ben Kirtman. Cloud Radiative Feedbacks and El Niño–Southern Oscillation. *Journal of Climate*, 32(15):4661–4680, August 2019. ISSN 0894-8755, 1520-0442. doi: 10.1175/JCLI-D-18-0842.1.

Joy Merwin Monteiro, Jeremy McGibbon, and Rodrigo Caballero. Sympl (v. 0.4.0) and climt (v. 0.15.3) – towards a flexible framework for building model hierarchies in Python. *Geo-*

scientific Model Development, 11(9):3781–3794, September 2018. ISSN 1991-959X. doi: 10.5194/gmd-11-3781-2018.

F. B. Mudge. The development of the 'greenhouse' theory of global climate change from Victorian times. *Weather*, 52(1):13–17, 1997. ISSN 1477-8696. doi: 10.1002/j.1477-8696.1997.tb06243.x.

James M. Murphy, David M. H. Sexton, David N. Barnett, Gareth S. Jones, Mark J. Webb, Matthew Collins, and David A. Stainforth. Quantification of modelling uncertainties in a large ensemble of climate change simulations. *Nature*, 430(7001):768–772, August 2004. ISSN 1476-4687. doi: 10.1038/nature02771.

Benjamin J. Murray, Kenneth S. Carslaw, and Paul R. Field. Opinion: Cloud-phase climate feedback and the importance of ice-nucleating particles. *Atmospheric Chemistry and Physics*, 21(2): 665–679, January 2021. ISSN 1680-7316. doi: 10.5194/acp-21-665-2021.

Timothy A. Myers and Joel R. Norris. On the Relationships between Subtropical Clouds and Meteorology in Observations and CMIP3 and CMIP5 Models. *Journal of Climate*, 28(8):2945–2967, April 2015. ISSN 0894-8755, 1520-0442. doi: 10.1175/JCLI-D-14-00475.1.

Timothy A. Myers, Ryan C. Scott, Mark D. Zelinka, Stephen A. Klein, Joel R. Norris, and Peter M. Caldwell. Observational constraints on low cloud feedback reduce uncertainty of climate sensitivity. *Nature Climate Change*, pages 1–7, May 2021. ISSN 1758-6798. doi: 10.1038/s41558-021-01039-0.

Femke J. M. M. Nijsse, Peter M. Cox, and Mark S. Williamson. Emergent constraints on transient climate response (TCR) and equilibrium climate sensitivity (ECS) from historical warming in CMIP5 and CMIP6 models. *Earth System Dynamics*, 11(3):737–750, August 2020. ISSN 2190-4979. doi: 10.5194/esd-11-737-2020.

Gerald R. North, Robert F. Cahalan, and James A. Coakley. Energy balance climate models. *Reviews of Geophysics*, 19(1):91–121, February 1981. ISSN 1944-9208. doi: 10.1029/RG019i001p00091.

P. A. O'Gorman and C. J. Muller. How closely do changes in surface and column water vapor follow Clausius–Clapeyron scaling in climate change simulations? *Environmental Research Letters*, 5(2):025207, April 2010. ISSN 1748-9326. doi: 10.1088/1748-9326/5/2/025207.

Paul A. O'Gorman and Tapio Schneider. The Hydrological Cycle over a Wide Range of Climates Simulated with an Idealized GCM. *Journal of Climate*, 21(15):3815–3832, August 2008. ISSN 0894-8755, 1520-0442. doi: 10.1175/2007JCLI2065.1.

Dirk Olonscheck and Maria Rugenstein. Coupled climate models systematically underestimate radiation response to surface warming, 2023.

Dirk Olonscheck, Maria Rugenstein, and Jochem Marotzke. Broad Consistency Between Observed and Simulated Trends in Sea Surface Temperature Patterns. *Geophysical Research Letters*, 47(10): e2019GL086773, 2020. ISSN 1944-8007. doi: 10.1029/2019GL086773.

Tim Palmer and Bjorn Stevens. The scientific challenge of understanding and estimating climate change. *Proceedings of the National Academy of Sciences of the United States of America*, 116 (49):34390–34395, 2019. ISSN 10916490. doi: 10.1073/pnas.1906691116.

Sungsu Park and Conway B. Leovy. Marine Low-Cloud Anomalies Associated with ENSO. *Journal of Climate*, 17(17):3448–3469, September 2004. ISSN 0894-8755, 1520-0442. doi: 10.1175/1520-0442(2004)017<3448:MLAAWE>2.0.CO;2.

D. Paynter and T. L. Frölicher. Sensitivity of radiative forcing, ocean heat uptake, and climate feedback to changes in anthropogenic greenhouse gases and aerosols. *Journal of Geophysical Research: Atmospheres*, 120(19):9837–9854, 2015. ISSN 2169-8996. doi: 10.1002/2015JD023364.

A. G. Pendergrass. The Global-Mean Precipitation Response to CO2-Induced Warming in CMIP6 Models. *Geophysical Research Letters*, 47(17):e2020GL089964, 2020. ISSN 1944-8007. doi: 10.1029/2020GL089964.

Angeline G. Pendergrass and Dennis L. Hartmann. The Atmospheric Energy Constraint on Global-Mean Precipitation Change. *Journal of Climate*, 27(2):757–768, January 2014. ISSN 0894-8755. doi: 10.1175/JCLI-D-13-00163.1.

Christopher Pennell and Thomas Reichler. On the Effective Number of Climate Models. *Journal of Climate*, 24(9):2358–2367, May 2011. ISSN 0894-8755, 1520-0442. doi: 10.1175/2010JCLI3814.1.

Grant William Petty. *A First Course in Atmospheric Radiation*. Sundog Pub., 2006. ISBN 978-0-9729033-1-8.

Felix Pithan and Thorsten Mauritsen. Arctic amplification dominated by temperature feedbacks in contemporary climate models. *Nature Geoscience*, 7(3):181–184, March 2014. ISSN 1752-0908. doi: 10.1038/ngeo2071.

Stephen Po-Chedley, Kyle C. Armour, Cecilia M. Bitz, Mark D. Zelinka, Benjamin D. Santer, and Qiang Fu. Sources of Intermodel Spread in the Lapse Rate and Water Vapor Feedbacks. *Journal of Climate*, 31(8):3187–3206, April 2018. ISSN 0894-8755, 1520-0442. doi: 10.1175/JCLI-D-17-0674.1.

Claude Servais Mathias Pouillet. Mémoire sur la chaleur solaire, sur les pouvoirs rayonnants et absorbants de l'air atmosphérique, et sur la température de l'espace. *Comptes Rendus des Séances de l'Academie des Sciences*, 7:24–64, 1838.

Xin Qu, Alex Hall, Anthony M. DeAngelis, Mark D. Zelinka, Stephen A. Klein, Hui Su, Baijun Tian, and Chengxing Zhai. On the Emergent Constraints of Climate Sensitivity. *Journal of Climate*, 31(2):863–875, January 2018. ISSN 0894-8755. doi: 10.1175/JCLI-D-17-0482.1.

Gaby Rädel, Thorsten Mauritsen, Bjorn Stevens, Dietmar Dommenget, Daniela Matei, Katinka Bellomo, and Amy Clement. Amplification of El Niño by cloud longwave coupling to atmospheric circulation. *Nature Geoscience*, 9(2):106–110, February 2016. ISSN 1752-0908. doi: 10.1038/ngeo2630.

Eugene M. Rasmusson and Thomas H. Carpenter. Variations in Tropical Sea Surface Temperature and Surface Wind Fields Associated with the Southern Oscillation/El Niño. *Monthly Weather Review*, 110(5):354–384, May 1982. ISSN 1520-0493, 0027-0644. doi: 10.1175/1520-0493(1982)110<0354:VITSST>2.0.CO;2.

Thomas Reichler, Martin Dameris, and Robert Sausen. Determining the tropopause height from gridded data. *Geophysical Research Letters*, 30(20):n/a–n/a, October 2003. ISSN 00948276. doi: 10.1029/2003GL018240.

Roger Revelle and Hans E. Suess. Carbon Dioxide Exchange Between Atmosphere and Ocean and the Question of an Increase of Atmospheric CO2 during the Past Decades. *Tellus*, 9(1):18–27, January 1957. ISSN 0040-2826. doi: 10.3402/tellusa.v9i1.9075.

T. B. Richardson, P. M. Forster, C. J. Smith, A. C. Maycock, T. Wood, T. Andrews, O. Boucher, G. Faluvegi, D. Fläschner, Ø. Hodnebrog, M. Kasoar, A. Kirkevåg, J.-F. Lamarque, J. Mülmenstädt, G. Myhre, D. Olivié, R. W. Portmann, B. H. Samset, D. Shawki, D. Shindell, P. Stier, T. Takemura, A. Voulgarakis, and D. Watson-Parris. Efficacy of Climate Forcings in PDRMIP Models. *Journal of Geophysical Research: Atmospheres*, 124(23):12824–12844, 2019. ISSN 2169-8996. doi: 10.1029/2019JD030581.

Walter A. Robinson. A Baroclinic Mechanism for the Eddy Feedback on the Zonal Index. *Journal of the Atmospheric Sciences*, 57(3):415–422, February 2000. ISSN 0022-4928. doi: 10.1175/1520-0469(2000)057<0415:ABMFTE>2.0.CO;2.

Gerard Roe. Feedbacks, Timescales, and Seeing Red. *Annual Review of Earth and Planetary Sciences*, 37(1):93–115, May 2009. ISSN 0084-6597, 1545-4495. doi: 10.1146/annurev.earth.061008.134734.

Gerard H. Roe and Marcia B. Baker. Why Is Climate Sensitivity So Unpredictable? *Science*, 318 (5850):629–632, October 2007. ISSN 0036-8075, 1095-9203. doi: 10.1126/science.1144735.

Tim Rohrschneider, Bjorn Stevens, and Thorsten Mauritsen. On simple representations of the climate response to external radiative forcing. *Climate Dynamics*, 53(5):3131–3145, September 2019. ISSN 1432-0894. doi: 10.1007/s00382-019-04686-4.

Brian E. J. Rose. CLIMLAB: A Python toolkit for interactive, process-oriented climate modeling. *Journal of Open Source Software*, 3(24):659, April 2018. ISSN 2475-9066. doi: 10.21105/joss.00659.

Brian E. J. Rose and M. Cameron Rencurrel. The Vertical Structure of Tropospheric Water Vapor: Comparing Radiative and Ocean-Driven Climate Changes. *Journal of Climate*, 29(11):4251–4268, June 2016. ISSN 0894-8755, 1520-0442. doi: 10.1175/JCLI-D-15-0482.1.

Brian E. J. Rose, Kyle C. Armour, David S. Battisti, Nicole Feldl, and Daniel D. B. Koll. The dependence of transient climate sensitivity and radiative feedbacks on the spatial pattern of ocean heat uptake. *Geophysical Research Letters*, 41(3):1071–1078, 2014. ISSN 1944-8007. doi: 10.1002/2013GL058955.

Maria Rugenstein, Jonah Bloch-Johnson, Jonathan Gregory, Timothy Andrews, Thorsten Mauritsen, Chao Li, Thomas L. Frölicher, David Paynter, Gokhan Danabasoglu, Shuting Yang, Jean-Louis Dufresne, Long Cao, Gavin A. Schmidt, Ayako Abe-Ouchi, Olivier Geoffroy, and Reto Knutti. Equilibrium Climate Sensitivity Estimated by Equilibrating Climate Models. *Geophysical Research Letters*, 47(4):e2019GL083898, 2020. ISSN 1944-8007. doi: 10.1029/2019GL083898.

Maria A. A. Rugenstein and Kyle C. Armour. Three Flavors of Radiative Feedbacks and Their Implications for Estimating Equilibrium Climate Sensitivity. *Geophysical Research Letters*, 48 (15):e2021GL092983, 2021. ISSN 1944-8007. doi: 10.1029/2021GL092983.

Maria A. A. Rugenstein, Ken Caldeira, and Reto Knutti. Dependence of global radiative feedbacks on evolving patterns of surface heat fluxes. *Geophysical Research Letters*, 43(18):9877–9885, 2016a. ISSN 1944-8007. doi: 10.1002/2016GL070907.

Maria A. A. Rugenstein, Jonathan M. Gregory, Nathalie Schaller, Jan Sedláček, and Reto Knutti. Multiannual Ocean–Atmosphere Adjustments to Radiative Forcing. *Journal of Climate*, 29(15): 5643–5659, August 2016b. ISSN 0894-8755. doi: 10.1175/JCLI-D-16-0312.1.

Rick D. Russotto and Michela Biasutti. Polar Amplification as an Inherent Response of a Circulating Atmosphere: Results From the TRACMIP Aquaplanets. *Geophysical Research Letters*, 47 (6):e2019GL086771, 2020. ISSN 1944-8007. doi: 10.1029/2019GL086771.

J. S. Sawyer. Man-made Carbon Dioxide and the "Greenhouse" Effect. *Nature*, 239(5366):23–26, September 1972. ISSN 1476-4687. doi: 10.1038/239023a0.

Kathleen A. Schiro, Hui Su, Fiaz Ahmed, Ni Dai, Clare E. Singer, Pierre Gentine, Gregory S. Elsaesser, Jonathan H. Jiang, Yong-Sang Choi, and J. David Neelin. Model spread in tropical low cloud feedback tied to overturning circulation response to warming. *Nature Communications*, 13 (1):7119, November 2022. ISSN 2041-1723. doi: 10.1038/s41467-022-34787-4.

Stephen H. Schneider and Robert E. Dickinson. Climate modeling. *Reviews of Geophysics*, 12(3): 447–493, 1974. ISSN 1944-9208. doi: 10.1029/RG012i003p00447.

Tapio Schneider. The Tropopause and the Thermal Stratification in the Extratropics of a Dry Atmosphere. *Journal of the Atmospheric Sciences*, 61(12):1317–1340, June 2004. ISSN 0022-4928. doi: 10.1175/1520-0469(2004)061<1317:TTATTS>2.0.CO;2.

Tapio Schneider and Christopher C. Walker. Self-Organization of Atmospheric Macroturbulence into Critical States of Weak Nonlinear Eddy–Eddy Interactions. *Journal of the Atmospheric Sciences*, 63(6):1569–1586, June 2006. ISSN 0022-4928. doi: 10.1175/JAS3699.1.

Tapio Schneider, Paul A. O'Gorman, and Xavier J. Levine. Water Vapor and the Dynamics of Climate Changes. *Reviews of Geophysics*, 48(3), 2010. ISSN 1944-9208. doi: 10.1029/2009RG000302.

Tapio Schneider, Tobias Bischoff, and Gerald H. Haug. Migrations and dynamics of the intertropical convergence zone. *Nature*, 513(7516):45–53, September 2014. ISSN 0028-0836, 1476-4687. doi: 10.1038/nature13636.

A. J. Schuddeboom and A. J. McDonald. The Southern Ocean Radiative Bias, Cloud Compensating Errors, and Equilibrium Climate Sensitivity in CMIP6 Models. *Journal of Geophysical Research: Atmospheres*, 126(22):e2021JD035310, 2021. ISSN 2169-8996. doi: 10.1029/2021JD035310.

Ryan C. Scott, Timothy A. Myers, Joel R. Norris, Mark D. Zelinka, Stephen A. Klein, Moguo Sun, and David R. Doelling. Observed Sensitivity of Low-Cloud Radiative Effects to Meteorological Perturbations over the Global Oceans. *Journal of Climate*, 33(18):7717–7734, September 2020. ISSN 0894-8755, 1520-0442. doi: 10.1175/JCLI-D-19-1028.1.

Richard Seager, Nili Harnik, Yochanan Kushnir, Walter Robinson, and Jennifer Miller. Mechanisms of Hemispherically Symmetric Climate Variability. *Journal of Climate*, 16(18):2960–2978, September 2003. ISSN 0894-8755, 1520-0442. doi: 10.1175/1520-0442(2003)016<2960:MOHSCV>2.0.CO;2.

Richard Seager, Mark Cane, Naomi Henderson, Dong-Eun Lee, Ryan Abernathey, and Honghai Zhang. Strengthening tropical Pacific zonal sea surface temperature gradient consistent with rising greenhouse gases. *Nature Climate Change*, 9(7):517–522, July 2019. ISSN 1758-6798. doi: 10.1038/s41558-019-0505-x.

Jacob T. Seeley and Nadir Jeevanjee. H2O Windows and CO2 Radiator Fins: A Clear-Sky Explanation for the Peak in Equilibrium Climate Sensitivity. *Geophysical Research Letters*, 48(4):e2020GL089609, 2021. ISSN 1944-8007. doi: 10.1029/2020GL089609.

William D. Sellers. A Global Climatic Model Based on the Energy Balance of the Earth-Atmosphere System. *Journal of Applied Meteorology and Climatology*, 8(3):392–400, June 1969. ISSN 1520-0450. doi: 10.1175/1520-0450(1969)008<0392:AGCMBO>2.0.CO;2.

Catherine A. Senior and John F. B. Mitchell. The time-dependence of climate sensitivity. *Geophysical Research Letters*, 27(17):2685–2688, 2000. ISSN 1944-8007. doi: 10.1029/2000GL011373.

T. A. Shaw and A. Voigt. Tug of war on summertime circulation between radiative forcing and sea surface warming. *Nature Geoscience*, 8(7):560–566, July 2015. ISSN 1752-0908. doi: 10.1038/ngeo2449.

T. A. Shaw, M. Baldwin, E. A. Barnes, R. Caballero, C. I. Garfinkel, Y.-T. Hwang, C. Li, P. A. O'Gorman, G. Rivière, I. R. Simpson, and A. Voigt. Storm track processes and the opposing influences of climate change. *Nature Geoscience*, 9(9):656–664, September 2016. ISSN 1752-0908. doi: 10.1038/ngeo2783.

Tiffany A. Shaw. Mechanisms of Future Predicted Changes in the Zonal Mean Mid-Latitude Circulation. *Current Climate Change Reports*, 5(4):345–357, December 2019. ISSN 2198-6061. doi: 10.1007/s40641-019-00145-8.

Tiffany A. Shaw and Zhihong Tan. Testing Latitudinally Dependent Explanations of the Circulation Response to Increased CO2 Using Aquaplanet Models. *Geophysical Research Letters*, 45 (18):9861–9869, 2018. ISSN 1944-8007. doi: 10.1029/2018GL078974.

Tiffany A. Shaw and Aiko Voigt. What can moist thermodynamics tell us about circulation shifts in response to uniform warming? *Geophysical Research Letters*, 43(9):4566–4575, May 2016. ISSN 1944-8007. doi: 10.1002/2016GL068712.

Tiffany A. Shaw, Pragallva Barpanda, and Aaron Donohoe. A Moist Static Energy Framework for Zonal-Mean Storm-Track Intensity. *Journal of the Atmospheric Sciences*, 75(6):1979–1994, March 2018. ISSN 0022-4928. doi: 10.1175/JAS-D-17-0183.1.

Karen M. Shell, Jeffrey T. Kiehl, and Christine A. Shields. Using the Radiative Kernel Technique to Calculate Climate Feedbacks in NCAR's Community Atmospheric Model. *Journal of Climate*, 21(10):2269–2282, May 2008. ISSN 0894-8755. doi: 10.1175/2007JCLI2044.1.

S. Sherwood, M. J. Webb, J. D. Annan, K. C. Armour, P. M. Forster, J. C. Hargreaves, G. Hegerl, S. A. Klein, K. D. Marvel, E. J. Rohling, M. Watanabe, T. Andrews, P. Braconnot, C. S. Bretherton, G. L. Foster, Z. Hausfather, A. S. von der Heydt, R. Knutti, T. Mauritsen, J. R. Norris, C. Proistosescu, M. Rugenstein, G. A. Schmidt, K. B. Tokarska, and M. D. Zelinka. An assessment of Earth's climate sensitivity using multiple lines of evidence. *Reviews of Geophysics*, n/a(n/a): e2019RG000678, July 2020. ISSN 1944-9208. doi: 10.1029/2019RG000678.

Steven C. Sherwood, William Ingram, Yoko Tsushima, Masaki Satoh, Malcolm Roberts, Pier Luigi Vidale, and Paul A. O'Gorman. Relative humidity changes in a warmer climate. *Journal of Geophysical Research: Atmospheres*, 115(D9), 2010. ISSN 2156-2202. doi: 10.1029/2009JD012585.

Steven C. Sherwood, Sandrine Bony, Olivier Boucher, Chris Bretherton, Piers M. Forster, Jonathan M. Gregory, and Bjorn Stevens. Adjustments in the Forcing-Feedback Framework for Understanding Climate Change. *Bulletin of the American Meteorological Society*, 96(2):217–228, February 2015. ISSN 0003-0007. doi: 10.1175/BAMS-D-13-00167.1.

C. J. Smith, G. R. Harris, M. D. Palmer, N. Bellouin, W. Collins, G. Myhre, M. Schulz, J.-C. Golaz, M. Ringer, T. Storelvmo, and P. M. Forster. Energy Budget Constraints on the Time History of Aerosol Forcing and Climate Sensitivity. *Journal of Geophysical Research: Atmospheres*, 126 (13):e2020JD033622, 2021. ISSN 2169-8996. doi: 10.1029/2020JD033622.

Christopher J. Smith, Ryan J. Kramer, Gunnar Myhre, Kari Alterskjær, William Collins, Adriana Sima, Olivier Boucher, Jean-Louis Dufresne, Pierre Nabat, Martine Michou, Seiji Yukimoto, Jason Cole, David Paynter, Hideo Shiogama, Fiona M. O'Connor, Eddy Robertson, Andy Wiltshire, Timothy Andrews, Cécile Hannay, Ron Miller, Larissa Nazarenko, Alf Kirkevåg, Dirk Olivié, Stephanie Fiedler, Anna Lewinschal, Chloe Mackallah, Martin Dix, Robert Pincus, and Piers M. Forster. Effective radiative forcing and adjustments in CMIP6 models. *Atmospheric Chemistry and Physics*, 20(16):9591–9618, August 2020. ISSN 1680-7316. doi: 10.5194/acp-20-9591-2020.

Brian J. Soden and Isaac M. Held. An Assessment of Climate Feedbacks in Coupled Ocean–Atmosphere Models. *Journal of Climate*, 19(14):3354–3360, July 2006. ISSN 0894-8755. doi: 10.1175/JCLI3799.1.

Brian J. Soden, Isaac M. Held, Robert Colman, Karen M. Shell, Jeffrey T. Kiehl, and Christine A. Shields. Quantifying Climate Feedbacks Using Radiative Kernels. *Journal of Climate*, 21(14): 3504–3520, July 2008. ISSN 0894-8755. doi: 10.1175/2007JCLI2110.1.

Graeme L. Stephens. Cloud Feedbacks in the Climate System: A Critical Review. *Journal of Climate*, 18(2):237–273, January 2005. ISSN 0894-8755, 1520-0442. doi: 10.1175/JCLI-3243.1.

Bjorn Stevens, Steven C. Sherwood, Sandrine Bony, and Mark J. Webb. Prospects for narrowing bounds on Earth's equilibrium climate sensitivity. *Earth's Future*, 4(11):512–522, 2016. ISSN 2328-4277. doi: 10.1002/2016EF000376.

T. F. Stocker, D. Qin, G.-K. Plattner, M. Tignor, S.K. Allen, J. Boschung, A. Nauels, Y. Xia, V. Bex, and P.M. Midgley, editors. *Climate Change 2013: The Physical Science Basis. Contribution of Working Group I to the Fifth Assessment Report of the Intergovernmental Panel on Climate Change*. Cambridge University Press, Cambridge, United Kingdom and New York, NY, USA, 2013. ISBN ISBN 978-1-107-66182-0.

Malte F. Stuecker, Cecilia M. Bitz, Kyle C. Armour, Cristian Proistosescu, Sarah M. Kang, Shang-Ping Xie, Doyeon Kim, Shayne McGregor, Wenjun Zhang, Sen Zhao, Wenju Cai, Yue Dong, and Fei-Fei Jin. Polar amplification dominated by local forcing and feedbacks. *Nature Climate Change*, 8(12):1076–1081, December 2018. ISSN 1758-6798. doi: 10.1038/s41558-018-0339-y.

Lantao Sun, Gang Chen, and Jian Lu. Sensitivities and Mechanisms of the Zonal Mean Atmospheric Circulation Response to Tropical Warming. *Journal of the Atmospheric Sciences*, 70(8): 2487–2504, August 2013. ISSN 0022-4928, 1520-0469. doi: 10.1175/JAS-D-12-0298.1.

Chiharu Takahashi and Masahiro Watanabe. Pacific trade winds accelerated by aerosol forcing over the past two decades. *Nature Climate Change*, 6(8):768–772, August 2016. ISSN 1758-6798. doi: 10.1038/nclimate2996.

Ivy Tan, Trude Storelvmo, and Mark D. Zelinka. Observational constraints on mixed-phase clouds imply higher climate sensitivity. *Science*, 352(6282):224–227, April 2016. doi: 10.1126/science.aad5300.

Karl E. Taylor, Ronald J. Stouffer, and Gerald A. Meehl. An Overview of CMIP5 and the Experiment Design. *Bulletin of the American Meteorological Society*, 93(4):485–498, April 2012. ISSN 0003-0007. doi: 10.1175/BAMS-D-11-00094.1.

Claudia Tebaldi and Reto Knutti. The use of the multi-model ensemble in probabilistic climate projections. *Philosophical Transactions of the Royal Society A: Mathematical, Physical and Engineering Sciences*, 365(1857):2053–2075, August 2007. doi: 10.1098/rsta.2007.2076.

Chad W. Thackeray and Christopher G. Fletcher. Snow albedo feedback: Current knowledge, importance, outstanding issues and future directions. *Progress in Physical Geography: Earth and Environment*, 40(3):392–408, June 2016. ISSN 0309-1333. doi: 10.1177/0309133315620999.

Diana R. Thatcher and Christiane Jablonowski. A moist aquaplanet variant of the Held–Suarez test for atmospheric model dynamical cores. *Geoscientific Model Development*, 9(4):1263–1292, April 2016. ISSN 1991-959X. doi: 10.5194/gmd-9-1263-2016.

David W. J. Thompson and Elizabeth A. Barnes. Periodic Variability in the Large-Scale Southern Hemisphere Atmospheric Circulation. *Science*, 343(6171):641–645, February 2014. ISSN 0036-8075, 1095-9203. doi: 10.1126/science.1247660.

David W. J. Thompson and John M. Wallace. Annular Modes in the Extratropical Circulation. Part I: Month-to-Month Variability. *Journal of Climate*, 13(5):1000–1016, March 2000. ISSN 0894-8755. doi: 10.1175/1520-0442(2000)013<1000:AMITEC>2.0.CO;2.

Jessica E. Tierney, Alan M. Haywood, Ran Feng, Tripti Bhattacharya, and Bette L. Otto-Bliesner. Pliocene Warmth Consistent With Greenhouse Gas Forcing. *Geophysical Research Letters*, 46 (15):9136–9144, 2019. ISSN 1944-8007. doi: 10.1029/2019GL083802.

Jessica E. Tierney, Christopher J. Poulsen, Isabel P. Montañez, Tripti Bhattacharya, Ran Feng, Heather L. Ford, Bärbel Hönisch, Gordon N. Inglis, Sierra V. Petersen, Navjit Sagoo, Clay R. Tabor, Kaustubh Thirumalai, Jiang Zhu, Natalie J. Burls, Gavin L. Foster, Yves Goddéris, Brian T. Huber, Linda C. Ivany, Sandra Kirtland Turner, Daniel J. Lunt, Jennifer C. McElwain, Benjamin J. W. Mills, Bette L. Otto-Bliesner, Andy Ridgwell, and Yi Ge Zhang. Past climates inform our future. *Science*, 370(6517), November 2020. ISSN 0036-8075, 1095-9203. doi: 10.1126/science.aay3701.

Katarzyna B. Tokarska, Gabriele C. Hegerl, Andrew P. Schurer, Piers M. Forster, and Kate Marvel. Observational constraints on the effective climate sensitivity from the historical period. *Environmental Research Letters*, 15(3):034043, March 2020a. ISSN 1748-9326. doi: 10.1088/1748-9326/ab738f.

Katarzyna B. Tokarska, Martin B. Stolpe, Sebastian Sippel, Erich M. Fischer, Christopher J. Smith, Flavio Lehner, and Reto Knutti. Past warming trend constrains future warming in CMIP6 models. *Science Advances*, 6(12):eaaz9549, 2020b. doi: 10.1126/sciadv.aaz9549.

Kevin E. Trenberth and John T. Fasullo. Global warming due to increasing absorbed solar radiation. *Geophysical Research Letters*, 36(7), 2009. ISSN 1944-8007. doi: 10.1029/2009GL037527.

Kevin E. Trenberth, Julie M. Caron, David P. Stepaniak, and Steve Worley. Evolution of El Niño–Southern Oscillation and global atmospheric surface temperatures. *Journal of Geophysical Research: Atmospheres*, 107(D8):AAC 5–1–AAC 5–17, 2002. ISSN 2156-2202. doi: 10.1029/2000JD000298.

Kevin E. Trenberth, John T. Fasullo, Chris O'Dell, and Takmeng Wong. Relationships between tropical sea surface temperature and top-of-atmosphere radiation. *Geophysical Research Letters*, 37(3), 2010. ISSN 1944-8007. doi: 10.1029/2009GL042314.

John Tyndall. On the absorption and radiation of heat by gases and vapours, and on the physical connexion of radiation, absorption, and conduction. *Philosophical Transactions of the Royal Society of London*, 151:1–36, January 1861. doi: 10.1098/rstl.1861.0001.

Alejandro Uribe, Frida A.-M. Bender, and Thorsten Mauritsen. Observed and CMIP6 modelled internal variability feedbacks and their relation to forced climate feedbacks. *Geophysical Research Letters*, n/a(n/a):e2022GL100075, 2022. ISSN 1944-8007. doi: 10.1029/2022GL100075.

Geoffrey K. Vallis, Greg Colyer, Ruth Geen, Edwin Gerber, Martin Jucker, Penelope Maher, Alexander Paterson, Marianne Pietschnig, James Penn, and Stephen I. Thomson. Isca, v1.0: A framework for the global modelling of the atmospheres of Earth and other planets at varying levels of complexity. *Geoscientific Model Development; Katlenburg-Lindau*, 11(3):843–859, 2018. doi: http://dx.doi.org/10.5194/gmd-11-843-2018.

Gabriel A. Vecchi and Brian J. Soden. Global Warming and the Weakening of the Tropical Circulation. *Journal of Climate*, 20(17):4316–4340, September 2007. ISSN 0894-8755. doi: 10.1175/JCLI4258.1.

Jessica Vial, Jean-Louis Dufresne, and Sandrine Bony. On the interpretation of inter-model spread in CMIP5 climate sensitivity estimates. *Climate Dynamics*, 41(11):3339–3362, December 2013. ISSN 1432-0894. doi: 10.1007/s00382-013-1725-9.

Aiko Voigt, Nicole Albern, Paulo Ceppi, Kevin Grise, Ying Li, and Brian Medeiros. Clouds, radiation, and atmospheric circulation in the present-day climate and under climate change. *WIREs Climate Change*, n/a(n/a):e694, November 2020. ISSN 1757-7799. doi: 10.1002/wcc.694.

Casey J. Wall and Dennis L. Hartmann. On the influence of poleward jet shift on shortwave cloud feedback in global climate models. *Journal of Advances in Modeling Earth Systems*, 7(4):2044–2059, 2015. ISSN 1942-2466. doi: 10.1002/2015MS000520.

Casey J. Wall, Nicholas J. Lutsko, and David N. Vishny. Revisiting Cloud Radiative Heating and the Southern Annular Mode. *Geophysical Research Letters*, 49(19):e2022GL100463, 2022a. ISSN 1944-8007. doi: 10.1029/2022GL100463.

Casey J. Wall, Trude Storelvmo, Joel R. Norris, and Ivy Tan. Observational Constraints on Southern Ocean Cloud-Phase Feedback. *Journal of Climate*, 35(15):5087–5102, August 2022b. ISSN 0894-8755, 1520-0442. doi: 10.1175/JCLI-D-21-0812.1.

Yuwei Wang and Yi Huang. Understanding the Atmospheric Temperature Adjustment to CO2 Perturbation at the Process Level. *Journal of Climate*, 33(3):787–803, December 2019. ISSN 0894-8755, 1520-0442. doi: 10.1175/JCLI-D-19-0032.1.

Masahiro Watanabe, Jean-Louis Dufresne, Yu Kosaka, Thorsten Mauritsen, and Hiroaki Tatebe. Enhanced warming constrained by past trends in equatorial Pacific sea surface temperature gradient. *Nature Climate Change*, 11(1):33–37, January 2021. ISSN 1758-6798. doi: 10.1038/s41558-020-00933-3.

Andrew I. L. Williams, Nadir Jeevanjee, and Jonah Bloch-Johnson. Circus Tents, Convective Thresholds, and the Non-Linear Climate Response to Tropical SSTs. *Geophysical Research Letters*, 50(6):e2022GL101499, 2023. ISSN 1944-8007. doi: 10.1029/2022GL101499.

K. D. Williams, W. J. Ingram, and J. M. Gregory. Time Variation of Effective Climate Sensitivity in GCMs. *Journal of Climate*, 21(19):5076–5090, October 2008. ISSN 0894-8755. doi: 10.1175/2008JCLI2371.1.

David L. Williamson, Michael Blackburn, Kensuke Nakajima, Wataru Ohfuchi, Yoshiyuki O. Takahashi, Yoshi-Yuki Hayashi, Hisashi Nakamura, Masaki Ishiwatari, John L. McGREGOR, Hartmut Borth, Volkmar Wirth, Helmut Frank, Peter Bechtold, Nils P. Wedi, Hirofumi Tomita,

Masaki Satoh, Ming Zhao, Isaac M. Held, Max J. Suarez, Myong-In Lee, Masahiro Watanabe, Masahide Kimoto, Yimin Liu, Zaizhi Wang, Andrea Molod, Kavirajan Rajendran, Akio Kitoh, and Rachel Stratton. The Aqua-Planet Experiment (APE): Response to Changed Meridional SST Profile. *Journal of the Meteorological Society of Japan. Ser. II*, 91A:57–89, 2013. doi: 10.2151/jmsj.2013-A03.

Mark S. Williamson, Chad W. Thackeray, Peter M. Cox, Alex Hall, Chris Huntingford, and Femke J. M. M. Nijsse. Emergent constraints on climate sensitivities. *Reviews of Modern Physics*, 93(2): 025004, May 2021. doi: 10.1103/RevModPhys.93.025004.

Michael Winton, Ken Takahashi, and Isaac M. Held. Importance of Ocean Heat Uptake Efficacy to Transient Climate Change. *Journal of Climate*, 23(9):2333–2344, May 2010. ISSN 0894-8755, 1520-0442. doi: 10.1175/2009JCLI3139.1.

Yan Xia and Yi Huang. Differential Radiative Heating Drives Tropical Atmospheric Circulation Weakening. *Geophysical Research Letters*, 44(20):10,592–10,600, 2017. ISSN 1944-8007. doi: 10.1002/2017GL075678.

Shang-Ping Xie. Westward Propagation of Latitudinal Asymmetry in a Coupled Ocean–Atmosphere Model. *Journal of the Atmospheric Sciences*, 53(22):3236–3250, November 1996. ISSN 0022-4928, 1520-0469. doi: 10.1175/1520-0469(1996)053<3236:WPOLAI>2.0.CO;2.

Shang-Ping. Xie and S. George H. Philander. A coupled ocean-atmosphere model of relevance to the ITCZ in the eastern Pacific. *Tellus A*, 46(4):340–350, 1994. ISSN 1600-0870. doi: 10.1034/j.1600-0870.1994.t01-1-00001.x.

Shang-Ping Xie, Yu Kosaka, and Yuko M. Okumura. Distinct energy budgets for anthropogenic and natural changes during global warming hiatus. *Nature Geoscience*, 9(1):29–33, January 2016. ISSN 1752-0908. doi: 10.1038/ngeo2581.

Haijun Yang and Fuyao Wang. Revisiting the Thermocline Depth in the Equatorial Pacific. *Journal of Climate*, 22(13):3856–3863, July 2009. ISSN 0894-8755, 1520-0442. doi: 10.1175/2009JCLI2836.1.

Mark D. Zelinka and Dennis L. Hartmann. Climate Feedbacks and Their Implications for Poleward Energy Flux Changes in a Warming Climate. *Journal of Climate*, 25(2):608–624, January 2012. ISSN 0894-8755. doi: 10.1175/JCLI-D-11-00096.1.

Mark D. Zelinka, Stephen A. Klein, and Dennis L. Hartmann. Computing and Partitioning Cloud Feedbacks Using Cloud Property Histograms. Part I: Cloud Radiative Kernels. *Journal of Climate*, 25(11):3715–3735, June 2012. ISSN 0894-8755. doi: 10.1175/JCLI-D-11-00248.1.

Mark D. Zelinka, Chen Zhou, and Stephen A. Klein. Insights from a refined decomposition of cloud feedbacks. *Geophysical Research Letters*, 43(17):9259–9269, 2016. ISSN 1944-8007. doi: 10.1002/2016GL069917.

Mark D. Zelinka, Timothy A. Myers, Daniel T. McCoy, Stephen Po-Chedley, Peter M. Caldwell, Paulo Ceppi, Stephen A. Klein, and Karl E. Taylor. Causes of Higher Climate Sensitivity in CMIP6 Models. *Geophysical Research Letters*, 47(1):e2019GL085782, 2020. ISSN 1944-8007. doi: 10.1029/2019GL085782.

Lei Zhang and Tim Li. A Simple Analytical Model for Understanding the Formation of Sea Surface Temperature Patterns under Global Warming. *Journal of Climate*, 27(22):8413–8421, November 2014. ISSN 0894-8755, 1520-0442. doi: 10.1175/JCLI-D-14-00346.1.

Liping Zhang, Thomas L. Delworth, William Cooke, and Xiaosong Yang. Natural variability of Southern Ocean convection as a driver of observed climate trends. *Nature Climate Change*, 9(1):59–65, January 2019. ISSN 1758-6798. doi: 10.1038/s41558-018-0350-3.

Minghong Zhang and Yi Huang. Radiative Forcing of Quadrupling CO2. *Journal of Climate*, 27(7):2496–2508, April 2014. ISSN 0894-8755. doi: 10.1175/JCLI-D-13-00535.1.

Pengfei Zhang, Gang Chen, and Yi Ming. Quantifying the Mechanisms of Atmospheric Circulation Response to Greenhouse Gas Increases in a Forcing–Feedback Framework. *Journal of Climate*, 34 (17):7005–7022, September 2021. ISSN 0894-8755, 1520-0442. doi: 10.1175/JCLI-D-20-0778.1.

Yi Zhang, Nadir Jeevanjee, and Stephan Fueglistaler. Linearity of Outgoing Longwave Radiation: From an Atmospheric Column to Global Climate Models. *Geophysical Research Letters*, 47(17): e2020GL089235, 2020. ISSN 1944-8007. doi: 10.1029/2020GL089235.

Chen Zhou, Mark D. Zelinka, and Stephen A. Klein. Impact of decadal cloud variations on the Earth's energy budget. *Nature Geoscience*, 9(12):871–874, December 2016. ISSN 1752-0908. doi: 10.1038/ngeo2828.

Chen Zhou, Mark D. Zelinka, and Stephen A. Klein. Analyzing the dependence of global cloud feedback on the spatial pattern of sea surface temperature change with a Green's function approach. *Journal of Advances in Modeling Earth Systems*, 9(5):2174–2189, 2017. ISSN 1942-2466. doi: 10.1002/2017MS001096.

Ping Zhu, James J. Hack, Jeffrey T. Kiehl, and Christopher S. Bretherton. Climate sensitivity of tropical and subtropical marine low cloud amount to ENSO and global warming due to doubled CO2. *Journal of Geophysical Research: Atmospheres*, 112(D17), 2007. ISSN 2156-2202. doi: 10.1029/2006JD008174.

Pablo Zurita-Gotor. The Sensitivity of the Isentropic Slope in a Primitive Equation Dry Model. *Journal of the Atmospheric Sciences*, 65(1):43–65, January 2008. ISSN 0022-4928. doi: 10.1175/2007JAS2284.1.

Appendix A

Forcing-feedback metrics

A.1 Global feedback parameters

Chapter 2 establishes the close analogy between the thermal relaxation coefficient τ^{-1} and the local climate feedback parameter λ. Using a procedure similar to *Armour et al.* (2012), we can also average Equation 2.2 to obtain dynamical core-friendly expressions for the "effective" global feedback parameter and global climate sensitivity.

First, suppose we define the full-atmosphere climate sensitivity $\overline{\langle \Delta T \rangle}$ as the temperature response averaged over the entire atmosphere (where the single overbar denotes a horizontal average and the single angle brackets denote a vertical average). An expression for $\overline{\langle \Delta T \rangle}$ can be obtained by taking the horizontal average vertical integral of Equation 2.2 (where the double angle brackets denote a vertical integral):

$$\overline{\left\langle\!\!\left\langle -\frac{C}{\tau}\Delta T \right\rangle\!\!\right\rangle} = \overline{\langle\!\langle \lambda_\tau \Delta T \rangle\!\rangle} = \hat{\lambda}_\tau \, \overline{\langle \Delta T \rangle} = \overline{\langle\!\langle \Delta Q \rangle\!\rangle} = \overline{\langle\!\langle \Delta N \rangle\!\rangle} - \overline{\langle\!\langle H \rangle\!\rangle} \tag{A.1}$$

In the context of the full-atmosphere response, the relaxation feedback parameter $\lambda_\tau \equiv -C/\tau$ represents the *local climate feedback parameter* and the response-weighted average $\hat{\lambda}_\tau \equiv \overline{\langle\!\langle \lambda_\tau \Delta T \rangle\!\rangle} \,/\, \overline{\langle \Delta T \rangle}$ represents the *effective global feedback parameter*. The global average vertical integral of the forcing perturbation H is analogous to the global average of the top-of-atmosphere radiative forcing perturbation from Equation 1.1.

Second, suppose we define the level-i climate sensitivity $\overline{\Delta T}_i$ as the global average temperature response at level i – say, the 1000 hPa pressure level. An expression for $\overline{\Delta T}_i$ can be obtained by regrouping the terms used to define the local feedback parameter in Equation A.1 in an effort to linearize the response around the temperature of level i:

$$\overline{\frac{\langle\!\langle \lambda_\tau \Delta T \rangle\!\rangle}{\Delta T_i} \Delta T_i} = \overline{\lambda_{i\tau} \Delta T_i} = \hat{\lambda}_{i\tau}\, \overline{\Delta T}_i = \overline{\langle\!\langle \Delta Q \rangle\!\rangle} = \overline{\langle\!\langle \Delta N \rangle\!\rangle} - \overline{\langle\!\langle H \rangle\!\rangle} \tag{A.2}$$

In the context of the level-i response, the scaled relaxation feedback parameter $\lambda_{i\tau} \equiv \langle\!\langle \lambda_\tau \Delta T \rangle\!\rangle \,/ \Delta T_i$ represents the *local climate feedback parameter* and the response-weighted average $\hat{\lambda}_{i\tau} \equiv \overline{\lambda_{i\tau} \Delta T_i} \,/\, \overline{\Delta T}_i$ represents the *effective global feedback parameter*. This effective global feedback parameter is similar to $\hat{\lambda}_\tau$ (Equation A.1), except the associated local feedback parameter is weighted by the temperature response from a single level rather than all levels – analogous to a weighting by the surface temperature response ΔT_s.

Equations A.1 and A.2 represent dynamical core-equivalents of a global climate feedback analysis under spatially dependent feedbacks (e.g., *Armour et al.* 2012, *Boer and Yu* 2003a,b, *Dong et al.* 2019, *Feldl and Roe* 2013a, *Zhou et al.* 2017). They express the climate sensitivity in terms of the spatial pattern of the local feedbacks, the spatial pattern of the temperature response, and the global average of the forcing perturbation.

A.2 Radiative feedback kernels

In more complex models, the local climate feedback parameter λ is often broken down into the sum of component feedback parameters. These are the separate radiative responses to changes in air temperature, specific humidity, cloud properties, surface temperature, and surface albedo associated with the full response of the climate system to forcing perturbations (e.g., *Hansen et al.* 1985). Each component feedback parameter can be estimated as the product of a so-called *radiative feedback kernel* and a climate response term (*Soden and Held* 2006, *Soden et al.* 2008). For example, the component feedback parameter λ_T associated with changes in air temperature can be expressed as follows:

$$\lambda_T = \left\langle\!\!\left\langle \frac{\partial R}{\partial T} \frac{\Delta T}{\Delta T_\mathrm{s}} \right\rangle\!\!\right\rangle = \left\langle\!\!\left\langle K_T \frac{\Delta T}{\Delta T_\mathrm{s}} \right\rangle\!\!\right\rangle \tag{A.3}$$

where R is the top-of-atmosphere radiative flux, T is the air temperature, T_s is the surface temperature, and $K_T \equiv \partial R/\partial T$ is the air temperature radiative kernel. A comparison of λ_T from Equation A.3 with $\lambda_{i\tau}$ from Equation A.2 reveals that the relaxation feedback parameter $\lambda_\tau \equiv -C/\tau$ is analogous to the air temperature radiative kernel K_T, with the level-i response ΔT_i standing in for the surface response ΔT_s. This also follows from the analogy between the dynamical core thermal forcing response $\Delta Q = \lambda_\tau \Delta T$ (Equation 2.2) and the top-of-atmosphere radiative response ΔR (Equation 1.1), which itself implies that the partial derivative $\partial Q/\partial T = \lambda_\tau$ is analogous to $\partial R/\partial T = K_T$.

Similar to Equation A.3, if the remaining thermodynamic properties can be expressed as a function of air temperature, then the local feedback parameter λ can be expressed in terms of a net radiative feedback kernel K:

$$\lambda = \left\langle\!\!\left\langle \frac{\mathrm{d}R}{\mathrm{d}T} \frac{\Delta T}{\Delta T_\mathrm{s}} \right\rangle\!\!\right\rangle = \left\langle\!\!\left\langle K \frac{\Delta T}{\Delta T_\mathrm{s}} \right\rangle\!\!\right\rangle \tag{A.4}$$

where $K \equiv \mathrm{d}R/\mathrm{d}T$ is the total derivative of the radiative response with respect to air temperature (i.e., including attendant changes to e.g. moisture). Again comparing λ from Equation A.4 with $\lambda_{i\tau}$ from Equation A.2 and noting the analogy between $\mathrm{d}Q/\mathrm{d}T = \lambda_\tau$ and $\mathrm{d}R/\mathrm{d}T = K_T$ (Equation 2.1), λ_τ also appears to be analogous to the *net* radiative kernel K.

Equation A.4 suggests that a variety of climate feedbacks might be "encoded" in a dynamical core model by appropriately scaling λ_τ. For example, consider the clear-sky radiative response to a forcing perturbation driven by changes to air temperature and specific humidity. If we suppose that specific humidity q always responds to changes in air temperature T according to the Clausius-Clapeyron relation (i.e., the relative humidity is fixed; e.g., *Held and Soden* 2006), then an estimate for the combined temperature-specific humidity feedback parameter can be obtained as follows:

$$\lambda_{T,q} = \left\langle\!\!\left\langle K_T \frac{\Delta T}{\Delta T_\mathrm{s}} + K_q \frac{\Delta q}{\Delta T_\mathrm{s}} \right\rangle\!\!\right\rangle \approx \left\langle\!\!\left\langle K_T \frac{\Delta T}{\Delta T_\mathrm{s}} + K_q \frac{\partial q}{\partial T} \frac{\Delta T}{\Delta T_\mathrm{s}} \right\rangle\!\!\right\rangle = \left\langle\!\!\left\langle K_{T,q} \frac{\Delta T}{\Delta T_\mathrm{s}} \right\rangle\!\!\right\rangle \tag{A.5}$$

where K_T is the temperature radiative kernel, K_q is the specific humidity radiative kernel, $K_{T,q} \equiv K_T + K_q \, \partial q / \partial T$ is the combined temperature-specific humidity radiative kernel, and $\partial q / \partial T$ represents the Clausius-Clapeyron scaling. If the latitude-height structure of the relaxation feedback parameter λ_τ resembles the radiative kernel $K_{T,q}$, the climate feedback due to water vapor might be thought of as "encoded" in the dry model. Figure 2.2 compares the spatial pattern of λ_τ under the HS94 configuration of a dynamical core model against the radiative kernel $K_{T,q}$ estimated from a reanalysis data set.

A.3 Relaxation climate sensitivity

In more complex models, the global feedback parameter associated with changes in air temperature is often broken down into two components: 1) a so-called Planck feedback parameter λ_P, associated with the isothermal component of the full temperature response; and 2) a lapse rate feedback parameter λ_L, associated with deviations from the isothermal response (e.g., *Hartmann* 2015). The climate sensitivity ΔT per unit radiative forcing H associated with the isothermal response is generally called the reference climate sensitivity parameter, equivalent to $s_0 = -1/\lambda_\mathrm{P}$.

In a dynamical core model, s_0 can be obtained analytically by solving Equations A.1 and A.2 for $s_0 = \Delta T \, / \, \overline{\langle\!\langle H \rangle\!\rangle}$ under the assumption of an isothermal response and an energy imbalance of zero (note the same result is obtained using either Equation A.1 or Equation A.2). I call this the *relaxation climate sensitivity parameter* s_τ, defined as follows:

$$\begin{aligned} \hat{\lambda}_\tau \approx \overline{\langle\!\langle \lambda_\tau \rangle\!\rangle} &= -\overline{\left\langle\!\!\left\langle \frac{C}{\tau} \right\rangle\!\!\right\rangle} = -\frac{C_0}{\tau_0} \\ s_\tau = -\frac{1}{\overline{\langle\!\langle \lambda_\tau \rangle\!\rangle}} &= \frac{\tau_0}{C_0} \end{aligned} \tag{A.6}$$

where $\tau_0 \equiv 1/\, \overline{\langle 1/\tau \rangle}$ is the *reference thermal relaxation timescale*, $C_0 \equiv \langle\!\langle C \rangle\!\rangle$ is the heat capacity of the full atmospheric column in $\mathrm{J\,m^{-2}\,K^{-1}}$, and the approximation on the first line invokes the isothermal assumption (see Equation A.1). Figures 3.1–3.3 use τ_0 and s_τ to characterize the climate sensitivity of each model configuration.

Likewise, I call the temperature response ΔT implied by the relaxation sensitivity parameter s_τ due to the forcing perturbation H the *relaxation climate sensitivity* ΔT_τ, defined as follows:

$$\Delta T_\tau = -\frac{\overline{\langle\langle H \rangle\rangle}}{\overline{\langle\langle \lambda_\tau \rangle\rangle}} = \overline{\langle\langle H \rangle\rangle} \frac{\tau_0}{C_0} \tag{A.7}$$

The relaxation climate sensitivity represents the climate sensitivity of a dynamical core model under the assumption of an isothermal warming response (or spatially uniform feedback parameters; see Equation A.1). Figure 3.4 compares the relaxation climate sensitivity ΔT_τ against empirical measures of the climate sensitivity ΔT obtained from the dynamical core model simulations.

We can estimate the most physically realistic relaxation sensitivity parameter $\hat{s}_\tau$ for a given dynamical core model configuration using the physics of the Planck feedback parameter λ_P. Under the HS94 configuration (see Appendix A.4), the average temperature over the entire atmosphere is around $\overline{\langle T \rangle} \approx 250\,\mathrm{K}$ – similar to the global average Earth emission temperature of $\overline{T}_\mathrm{e} \approx 255\,\mathrm{K}$. If we use $\overline{\langle T \rangle}$ as a stand-in for the emission temperature $\overline{T}_\mathrm{e}$, then our realistic relaxation sensitivity parameter is derived from the Stefan-Boltzmann Law as follows (e.g., *Hartmann* 2015):

$$\hat{s}_\tau = -\frac{1}{\lambda_\mathrm{P}} = \left(\frac{\partial \left(\sigma \overline{T}_\mathrm{e}^{\,4} \right)}{\partial \overline{T}_\mathrm{e}} \right)^{-1} = \left(4\sigma \overline{T}_\mathrm{e}^{\,3} \right)^{-1} \approx 0.28\,\mathrm{K\,/\,W\,m^{-2}} \tag{A.8}$$

where σ is the Stefan-Boltzmann constant. Figure 2.1 compares the relaxation sensitivity parameter s_τ from an HS94 simulation of the dynamical core model against the realistic relaxation sensitivity parameter $\hat{s}_\tau$ and a radiative kernel-derived coupled climate model estimate of the reference sensitivity parameter s_0 (*Soden et al.* 2008, *Zelinka et al.* 2020).

A.4 Model description

For the idealized model experiments described in Chapter 3, I used the spectral dynamical core model from the Geophysical Fluid Dynamics Laboratory (GFDL). I ran the model with a spherical harmonic truncation level of 85 and with 60 vertical hybrid levels spaced according to the European

Center for Medium-Range Weather Forecasts (ECMWF) "L60" specification (used by ECMWF to generate the ERA-Interim reanalysis product; *Dee et al.* 2011).

For each simulation, I used a simple variant of the standard HS94 model configuration. Under HS94, the thermal relaxation rate $Q = -C(T - T^{\mathrm{e}})/\tau$ is evaluated using the following analytic expressions for the equilibrium temperature T^{e} and the thermal relaxation timescale τ (shown in Figure 2.4, A–B):

$$T^{\mathrm{e}} = \max\left\{T^{\mathrm{e}}_{\mathrm{min}},\ \left(\overline{T}^{\mathrm{e}}_{\mathrm{s}} + \Delta^{\mathrm{e}}_{\mathrm{h}}\left(\frac{1}{3} - \sin^2\phi\right) - \Delta^{\mathrm{e}}_{\mathrm{v}}\cos^2\phi\log\left(\frac{p}{p_0}\right)\right)\left(\frac{p}{p_0}\right)^{\kappa}\right\} \tag{A.9}$$

$$\frac{1}{\tau} = \frac{1}{\tau_{\mathrm{max}}} + \left(\frac{1}{\tau_{\mathrm{min}}} - \frac{1}{\tau_{\mathrm{max}}}\right)\max\left\{0,\ \frac{\sigma - \sigma_{\mathrm{b}}}{1 - \sigma_{\mathrm{b}}}\right\}\cos^4(\phi) \tag{A.10}$$

Above, ϕ is latitude, p is pressure, and $\sigma \equiv p/p_{\mathrm{s}}$ is the sigma height coordinate, where p_{s} is the instantaneous surface pressure; $\sigma_b = 0.7$ is the sigma coordinate representing the top of the boundary layer; $\tau_{\mathrm{max}} = 40$ days is the maximum thermal relaxation timescale, realized everywhere above σ_{b}; $\tau_{\mathrm{min}} = 4$ days is the minimum thermal relaxation timescale, realized at the surface on the equator; $T^{\mathrm{e}}_{\mathrm{min}} = 200\,\mathrm{K}$ is the isothermal stratospheric equilibrium temperature; $\overline{T}^{\mathrm{e}}_{\mathrm{s}} = 300\,\mathrm{K}$ is the global average surface equilibrium temperature; $\Delta^{\mathrm{e}}_{\mathrm{h}} = 60\,\mathrm{K}$ is the equator-pole equilibrium temperature difference at the surface; $\Delta^{\mathrm{e}}_{\mathrm{v}} = 10\,\mathrm{K}$ controls the magnitude of the equilibrium static stability in the tropics; $p_0 \equiv 10^5\,\mathrm{Pa}$ is the reference pressure; and $\kappa \equiv R_{\mathrm{d}}/c_p$ is the Poisson constant, where R_{d} is the dry air gas constant and c_p is the specific heat at constant pressure.

I ran each simulation for either 5500 days or 7500 days, with the first 500 days discarded to account for model spin-up. I compiled climatological averages from the remaining days. Since every forcing configuration was hemispherically symmetric, I used northern-southern hemisphere averages of the climatological averages to increase the effective sample size. For most of the simulations, I initialized the model with "cold starts" by imposing randomized small-amplitude vorticity perturbations on an isothermal initial state. However, the spin-up time for cold starts was often longer than 500 days for simulations with long thermal relaxation timescales and small meridional equilibrium temperature gradients. Therefore, I used "warm starts" for configurations

with $\tau_{\max} > 40$ days or $\Delta_{\mathrm{h}}^{\mathrm{e}} < 60\,\mathrm{K}$ (their HS94 values). A "warm start" consisted of initializing the model with the final state of the preceding simulation in the same experiment. For example, I began the $\tau_{\max} = 100$ day simulation with the final timestep from the $\tau_{\max} = 40$ day simulation, the $\tau_{\max} = 200$ day simulation with the final timestep from the $\tau_{\max} = 100$ day simulation, etc. This considerably reduced the spin-up period as diagnosed from time series of extratropical circulation metrics (not shown). The resulting steady-state climates were also no different from climates obtained with cold start initializations – the same steady-state solutions were just obtained more quickly. The simulations that required warm starts were also subject to long timescales of extratropical circulation variability. Therefore, to better resolve the steady-state responses to forcing perturbations, I ran the unperturbed and perturbed simulations with $\tau_{\max} > 40$ days for an extra 2000 days (7500 days instead of 5500 days).

Appendix B

Coupled models

B.1 Forcing-feedback metrics

For the results shown in Chapters 4 and 5, I used 59 models from CMIP6 and 30 models from CMIP5 (see Tables B.1 and B.2 for the full lists). To characterize the forcing-feedback behavior of each model, I used the first ensemble member from its pre-industrial experiment and the first ensemble member from its abrupt $4\times CO_2$ experiment (these were typically r1i1p1f1 for CMIP6 and r1i1p1 for CMIP5; see Tables B.1 and B.2). The pre-industrial experiments used constant radiative forcing agents representative of the period prior to the industrial revolution (*Eyring et al.* 2016, *Taylor et al.* 2012); I call the feedbacks estimated from these experiments *unperturbed climate feedbacks*. The abrupt $4\times CO_2$ experiments were initialized from year zero of the pre-industrial experiments with a constant, uniformly quadrupled CO_2 perturbation; I call the feedbacks estimated from these experiments *perturbed climate feedbacks*. To separately characterize the fast and slow components of the quadrupled CO_2 response, I further divided the corresponding 150-year experiment results into separate *early* (years 0–20) and *late* (years 20–150) periods (following *Andrews et al.* 2015, *Geoffroy et al.* 2013a, *Held et al.* 2010). I calculated each climate term and each feedback term using monthly-averages from the relevant experiment mapped onto a standard $5^\circ\times5^\circ$ longitude-latitude grid using an area-conservative weighting scheme (*Hanke et al.* 2016).

I estimated unperturbed, early perturbed, and late perturbed climate feedbacks from each time series using the *Gregory regression* method (*Gregory et al.* 2004). This consisted of linearly regressing annual anomalies in top-of-atmosphere radiative flux R against anomalies in surface temperature T, with anomalies always taken relative to the monthly 150-year pre-industrial climatology. The resulting least-squares regression coefficients represent estimates of the *global climate feedback parameter* and can be written $\lambda \equiv \sum_t R'T' / \sum_t T'^2$, where t indicates time and primes indicate deviations from the average anomaly (*Gregory et al.* 2004). The x- and y-intercepts of

Table B.1: The CMIP6 models used in this thesis. *Institute* indicates the standard or abbreviated `institute_id` for each modeling center. *Loc.* indicates the ISO-3166-1 country or location code of the center (e.g., AU for Australia, CN for China, FR for France). *Num.* indicates the number of models used from the center. *Model(s)* lists the individual models selected from each center. *Member(s)* lists the "flagship" ensemble members selected from each pre-industrial and abrupt $4\times CO_2$ experiment (generally matching the ensemble members used in *Zelinka et al.* 2020). Note that parentheses indicate two distinct ensemble member identifiers selected from the pre-industrial ensemble and its branching abrupt $4\times CO_2$ ensemble(s). Where there are no parentheses, the same identifier was selected from both ensembles. I used the `parent_variant_label` metadata to ensure that the selected abrupt $4\times CO_2$ ensemble members were always branched directly from the selected pre-industrial ensemble members.

Institute	Loc.	Num.	Model(s)	Member(s)
AS	TW	1	TaiESM1	r1i1p1f1
AWI	DE	1	AWI-CM-1-1-MR	r1i1p1f1
BCC	CN	2	BCC-ESM1	r1i1pf11
			BCC-CSM2-MR	r1i1p1f1
CAMS	CN	1	CAMS-CSM1-0	r1i1p1f1
CAS	CN	3	CAS-ESM2-0	r1i1p1f1
			FGOALS-g3	r1i1p1f1
			FGOALS-f3-L	r1i1p1f1
CCCma	CA	2	CanESM5-1	r1i1p1f1
			CanESM5	r1i1p1f1
CMCC	IT	2	CMCC-ESM2	r1i1p1f1
			CMCC-CM2-SR5	r1i1p1f1
CNRM	FR	3	CNRM-ESM2-1	r1i1p1f2
			CNRM-CM6-1-HR	r1i1p1f2
			CNRM-CM6-1	r1i1p1f2
CSIRO	AU	2	ACCESS-ESM1-5	r1i1p1f1
			ACCESS-CM2	r1i1p1f1
E3SM	US	2	E3SM-2-0	r1i1p1f1
			E3SM-1-0	r1i1p1f1
EC-Earth	EU	5	EC-Earth3	r(1,8)i1p1f1
			EC-Earth3-AerChem	r1i1p1f1
			EC-Earth3-CC	r1i1p1f1
			EC-Earth3-Veg-LR	r1i1p1f1
			EC-Earth3-Veg	r1i1p1f1
GFDL	US	2	GFDL-ESM4	r1i1p1f1
			GFDL-CM4	r1i1p1f1
GISS	US	4	GISS-E2-2-H	r1i1p1f1
			GISS-E2-2-G	r1i1p1f1
			GISS-E2-1-H	r1i1p1f1
			GISS-E2-1-G	r1i1p1f1
IITM	IN	1	IITM-ESM	r1i1p1f1
INM	RU	2	INM-CM5-0	r1i1p1f1
			INM-CM4-8	r1i1p1f1
IPSL	FR	2	IPSL-CM5A2-INCA	r1i1p1f1
			IPSL-CM6A-LR	r1i1p1f1
KIOST	KR	1	KIOST-ESM	r1i1p1f1
KMA	KR	1	KACE-1-0-G	r1i1p1f1
MIROC	JP	3	MIROC-ES2H	r1i1p4f2
			MIROC-ES2L	r1i1p1f2
			MIROC6	r1i1p1f1
MOHC	UK	4	UKESM1-1-LL	r1i1p1f2
			UKESM1-0-LL	r1i1p1f2
			HadGEM3-GC31-MM	r1i1p1f(1,3)
			HadGEM3-GC31-LL	r1i1p1f(1,3)
MPI	DE	4	MPI-ESM1-2-HR	r1i1p1f1
			MPI-ESM1-2-LR	r1i1p1f1
			MPI-ESM-1-2-HAM	r1i1p1f1
			ICON-ESM-LR	r1i1p1f1
MRI	JP	1	MRI-ESM2-0	r1i1p1f1
NCAR	US	4	CESM2-WACCM	r1i1p1f1
			CESM2-WACCM-FV2	r1i1p1f1
			CESM2	r1i1p1f1
			CESM2-FV2	r1i1p1f1
NCC	NO	3	NorESM2-MM	r1i1p1f1
			NorESM2-LM	r1i1p1f1
			NorCPM1	r1i1p1f1
NUIST	CN	1	NESM3	r1i1p1f1
SNU	KR	1	SAM0-UNICON	r1i1p1f1
THU	CN	1	CIESM	r1i1p1f1

Table B.2: The CMIP5 models used in this thesis. See Table B.1 for details.

Institute	Loc.	Num.	Model(s)	Member(s)
BCC	CN	2	bcc-csm1-1-m	r1i1p1
			bcc-csm1-1	r1i1p1
BNU	CN	1	BNU-ESM	r1i1p1
CAS	CN	2	FGOALS-g2	r1i1p1
			FGOALS-s2	r1i1p1
CCCma	CA	1	CanESM2	r1i1p1
CNRM	FR	1	CNRM-CM5-2	r1i1p1
			CNRM-CM5	r1i1p1
CSIRO	AU	3	ACCESS1-3	r1i1p1
			ACCESS1-0	r1i1p1
			CSIRO-Mk3-6-0	r1i1p1
GFDL	US	3	GFDL-ESM2M	r1i1p1
			GFDL-ESM2G	r1i1p1
			GFDL-CM3	r1i1p1
GISS	US	2	GISS-E2-H	r1i1p1
			GISS-E2-R	r1i1p1
INM	RU	1	inmcm4	r1i1p1
IPSL	FR	3	IPSL-CM5A-MR	r1i1p1
			IPSL-CM5A-LR	r1i1p1
			IPSL-CM5B-LR	r1i1p1
MIROC	JP	2	MIROC-ESM	r1i1p1
			MIROC5	r1i1p1
MOHC	UK	1	HadGEM2-ES	r1i1p1
MPI	DE	3	MPI-ESM-MR	r1i1p1
			MPI-ESM-LR	r1i1p1
			MPI-ESM-P	r1i1p1
MRI	JP	1	MRI-CGCM3	r1i1p1
NCAR	US	1	CCSM4	r1i1p1
NCC	NO	2	NorESM1-M	r1i1p1
			NorESM1-ME	r1i1p1

each Gregory regression provide estimates of the climate sensitivity and radiative forcing perturbation. The quadrupled-CO_2 regression results for each model and institute-average are shown in Figures B.1 and B.2. The results are very similar to another recent multi-model analysis (*Zelinka et al.* (2020); Figure B.3).

I used the *radiative kernel* technique to break down each climate feedback parameter into separate process-level components (*Held and Shell* 2012, *Shell et al.* 2008, *Soden and Held* 2006, *Soden et al.* 2008). I started by interpolating a set of reanalysis-based surface temperature, air temperature, specific humidity, and surface albedo kernels (*Huang et al.* 2017) onto the $5^\circ \times 5^\circ$ grid and pressure levels I used for the CMIP data. Then, for each experiment, I estimated the time-evolving radiative response to anomalous surface and atmosphere conditions from the products of the kernels with their corresponding, time-evolving state variables (note that the specific humidity kernels were scaled logarithmically; *Soden and Held* 2006, *Soden et al.* 2008). For the air temperature and specific humidity responses, I weighted the kernel products by pressure level thickness and vertically integrated to a monthly-varying tropopause (defined as the pressure level of the $-2\ \mathrm{K}\,/\,\mathrm{km}$ lapse rate estimated from linear interpolation across pseudoheights; *Reichler et al.* 2003). Finally, I used Gregory regressions with combinations of the annual-average model-simulated fluxes and kernel-derived fluxes to estimate the feedback components (*Soden and Held* 2006, *Soden et al.* 2008). For the cloud feedbacks, I used the model-simulated shortwave and longwave cloud radiative effects adjusted by the time-evolving shortwave and longwave cloud masking implied by the kernels (*Soden et al.* 2008). For the non-cloud feedbacks, I used the residual of the net feedback and the cloud feedback.

Figure B.3 compares the quadrupled-CO_2 Gregory regression computed for this thesis (y-axis) to the results from *Zelinka et al.*, 2020 (x-axis). As we used the same general methodology (*Zelinka et al.* 2020) and the same radiative kernels (*Huang et al.* 2017), the results from this thesis are in very close agreement with *Zelinka et al.* (2020). There are only minor differences in the Planck feedback, associated with its very narrow range of inter-model spread (Figure B.3, I); the relative humidity feedback, possibly arising from minor differences in our vertical integration schemes

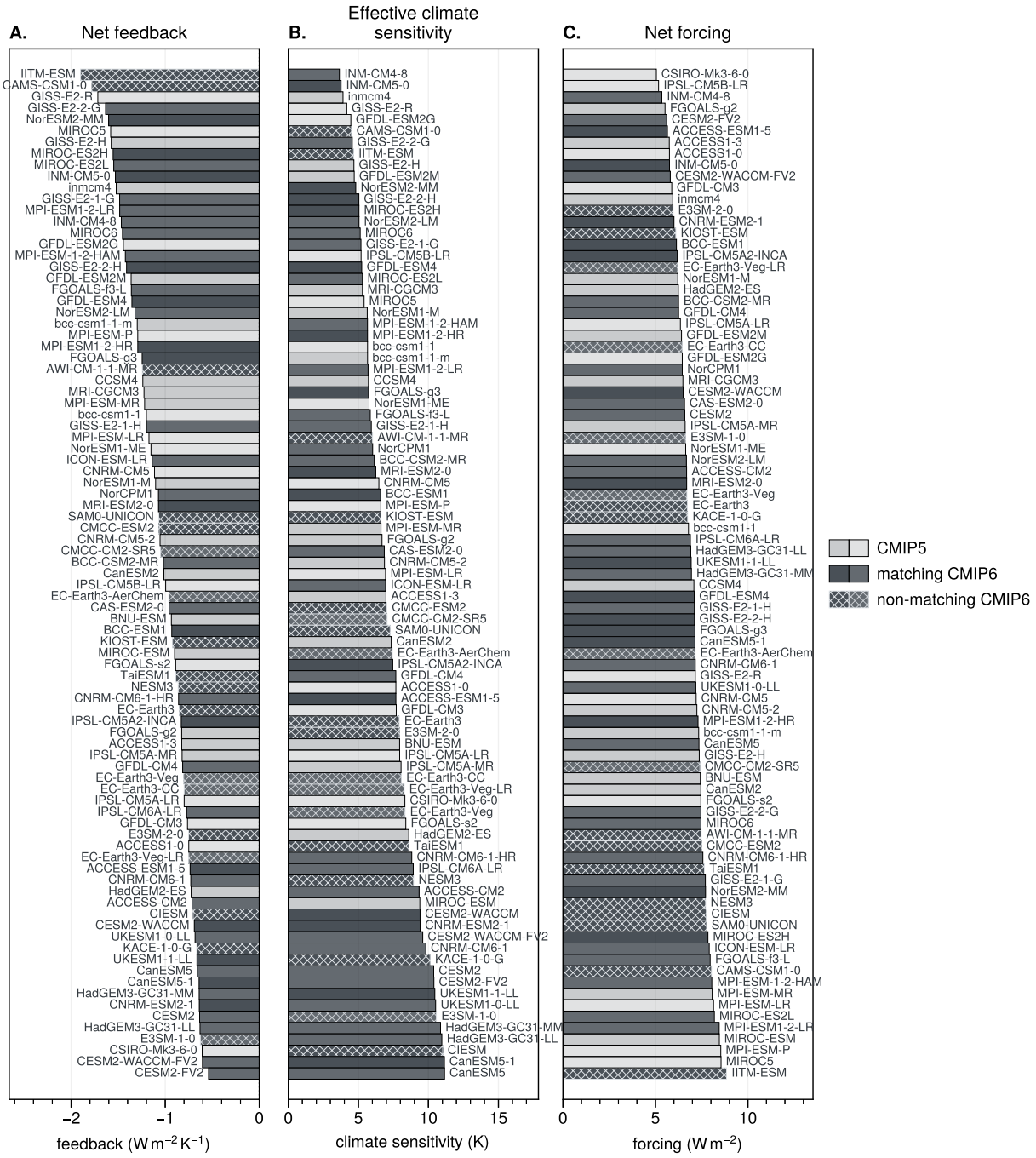

Figure B.1: Forcing-feedback analysis results for CMIP5 and CMIP6 abrupt $4\times CO_2$ experiments (see also Figure B.4). Light shading (dark shading) indicates models from CMIP5 (CMIP6). Hatching is used for CMIP6 models published by institutes that did not publish models in CMIP5. For each institute, a slightly darker shade is used for the first model listed in Tables B.1 and B.2, and a slightly lighter shade is used for any remaining models.

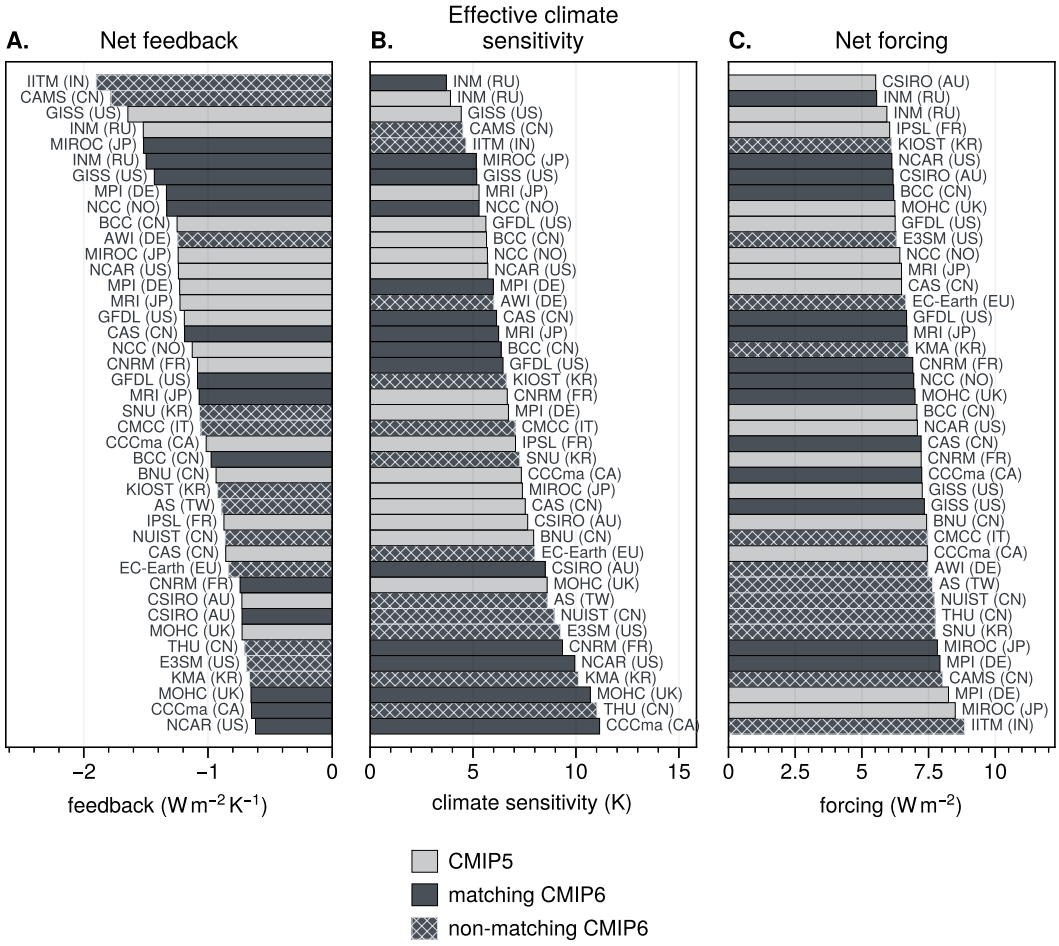

Figure B.2: As in Figure B.1 but showing institute-averages instead of individual models (see also Figure B.6). Annotations indicate the institute names and country codes from Tables B.1 and B.2.

(Figure B.3, K); and the albedo feedback, possibly arising from the initial remapping to a $5° \times 5°$ grid (Figure B.3, F).

B.2 Institute averaging

Owing to shared model components, the climate states simulated by models across CMIP ensembles are not expected or designed to be wholly independent (*Abramowitz and Bishop* 2015, *Abramowitz et al.* 2018, *Knutti* 2010, *Knutti et al.* 2010, *Masson and Knutti* 2011, *Tebaldi and Knutti* 2007). Throughout Chapters 4 and 5, to help reduce biases on inter-model statistics arising from inter-model dependencies, I employed an *institutional democracy* scheme. Compared to the traditional model democracy scheme, in which each model result is treated as an independent sample, institutional democracy treats each group of models from the same modeling institute and CMIP generation as an independent sample by averaging their output together before computing ensemble statistics (*Abramowitz et al.* 2018, *Leduc et al.* 2016). This helps reduce double counting biases, where the degrees of freedom on inter-model statistics are underestimated due to giving single results from models with more published variants higher weight. While institutional democracy does not perfectly account for model similarities within the CMIP ensembles (*Abramowitz et al.* 2018, *Kuma* 2023), it provides a minimal and reasonable first-order correction to the effect of model double counting on inter-model statistics (*Abramowitz et al.* 2018, *Leduc et al.* 2016, *Masson and Knutti* 2011, *Pennell and Reichler* 2011).

The underlying assumption of institutional democracy is that model results from the same institute are closer together than model results from different institutes. To test this assumption, I use a bootstrapping approach. On average, within institute groups of more than one model, the quadrupled-CO_2 effective climate sensitivity spans 1.18 K with a standard deviation of 0.55 K. Only a handful of institute groups have quadrupled-CO_2 responses that span more than 2 K (GFDL, IPSL, and MIROC in CMIP5; GFDL and E3SM in CMIP6). By comparison, for $100\,000$ random arrangements of the same models into the same distribution of group sizes, the average group spans 3.03 K and has a standard deviation of 1.34 K. Notably, the average spread of the random groups is

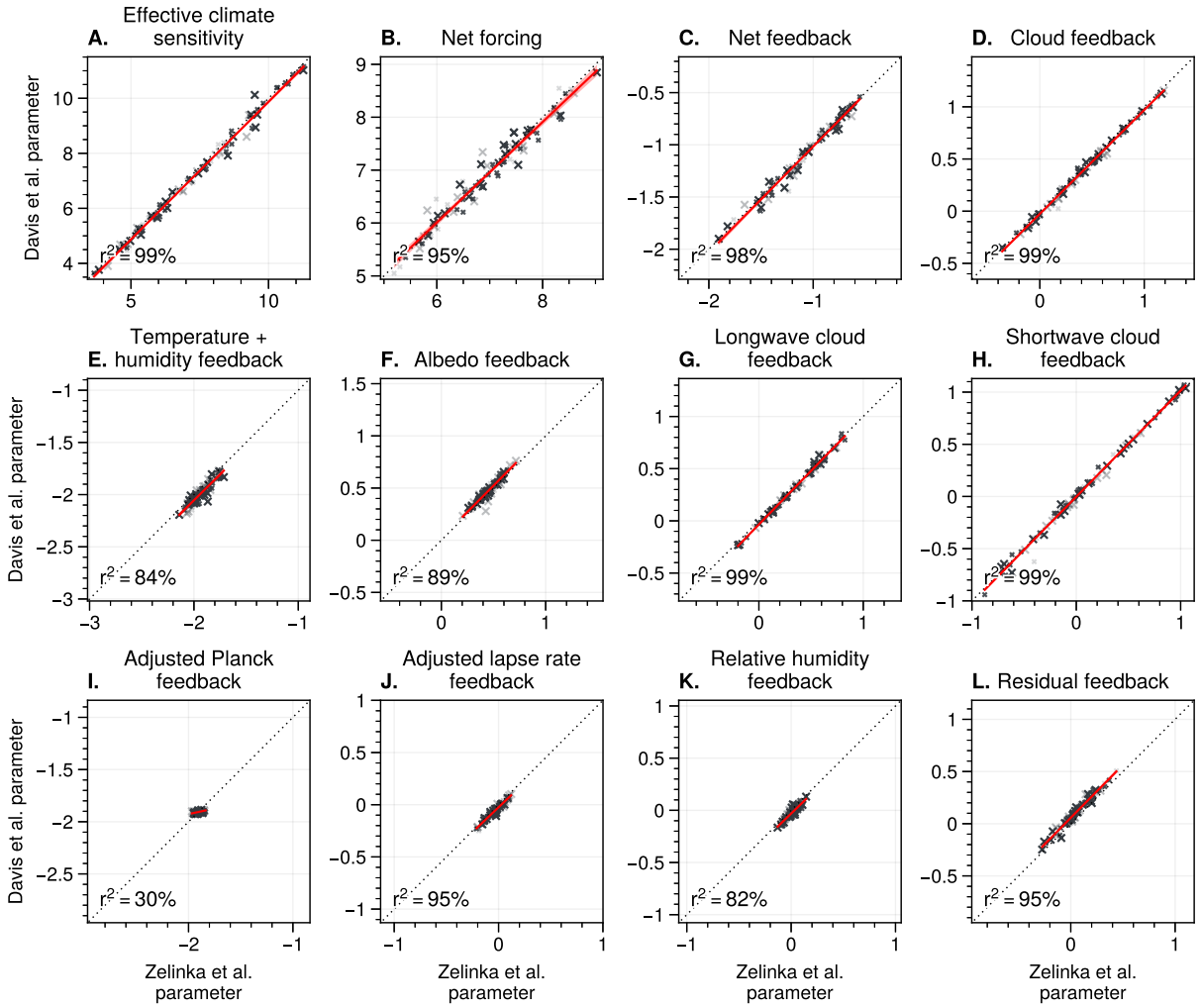

Figure B.3: Comparison of abrupt $4\times CO_2$ forcing-feedback analysis from this thesis to analysis from *Zelinka et al.* (2020). For each panel, the model estimates from *Zelinka et al.* (2020) are indicated on the x axis and the estimates from this thesis are indicated on the y axis. The black dashed lines indicate the 1:1 relationship. The red lines indicate the linear least-squares regressions, with shading indicating 95% uncertainty bounds according to a Student's t-distribution (assuming the regression residuals are normally distributed). The bottom-right annotations indicate the variance explained by the fits. The units are K for the effective climate sensitivity (A), $\mathrm{W\,m^{-2}}$ for the effective forcing (B), and $\mathrm{W\,m^{-2}\,K^{-1}}$ for all feedback terms (C–L). Note that the x and y axes of the feedback panels (C–L) are scaled to have identical width in $\mathrm{W\,m^{-2}\,K^{-1}}$.

larger than virtually all of the CMIP6 institute groups and all but two of the CMIP5 institute groups (GFDL and MIROC). Further, the standard deviation across CMIP5 and CMIP6 institute-averages (1.89 K) is only slightly lower than the standard deviation across individual models (1.99 K), suggesting that institute-averaging does not reduce the overall ensemble spread. I found very similar results for the climate feedback parameters (not shown). Figure B.1 is qualitatively consistent with this analysis; model results from the same institute and CMIP generation are generally found near one another, and the ensemble spreads are similar to Figure B.2. These results highlight the comparative similarity of models belonging to the same institute and the suitability of institute-averaging for reducing double counting biases.

To quantify the effect of institute-averaging on the ensemble statistics shown in this thesis, Figures B.4 and B.5 reproduce Figures 4.2 and 4.3 using models as independent samples instead of institutes. Compared to Figure 4.2, the spread differences in Figure B.4 between CMIP generations, perturbation response times, and feedback components are largely similar – although the effects of a few outlier models are more noticeable. Likewise, the regression coefficient magnitudes and percents variance explained in Figure B.5 are largely similar to Figure 4.3. However, the 50% and 95% confidence intervals on the regression coefficients are substantially reduced when models are used as independent samples (Figure B.5). The reduction is especially large for the CMIP6 ensemble, for which institutes publish as many as five variants of the same model (Table B.1). This suggests that the primary effect of treating models instead of institutes as independent samples is to produce misleadingly-narrow confidence intervals on inter-model statistics. It also demonstrates that the results presented in this thesis are robust to the methodological choice of institute-averaging.

B.3 Institute grouping

The CMIP6 ensemble includes models published by several new institutes that did not participate in CMIP5. Some of these models are closely related to other CMIP6 models developed by CMIP5-era institutes (raising further double counting concerns), while others include more robust

changes or were even created from scratch (*Kuma* 2023). To further address shared model components, and to test whether differences between CMIP5 and CMIP6 are driven by the introduction of new institutes or updates from existing institutes, I split the CMIP6 ensemble into two groups. The first group, called *matching CMIP6*, consists of institutes that published pre-industrial and abrupt $4\times CO_2$ experiments in CMIP5 with the output required for feedback analysis. The second group, called *non-matching CMIP6*, consists of institutes that did not publish the requisite experiments or output in CMIP5. The resulting three ensembles have a similar number of institutes – CMIP5 has 16 institutes and 30 models; matching CMIP6 has 15 institutes and 41 models; and non-matching CMIP6 has 12 institutes and 18 models (see Tables B.1 and B.2).

Figures B.6 and B.7 reproduce Figures 4.2 and 4.3 using institute-averages across the CMIP5 ensemble and the separate matching and non-matching CMIP6 ensembles. In general, the notable differences between CMIP5 and CMIP6 are also evident for each separate CMIP6 group. While there are some differences between the CMIP6 groups, they tend to be smaller than the differences between the full CMIP5 and CMIP6 ensembles. Compared to CMIP5, the CMIP6 groups are characterized by 1) slightly more positive perturbed feedbacks with greater inter-model spread, and 2) slightly more negative unperturbed feedbacks with equal inter-model spread, with most of these changes driven by the cloud component (Figures 4.2 and B.6). Likewise, the perturbed feedbacks of each CMIP6 group are more predictable from the unperturbed feedbacks, again due to the cloud component (Figures 4.3 and B.7). There are a few notable differences between the CMIP6 groups, with non-matching CMIP6 models exhibiting somewhat more positive and more predictable perturbed cloud feedbacks (Figures B.6 and B.7). However, the broad consistency of the CMIP6 results described in this thesis with both the matching and non-matching CMIP6 groups suggests that differences in inter-model statistics between CMIP5 and CMIP6 are not an artifact of model similarities or structural changes to the CMIP ensemble. Instead, they appear to be driven by updates to the underlying numerics and parameterizations of CMIP5-era models.

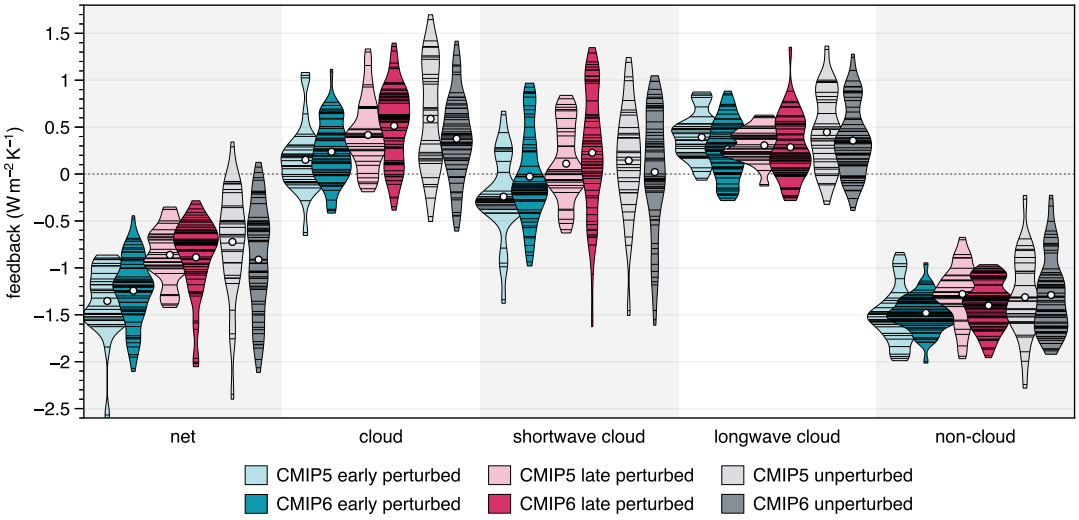

Figure B.4: As in Figure 4.2 but using individual models instead of institute averages.

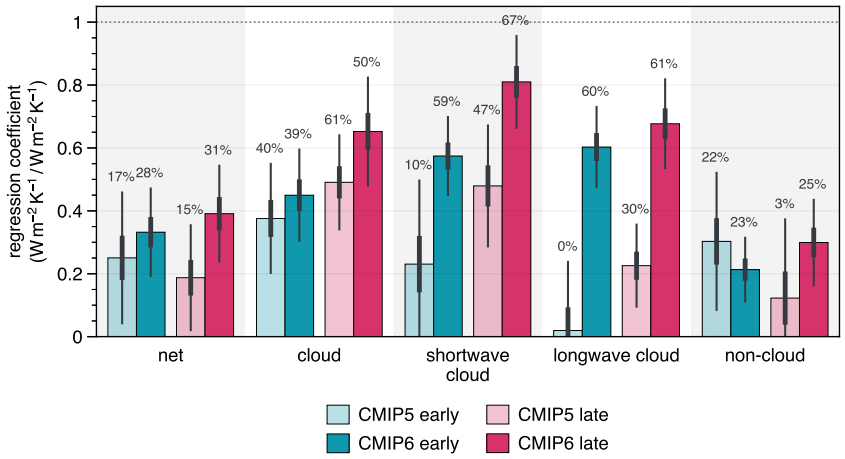

Figure B.5: As in Figure 4.3 but using individual models instead of institute averages.

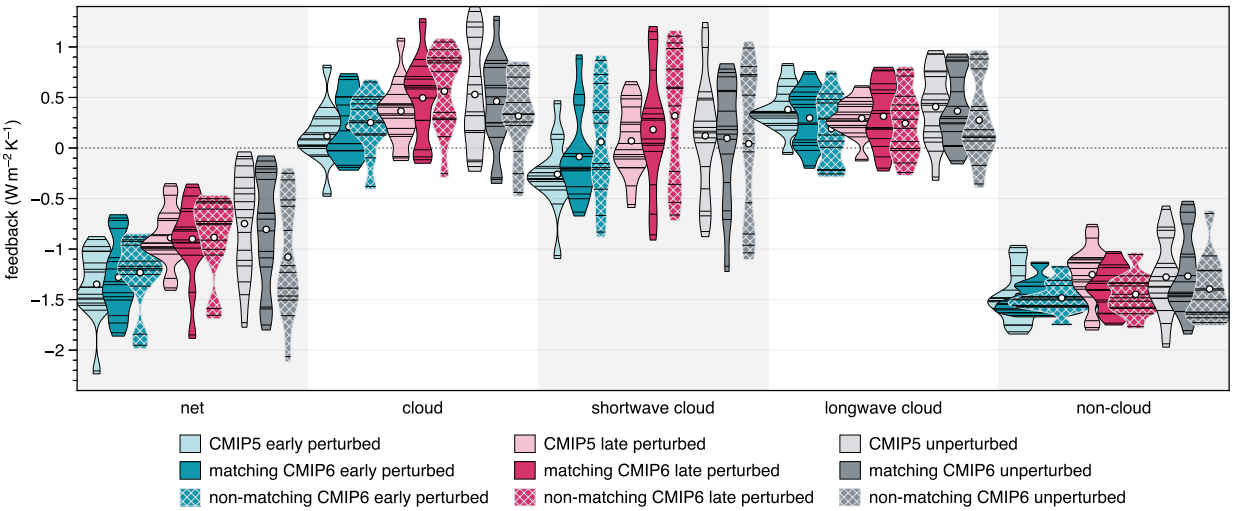

Figure B.6: As in Figure 4.2 but using two separate groups of CMIP6 institutes.

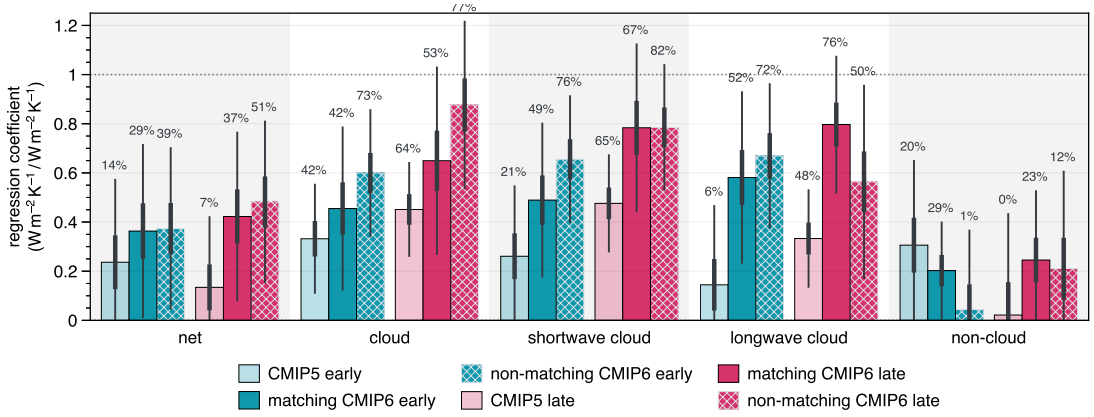

Figure B.7: As in Figure 4.3 but using two separate groups of CMIP6 institutes.

Appendix C

Software and data availability

The dynamical core model used in this thesis is available in its original form online via the Geophysical Fluid Dynamics Laboratory (https://www.gfdl.noaa.gov/fms/). A version of the model with modifications for the experiments described in this thesis, along with the code I used to conduct the experiments, is published on Github (https://github.com/lukelbd/gfdl-fms, https://github.com/lukelbd/drycore).

The CMIP6 and CMIP5 data used in this thesis were obtained online via the Earth System Grid Federation (ESGF; https://esgf.llnl.gov) using the public ESGF python API (https://github.com/ESGF/esgf-pyclient). The code I used to systematically download up-to-date model data and perform climatology and forcing-feedback calculations is published on Github (https://github.com/lukelbd/cmip-data).

The *Huang et al.* (2017) radiative kernels shown in Figure 2.2 and used for feedback estimates throughout Chapter 4 were obtained online via Mendeley Data (https://doi.org/10.17632/3drx8fmmz9.1). The *Zelinka et al.* (2020) climate sensitivity, climate feedback, and radiative forcing estimates shown in Figures 2.1 and B.3 were obtained online via Zenodo (https://doi.org/10.5281/zenodo.5206851).

This thesis also benefited from several open-source software packages: NetCDF Operators (NCO) and Climate Data Operators (CDO), used to process the dynamical core and coupled model data (https://nco.sourceforge.net, https://code.mpimet.mpg.de/projects/cdo/); the python packages numpy, pandas, xarray, and pint, used to derive physical quantities and inter-model statistics (https://numpy.org, https://pandas.pydata.org, https://xarray.pydata.org, https://pint.readthedocs.io); and the python packages matplotlib, cartopy, and proplot, used to produce figures for this thesis (https://matplotlib.org, https://scitools.org.uk/cartopy, https://proplot.readthedocs.io).